UNIVERSITY OF CALIFORNIA SAN DIEGO

Aspects of Dark Matter Dynamics in Stellar and Cosmological Environments

A dissertation submitted in partial satisfaction of the
requirements for the degree
Doctor of Philosophy

in

Physics

by

Jung-Tsung Li

Committee in charge:

Professor George M. Fuller, Chair
Professor Dusan Keres
Professor Julius Kuti
Professor David A. Meyer
Professor Mark H. Thiemens

2021

The Dissertation of Jung-Tsung Li is approved, and it is acceptable in quality and form for publication on microfilm and electronically.

University of California San Diego

2021

DEDICATION

To my family

EPIGRAPH

Space, the whole universe - I know no better place to find new physics.

Eugene N. Parker

TABLE OF CONTENTS

LIST OF FIGURES

LIST OF TABLES

ACKNOWLEDGEMENTS

First and foremost, I would like to express my sincere appreciation to my thesis supervisor George Fuller for his enthusiastic mentorship, guidance, and support. George leads me to the fields of dark matter, neutrino physics, gravitational waves, and many other interdisciplinary areas throughout my time in graduate school. He has trained me well as a generalist and showed me the fun and excitement of exploring new physics from space and the universe. The insightful and creative thinking that I learn from George is invaluable to my career.

I would also like to thank Tongyan Lin for the collaborations on research, teaching, and all the supports. Tongyan always encourages me to be patient and do the right thing for good scientific work, even if the path ahead is challenging. The rigorous scientific attitude and the vision in physics I learn from her elevate my ability to a higher level. I am grateful for the opportunity to work with Tongyan.

My research would not have been possible without my fantastic collaborators. I want to thank Chad Kishimoto for the stimulating discussion on gravitational-wave memory and Evan Grohs for guiding me to the field of precision cosmology.

My time in the astronomy and plasma groups at UCSD shape who I am now and influence my career path a lot. For that, I would like to especially thank Patrick Diamond for the fantastic and stimulating plasma/MHD courses he offered at UCSD; and Mikhail Malkov for his patient guidance on cosmic ray physics.

Last but not least, I would like to thank my friend Hope How-Huan Chen for his encouragement whenever I hit rock bottom during graduate school.

Chapter 2 is, in part, a reprint of material from published work done in collaboration with George Fuller and Chad Kishimoto, as it appears in the *Physical Review D*, "Neutrino burst-generated gravitational radiation from collapsing supermassive star", *Phys. Rev. D* **98** (2), 023002. The dissertation author was the primary investigator and author of this paper.

Chapter 3 is, in full, a reprint of material from published work done in collaboration with George M. Fuller and Evan Grohs, as it appears in the *Journal of Cosmology and Astroparticle*

Physics, "Probing dark photons in the early universe with big bang nucleosynthesi", *JCAP* **12** (2020), 049. The dissertation author was the primary investigator and author of this paper.

Chapter 4 is, in full, a reprint of material from published work done in collaboration with Tongyan Lin, as it appears in the *Physical Review D*, "Dynamics of millicharged dark matter in supernova remnants", *Phys. Rev. D* **101** (10), 103034. The dissertation author was the primary investigator and author of this paper.

VITA

2007-2011 Bachelor of Science, National Tsing Hua University, Hsinchu

2011-2013 Master of Science, National Tsing Hua University, Hsinchu

2014-2021 Doctor of Philosophy, University of California, San Diego

ABSTRACT OF THE DISSERTATION

Aspects of Dark Matter Dynamics in Stellar and Cosmological Environments

by

Jung-Tsung Li

Doctor of Philosophy in Physics

University of California San Diego, 2021

Professor George M. Fuller, Chair

This dissertation studies the aspects of dark matter and gravitational waves in dense and compact environments. We consider gravitational waves from supermassive black hole formation, dark photon production and decay in big bang nucleosynthesis, and millicharged dark matter acceleration in supernova shock. We begin with a general overview of the three topics studied in this dissertation.

In Chapter 2, we investigate the formation of supermassive black holes (SMBHs) from the collapse of high-redshift supermassive stars and study the neutrino burst-generated gravitational waves (GW). We investigated the GW signatures driven by the neutrino bursts, which create unique memory GW signals. Our result may provide an intriguing hint toward solving the

problem of the formation of SMBHs in the high redshift universe.

In Chapter 3, we calculate the freeze-in abundance of dark photons and use the code BURST to trace the evolution of nucleosynthesis numerically from the beginning of weak decoupling with the presence of late-decay dark photons. Using the 1%-level precision in the primordial deuterium abundance measurements from quasar absorption lines, our result not only excludes a range of dark photon model parameters but also identify ranges of dark photon mass and couplings accessible in future Stage-4 cosmic microwave background experiments.

In Chapter 4, we provide a mechanism for millicharged dark matter (mDM) to scatter efficiently with Standard Model particles in supernova remnants. Our work reveals that the supernova shocks could sweep up and thermalize the ambient mDM via plasma instability. We also address the difficulty of getting Fermi-accelerated mDM owing to an ultra-slow instability upstream of the shock. Our result implies that the sensitivity for detection of terrestrial experiments for charged DM is, in fact, not strongly affected by supernova shocks, despite prior claims.

Chapter 1

General introduction

My graduate research centers around two unsolved problems in astrophysics: *how are the high redshift supermassive black holes formed* and *what is dark matter made of*. Both problems have remained open for many decades, and yet no definitive theories have been reached. Fortunately, the recent tremendous progress on the high-precision observations has provided us increasingly stringent cosmological and astrophysical data for improving our understanding of the models and testing the new physics.

This thesis investigates the two problems from the perspective of interdisciplinary areas between particle phenomenology, neutrinos, and plasma physics. We focus on three specific topics: (1) neutrino burst-generated gravitational wave signals from high-redshift supermassive stars, (2) dark photon phenomenology in big bang nucleosynthesis, and (3) dynamics of millicharged particles in supernova shocks. For the clarity of the presentation, we will split this thesis into three groups.

1.1 From supermassive star to supermassive black hole

Supermassive black hole (SMBH) refers to a huge black hole with a mass above $10^5\,M_\odot$. Strong gravitation from these holes powers active galactic nuclei and quasar by accreting interstellar gas. Almost every massive galaxy contains more than one SMBH at its galactic center. The SMBH in our Milky Way resides at the region called Sagittarius A* with a mass

of $4.1 \times 10^6 M_\odot$ [1]. The most massive BH ever discovered is TON 618 quasar with a mass of $6.6 \times 10^{10} M_\odot$ [2].

Supermassive black holes aren't just exclusive to late times. In the past few years, an increasing number of luminous quasars powered by SMBH of mass of $\sim 10^9 M_\odot$ have been discovered at the redshift $z > 6$ [3–7]. The oldest known quasar is at $z = 7.642$, corresponding to the age of the universe of approximately 690 Myr, with a black hole mass of about $1.6 \times 10^9 M_\odot$ [8]. It's surprising that BH can grow to such massive mass so rapidly: To get an SMBH with a mass of $10^9 M_\odot$ by $z \sim 7$, a "seed" black hole would have to start with a mass of, at least, $\sim 10^3 M_\odot$ at the time the first luminous objects were formed ($z \sim 30$) and grow at the Eddington limit throughout [9].

The discovery of these high redshift quasars invites the question of how the seed black holes were formed and grown to $\sim 10^9 M_\odot$ in less than 1 Gyr after the Big Bang. The flow chart drawn by Begelman & Rees [10, 11] four decades ago is still an excellent guideline showing the candidate pathways to SMBH formation. Several of them include the matter accumulation from the remnants of metal-free Population III stars [12, 13] and the direct collapse of self-gravitating gas [14, 15], either with or without hydrogen-burning supermassive stars (SMS) as the intermediate stage.

In this dissertation, we focus on the direct collapse scenario with an SMS collapsing to an SMBH. The formation of SMS can be obtained either by suppression of fragmentation of a collapsing primordial gas cloud [14, 16–21], by forming such an object in a dense star cluster via tidal gas stripping in close stellar encounters [22–25], or by the mergers of massive gas-rich galaxies at high redshifts [26]. This type of star is high entropy and fully convective configuration, with stellar mass $M_\star \gtrsim 5 \times 10^4\ M_\odot$. While the bulk of the mass-energy is provided by baryon rest mass, the entropy and pressure support come from radiation fields [27–30], resulting in the adiabatic index being close to $4/3$ and a star that is unstable to Feynman-Chandrasekhar instability [31, 32].

During the collapse of SMS, the innermost 25% of the star plunges homologously to a

BH in about one dynamical timescale, with more than a few percent of the gravitational binding energy becoming neutrino radiation. For an SMS with a stellar mass of $4 \times 10^5 M_\odot$, the total neutrino energy emitted during the collapse is $\sim 4 \times 10^{57}$ ergs in a timescale of $1 - 10$ seconds.

With such a strong neutrino luminosity from a collapsing SMS, it is tempting to consider the prospect of the direct neutrino detection. Considering a SMS of the stellar mass of $M_\star = 4 \times 10^5\ M_\odot$, the average neutrino energy is about 4 MeV [33]. However, since these neutrinos are radiated from the SMS at $z > 6$, their average energy suffering a redshift factor of $(1+z) \approx 7$ would have the average energy of only ≈ 0.6 MeV, which does not pass the energy threshold of Super-Kamiokande experiment (5.5 MeV). Moreover, the neutrinos from the Sun with the average energy of 1 MeV further reduces the prospect of direct neutrino detection of the collapsing SMS.

The prospect of detecting *each individual* neutrino by terrestrial neutrino experiments is dismal. Fortunately, the gravitational wave emitted by a *collective* of neutrinos is a promising signal to explore. This aspect is especially encouraged after the success of LIGO/VIRGO has demonstrated the future potential of laser interferometry for probing unexplored regimes beyond the reach of the traditional telescopes and neutrino detectors. In Chapter 2, we consider the gravitational wave signals from a time-changing effective quadrupole moment generated by the neutrino burst in a collapsing SMS. We also analyze the prospect of detection through the proposed upcoming space-based laser interferometry like DECIGO [34] and BBO [35, 36].

1.2 Dark matter and dark sector physics

The modern cosmology is based primarily on the ΛCDM model. This model has three essential ingredients: the cosmological constant Λ governing the expansion of the universe, the collisionless cold dark matter (CDM) fluid, and the ordinary matter, including baryons, photons, and neutrinos. This model also assumes the General Relativity describes the universe at large scales. Under these conditions, the nearly scale-invariant matter and metric perturbations are amplified by gravitational instability and form the temperature anisotropy of CMB and the

large-scale structures that we see today.

According to the 2018 Planck Satellite observation of the CMB, the current total mass-energy in the universe contains approximately 5% ordinary matter and radiation, 27% dark matter, and 68% dark energy. That is, dark matter constitutes about 84% of the total mass in the universe today. The dark matter need not be composed of the same particle or object. It could be a combination of undiscovered elementary particles, the composite objects, or even primordial black holes. The minimum requirement is dark matter interacts very weakly with radiation and baryonic matter except through gravity. Before exploring the possible dark matter candidates, we would like to know how the early universe gives rise to the observed relic dark matter abundance. In the following paragraphs, we give an overview of the DM production mechanism with the assumption that the relic DM abundance consists of only one *particle* DM candidate.

There are two main production mechanisms for particle DM: the thermal freeze-out of nonrelativistic DM and the freeze-in. In the freeze-out scenario, DM is initially in chemical equilibrium with the Standard Model thermal bath at high temperatures. As the universe expands, the DM-DM annihilation rate eventually becomes lower than the Hubble expansion rate. Subsequently, the DM particles decouple from the thermal bath, and the DM relic abundance is "frozen out". To obtain the observed relic abundance, the minimum value for the thermally-averaged cross-section of DM self-annihilation is $\langle \sigma v \rangle \approx 2.2 \times 10^{-26}$ cm^3/s [37]. Below it, the DM particles are not annihilated efficiently enough to reach the observed relic abundance. Based on this cross-section, the unitarity limit sets the upper bound of the DM mass m_χ at ~ 100 TeV [38]. The lower bound of the DM mass in the freeze-out scenario comes from the warm dark matter limit of the structure formation, which gives $m_\chi \gtrsim 10$ keV.

One advantage of the freeze-out mechanism is that the DM relic abundance is not sensitive to the initial conditions at the reheating after inflation. Another merit is that a DM candidate with TeV-scale mass, together with the SM gauge couplings, naturally gives rise to the desired annihilation cross-section and does not require new mediators. (A well-studied TeV-scale thermal DM is *weakly interacting massive particle* (WIMP), and the merit described above is known

as the "WIMP miracle".) On the other hand, the Lee-Weinberg bound [39] suggests that DM with $m_\chi \lesssim$ GeV and mediated by the weak scale mediators would lead to too low annihilation cross-section to match the observed relic abundance. As a result, the sub-GeV DM candidates are often categorized as "light" DM, and new mediators lighter than weak scale mass are warranted.

In the freeze-in scenario [40], DM interacts very weakly with the SM sectors that it never reaches chemical equilibrium with the thermal bath. While the interaction is feeble, the thermal bath does produce DM and gradually builds up the DM abundance as the universe expands. When the temperature T of the thermal bath drops below m_χ, there is no more energy to produce DM. Then, the DM abundance is "frozen-in" from the thermal bath. Considering two SM particles annihilate to two DM particles via a new mediator, we see that the thermally-averaged cross-section is $\langle \sigma v \rangle \sim \alpha_\chi \alpha_{\rm SM}/T^2$, where α_χ and $\alpha_{\rm SM}$ are the structure constants of DM and SM particles, respectively. This cross-section indicates that the thermal bath produces most of the relic DM at around the "freeze-in" point when $T \sim m_\chi$, and the freeze-in mechanism with a light mediator ($m_V \ll m_\chi$) is not sensitive to the initial conditions at the reheating.

We note that not all the freeze-in mechanisms require new mediators. A notable example is resonant and non-resonant sterile neutrino production [41–45]. This model considers a sterile (right-handed) neutrino state in the electroweak theory and allows a flavor oscillation between the active and sterile neutrino states through a non-zero active-sterile mixing angle. It has also been pointed out in Ref. [42] that a non-zero lepton asymmetry in the early universe give rise to a forward scattering potential of the active neutrinos and enhances the effective mixing angle between the active and sterile states through the Mikheyev-Smirnov-Wolfenstein (MSW) effect [46, 47]. The sterile neutrino DM produced by this way typically requires the mass to be above a few keV to satisfy the structure formation constraints.

In any case, introducing new mediators below the weak scale in both freeze-in and freeze-out mechanisms leads us to a plethora of DM candidates beyond the traditional WIMP paradigm. The new mediators allow the interactions between the DM and the SM sectors, enabling the thermal bath to produce DM. On the other hand, while the new mediators may

add new interactions within the SM sectors, the couplings must be small enough to satisfy any precision measurements.

Some of the well-studied portals are (1) neutrino portal with a sterile neutrino coupling to the SM lepton and the Higgs doublet, (2) Higgs portal with a scalar field coupling to Higgs doublets, (3) axion portal with a pseudo-scalar field coupling to SM fermions, and (4) kinetically mixing portal with a dark $U(1)$ field coupling to the SM $U(1)$ hypercharge.

In this thesis, we focus our attention on the kinetic mixing portal for its simplicity and the potentially rich phenomenology of outcomes. The simplest model for this portal is a vector dark photon kinetically mixed with the SM photon. An extension to it is introducing a Dirac fermion as DM that couples to the kinetically mixed dark photon. In the latter case, the Dirac fermion acquires a small fractional electric charge if the dark photon mediator is nearly massless, and the Dirac fermion DM in this scenario is called the "millicharged dark matter".

1.2.1 Dark photon

Dark photon is a new $U(1)$ vector that interacts with SM photons via the kinetic mixing portal. It acquires mass either from the Stueckelberg mechanism or from a new Higgs mechanism with new light degrees of freedom. Thermally-produced dark photons can come from the resonant photon-dark photon conversion or the couplings with the electromagnetic charge currents.

There have been extensive dark photon studies utilizing stellar and cosmological objects to constraints the model parameters. One example is the dark photon emission enhancement in the stars. The idea is that the dark photon mixing parameter is modified as the SM photons acquire the self-energy in the plasma. When the in-medium SM photon mass equals the dark photon mass, the dark photon production is greatly enhanced. This phenomenon plays significant roles in the Sun, the horizontal branch stars, and SN1987a, where the cooling rates could be altered by the in-medium dark photon emission [48, 49].

On the other hand, while the early universe has high density, only $\lesssim 5\%$ of freeze-in dark photon abundance is produced from the in-medium enhanced resonant emission. The rest of the

abundance comes from the non-resonant continuum emission. The reason is that the resonant emission happens only at a very narrow width of temperature. Thus the resonant emission only contributes a fraction of the abundance in the expanding universe. It is the non-resonant part that dominates the total freeze-in abundance of dark photons.

We note that the thermally produced dark photons never constitute a significant fraction of the DM abundance at any time in the early universe. While so, their production and decay still alter the Standard Cosmology. Here we consider the late-decay of dark photons during the weak decoupling epoch and look for the changes in radiation energy density and light element abundance. The key idea is that a decaying dark photon during weak decoupling releases entropy back to the SM plasma and neutrino seas which causes an additional entropy flow between the plasma sector and the neutrinos. This effect alters the time-temperature-scale factor relation and the phasing of the nuclear reactions involving light elements. The overall results are a more diluted radiation energy density and a slight change of primordial Deuterium yield.

In Chapter 3, we calculate the freeze-in abundance of dark photons and use the code burst to trace the evolution of nucleosynthesis numerically from the beginning of weak decoupling with the presence of late-decay dark photons. We exclude a range of dark photon model parameters using the 1%-level primordial deuterium abundance measurements from quasar absorption lines. Moreover, we also identify ranges of dark photon mass and couplings not yet constrained but perhaps accessible in future Stage-4 CMB experiments.

1.2.2 Millicharged dark matter

Millicharged dark matter (mDM) is a leading DM candidate and has been extensively searched in terrestrial DM experiments. It possesses a small fractional electric charge and interacts with the SM particles through long-range electromagnetic force. One motivation for this candidate is that the observed relic DM abundance can be obtained entirely through freeze-in of mDM for charges $q_\chi/e \sim 10^{-11} - 10^{-10}$, which is one or two orders of magnitudes smaller than the current direct detection bounds, $q_\chi/e \gtrsim 10^{-10} - 10^{-9}$ [50, 51].

The long-range interaction of mDM indicates that mDM interacts with baryons more strongly at low velocities or low momentum transfer. This feature enhances the DM-nuclei or DM-electron scatterings in the direct detection experiments. In addition, mDM has received significant interest following the observation of an anomalous absorption of radio frequency by the EDGES collaboration [52]. Because mDM interacts more strongly with baryons in the late times when the particle velocities have become lower, the anomaly could potentially be explained by the cooling of baryons relative to CMB photons from the mDM-baryon scattering at the Cosmic Dawn [53].

The discussions thus far are based on the particle-particle interaction of mDM. The interaction strength between the mDM and the SM sector is limited by their couplings and number densities. However, astrophysical and cosmological plasmas are often too tenuous to have any significant particle-particle scattering. Instead, it is the wave-particle interaction (i.e., each test particle scatters a collective plasma wave) that governs the dynamics of the plasma and the phase space of the particles.

In Chapter 4, we study the consequences of the long-range electromagnetic interactions of mDM in the supernova remnants. We investigate the plasma instabilities generated by the ambient mDM as the supernova shocks expand. Specifically, we will determine the mDM parameter space where the galactic mDM can be swept up by supernova shocks.

Chapter 2

Neutrino burst-generated gravitational radiation from collapsing supermassive stars

We estimate the gravitational radiation signature of the electron/positron annihilation-driven neutrino burst accompanying the asymmetric collapse of an initially hydrostatic, radiation-dominated supermassive object suffering the Feynman-Chandrasekhar instability. An object with a mass $5 \times 10^4 M_\odot < M < 5 \times 10^5 M_\odot$, with primordial metallicity, is an optimal case with respect to the fraction of its rest mass emitted in neutrinos as it collapses to a black hole: lower initial mass objects will be subject to scattering-induced neutrino trapping and consequently lower efficiency in this mode of gravitational radiation generation; while higher masses will not get hot enough to radiate significant neutrino energy before producing a black hole. The optimal case collapse will radiate several percent of the star's rest mass in neutrinos and, with an assumed small asymmetry in temperature at peak neutrino production, produces a characteristic linear memory gravitational wave burst signature. The timescale for this signature, depending on redshift, is ~ 1 s to 10 s, optimal for proposed gravitational wave observatories like DECIGO. Using the response of that detector, and requiring a signal-to-noise ratio SNR > 5, we estimate that collapse of a $\sim 5 \times 10^4 M_\odot$ supermassive star could produce a neutrino burst-generated gravitational radiation signature detectable to redshift $z \lesssim 7$. With the envisioned ultimate DECIGO design sensitivity, we estimate that the linear memory signal from these events could

be detectable with SNR > 5 to $z \lesssim 13$.

2.1 Introduction

In this paper we point out a surprising and serendipitous connection between the weak interaction physics of supermassive star (SMS) collapse to a black hole, the generation of a linear memory gravitational radiation signature from the neutrino burst that ensues in such an event, and the detection of this signature in proposed mid-frequency ($\sim 0.1\,\mathrm{Hz}$) gravitational wave observatories like DECIGO [34, 54].

We consider stars with a range of masses which falls into the category of the classic SMS of Fowler and Hoyle [27–30, 55], *i.e.*, $M \gtrsim 10^4\,M_\odot$. These are initially hydrostatic, high entropy, fully convective configurations, with the bulk of the mass-energy provided by baryon rest mass, but with the entropy and pressure support stemming predominately from the radiation field. The result is a star with adiabatic index perilously close to $4/3$, trembling on the verge of instability, and therefore ripe for destabilization by tiny (in this case) nonlinear effects inherent in General Relativity: the Feynman-Chandrasekhar post-Newtonian instability [31, 32]. There are many unresolved issues surrounding the formation and existence of such objects, their fate once they suffer the post-Newtonian instability, and the weak interaction and nuclear reaction history of the material in the collapsing star and the associated neutrino emission. We will not address these issues here, except insofar as they impact our key requirement for this work: an ultra-high entropy star that collapses to a black hole but remains essentially transparent to neutrinos until nearly the bitter end, when a black hole forms.

First, it must be pointed out that there exists no direct observational evidence, or even an indirect nucleosynthesis or chemical evolution argument that these stars ever existed. Moreover, even the question of whether nature could produce such objects remains unanswered. The existence of supermassive black holes (SMBHs) powering quasars at high redshift is indisputable [56–60]. This has long invited speculation on the origin of these SMBHs and about the

masses of "seed" black holes from which early SMBH could arise via mergers.

Begelman & Rees [10, 11] drafted a flow chart showing the routes to SMBH formation. Several of these include the formation of a SMS, either by suppression of fragmentation of a collapsing primordial gas cloud [14, 16–21], or by forming such an object in a dense star cluster via tidal gas stripping in close stellar encounters or by collisions [22–25]. In the primordial gas cloud collapse scenario, the outcome may depend on the gas accretion rate. High accretion can lead to a non-adiabatic configuration, essentially a compact object at the center with a distended lower density envelope [61, 62]. This will not produce the high entropy, fully convective (adiabatic) configuration we consider here. It is an open question whether a lower gas accretion rate, plus fragmentation suppression through heating or reduced cooling, can lead to this result. Certainly, stellar disruption or collision could produce a high entropy self-gravitating star, but this object might have relatively higher metallicity and therefore may explode via hot CNO hydrogen burning rather than collapse to a black hole [55].

Instead, we focus on the classic primordial metallicity hydrostatic SMS, completely convective, where the density, temperature, and pressure runs with radius are well described by a Newtonian index $n = 3$ polytrope, at least initially, prior to the onset of the post-Newtonian instability. Moreover, we point out here that if such a high entropy hydrostatic SMS *did* form, its subsequent collapse and neutrino emission can produce a unique gravitational wave burst signature, potentially detectable even for a collapse at very high redshift.

Gravitational radiation originating in the collapse of a rapidly rotating SMS to a black hole has been studied in Ref. [63]. That study found that most of the energy radiated in gravitational waves in SMS collapse is generated either by the time changing quadrupole moment of the baryons before trapped surface formation, or subsequent black hole ring down, all depending on the initial angular momentum content of the star. The gravitational wave signal produced this way will be a conventional, oscillatory one, well matched to proposed detectors in the mid- to low-frequency band.

Here we consider something quite different, both in the origin of the gravitational

radiation in a SMS collapse and in the nature and signature of this radiation in detectors. While the study in Ref. [63] centered on the effects of the bulk of the mass-energy, the baryons, in these objects, here we examine a complementary issue, the role of the very sub-dominant neutrino component in gravitational radiation production. Gravitational waves generated by the neutrino burst associated with ordinary core collapse supernovae and neutron star production is an old and well investigated idea [64–69], but these venues are eventually opaque to neutrinos and involve neutrino emission from a neutrino sphere. By contrast, we examine what happens in a star with significant neutrino emission, more than a few percent of the gravitational binding energy, yet has high enough entropy and therefore low enough density to be essentially transparent to neutrinos until near gravitational trapped surface formation. We will show how, unlike a *static* neutrino-transparent configuration, a collapsing but otherwise transparent SMS can "lock in" an asymmetry in neutrino emissivity and thereby generate a neutrino burst with a time-changing effective quadrupole moment.

Interestingly, since neutrinos emitted during the collapse are gravitationally unbound, the accompanying gravitational radiation generated by the neutrino burst will constitute what is termed gravitational waves with linear memory (GWM) [70–73]. A GWM is a non-oscillatory gravitational wave that leaves a net change in the gravitational wave strain after the signal has passed by.

The GWM effect was first discussed in its linear form in the 1970-80s [70–77]. For a recent review see Ref. [78]. In general, systems with more than one mass component gravitationally unbound to each other can produce gravitational waves with linear memory. Several such production mechanisms have been discussed, for example, hyperbolic binaries [72, 74], gamma-ray bursts [79], matter ejecta from supernova explosions [64–69], and anisotropic neutrino emission [75, 76]. The prospects for detecting the memory effect have been studied in Refs. [73, 77, 80].

This paper is organized as follows. In Section 2.2 we discuss the neutrino emission from SMSs. In Section 2.3 we estimate the strain magnitude of the gravitational wave signals from

this mechanism in collapsing SMSs and calculate the corresponding waveforms. In Section 2.4 we discuss the prospects for detection of these signals with the next generation space-based gravitational wave detectors. In Section 2.5 we discuss other possible sources which could also produce the linear GWM signal with strain magnitude and timescale similar to those originated from high-redshift SMS collapse. Throughout this paper we adopt geometric and natural units, $G = c = k_{\rm b} = \hbar = 1$, and assume ΛCDM cosmology with the closure fraction of the non-relativistic component chosen as $\Omega_{\rm M} = 0.3$, the vacuum energy contribution to this fraction taken as $\Omega_\Lambda = 0.7$, and the Hubble parameter at the current epoch in units of $100\,{\rm km\,s^{-1}\,Mpc^{-1}}$ taken to be $h = 0.7$.

2.2 Characteristics of SMSs

2.2.1 Total neutrino energy from the collapsing SMS

A hydrostatic, fully convective SMS with stellar mass $M_{\rm SMS} \gtrsim 5 \times 10^4\, M_\odot$ has a structure well represented by an $n = 3$ polytrope. It is radiation dominated and most of its entropy is carried by photons and electron/positron pairs. The entropy per baryon in units of Boltzmann's constant $k_{\rm b}$ is typically $s \approx (M/M_\odot)^{1/2} \approx 300\left(M_5^{\rm HC}\right)^{1/2}$, where $M_5^{\rm HC}$ is the homologous core mass in units of $10^5\, M_\odot$ [33]. As the SMS gradually radiates away energy and shrinks in radius, the star eventually suffers post-Newtonian instability and begins to collapse. For $M^{\rm HC} \sim 10^5\, M_\odot$, instability sets in roughly at the onset of hydrogen burning. A fraction, likely a few tens of percent, of the initial stellar mass may collapse homologously, depending on the history of neutrino energy loss, nuclear burning and initial angular momentum content and distribution [55]. It's this homologous core that produces the initial BH.

The gravitational binding energy liberated in the collapse is $E_s \sim M^{\rm HC}$. Most of this energy is trapped in the BH, but a small fraction will be radiated as neutrinos. These neutrinos are produced mostly via electron/positron pair annihilation into neutrino pairs. Since the rate of the energy emissivity of this neutrino pair production channel is proportional to a high power of

the temperature, $\propto T^9$ [81–83], the bulk of the radiated neutrino energy will be produced very close to the BH formation point, where the temperature is the highest. Just how high the plasma temperature gets before redshift associated with gravitational trapped surface formation cuts off neutrino escape depends on details of SMS evolution, e.g., nuclear burning and convective timescales during the collapse, and on the collapse rate near BH formation.

Shi & Fuller [33] estimated that the total neutrino energy emitted during the collapse of a non-rotating SMS as $3.6 \times 10^{57} \left(M_5^{\rm HC}\right)^{-0.5}$ ergs in a timescale $\Delta\tau = M_5^{\rm HC}$ s. More sophisticated hydrodynamic simulations conducted by Linke et al. [84] show that the innermost 25% of the SMS mass will collapse homologously to a BH, emitting neutrinos on a timescale approximately 11 times longer than estimated by Shi & Fuller. In the mass range $10^5\,M_\odot \lesssim M^{\rm HC} \lesssim 5 \times 10^5\,M_\odot$, they calculate the total energy emitted in neutrinos to be approximately 3% of what was found in Shi & Fuller. Though still a substantial amount of energy, this result shows a considerable discrepancy with Shi & Fuller. The difference between these calculations reflect the different ways in which neutrino emission and redshift near the BH formation point were calculated. In turn, this physics is dependent on the treatment of in-fall and collapse timescales, pressure, and the adiabat of collapse. The Linke et al. calculation likely is more realistic, as it gives a self consistent calculation of neutrino emission coupled to collapse dynamics and redshift. Nevertheless large uncertainties remain in the physics "upstream" of the BH formation point. Consequently, we will consider both calculations in our assessment of the neutrino burst-generated linear memory gravitational wave signal from SMS collapse.

The calculations in Ref. [33] do not apply for $M_5^{\rm HC} \lesssim 0.1$, *i.e.,* where neutrinos may be trapped via scattering on electrons and positrons. For example, a homologous core with mass $M_5^{\rm HC} = 0.1$, close to BH formation, has a neutrino mean free path smaller than the Schwarzschild radius. We conclude that for $M_5^{\rm HC} \lesssim 0.1$ the homologous core will be subject to neutrino scattering-induced trapping and is opaque to neutrinos. It is likely that a significant fraction of neutrinos will be carried into, and trapped inside, the BH in this case.

At higher SMS masses, a smaller fraction of the SMS rest mass is radiated as neutrinos

even though the total gravitational binding energy released in the collapse is higher. This stems from the fact that electron/positron pair annihilation neutrino emissivity scales as the ninth power of the temperature, whereas the temperature scales as $(M^{\rm HC})^{-1/2}$. At large SMS mass the core will not get hot enough to radiate a significant fraction of E_s before BH formation. When $M_5^{\rm HC} \gtrsim 10$, less than 0.1 percent of the homologous core gravitational binding energy would be emitted as neutrinos.

Subject to scattering-induced neutrino trapping at low SMS masses, and low neutrino emissivity at high SMS masses, the optimal mass range of the homologous core for a maximal fraction of the SMS mass to be radiated in neutrinos is $5 \times 10^4\, M_\odot < M^{\rm HC} < 5 \times 10^5\, M_\odot$.

As discussed above, there remain open questions in the evolution and collapse physics of SMSs. These issues can be relevant for the neutrino burst accompanying SMS collapse. In part, uncertainties in the characteristics of the eventual neutrino burst arise from the fact that the total energy, internal plus gravitational, of these objects near their instability points will be very close to zero. Relatively small changes in nuclear burning history or neutrino emission history may lead to significant subsequent alterations in the thermodynamic history of collapse. During the collapse, neutrino emission and escape remove entropy from the star, while nuclear burning in effect counters this by adding entropy. By far the biggest effect is the former, entropy loss, but the latter entropy source helps determine the entropy content relevant for peak neutrino emission just before the BH formation point. The small effect from nuclear burning in making the entropy, and hence temperature, slightly higher can be significant because the neutrino emission rate from electron/positron pair annihilation scales as the ninth power of the temperature. Though there is negative feedback between the competing processes of neutrino engendered entropy loss and added entropy from nuclear burning, in the end nuclear burning will mean stronger neutrino emission overall and a larger fraction of the homologous core rest mass radiated as escaping neutrinos.

That is, as long as the energy production from nuclear burning is not large enough, or not optimally phased in time or location, so as to cause the thermonuclear explosion and disruption

of the star! An explosion caused by nuclear burning early in the collapse obviously precludes production of a BH. The lower end of our considered range of SMS masses may be the most vulnerable to the uncertain details of the phasing and interplay of nuclear burning, convection, rotation, and neutrino emission. For example, the calculation reported in Ref. [85] suggested that for a narrow range of SMS masses around $5.5 \times 10^4 M_\odot$ "explosive" helium burning immediately subsequent to the post-Newtonian instability point would be sufficient to cause an explosion of the star, even with primordial metallicity at SMS formation. This calculation highlights the outstanding uncertainties associated with SMS evolution up to the instability point and subsequently.

2.2.2 Creating an anisotropic neutrino energy flux

There can be another consequence of electron/positron annihilation-generated neutrino energy emission being proportional to nine powers of temperature [81–83]. Because of this high sensitivity to the temperature, even a small anisotropy in the temperature can translate into an order of magnitude larger neutrino emissivity anisotropy. For example, a configuration with a 2.5% lower temperature at the equator than at the poles will have an approximately 25% neutrino emissivity asymmetry between volume elements along the equatorial plane and the polar direction.

In the SMSs we consider here, the bulk of the pressure, P, comes from relativistic particles, implying that $P \propto T^4$. Therefore $\delta P/P = 4\delta T/T$. So a 2.5% decrease in temperature corresponds to a 10% decrease in pressure. A rotation-driven centrifugal acceleration decreases the required pressure support in the star's equatorial plane relative to its polar direction. Interestingly, 10% difference in pressure between the equator and pole on a 2-sphere near the maximum neutrino emissivity point, in turn, likely would not significantly change the free-fall collapse time there. For $M^{\rm HC} = 10^5 M_\odot$, an angular speed of $\omega \sim 0.22\,{\rm rad\,s^{-1}}$ at BH formation, corresponding to dimensionless angular momentum of $J/M^2 \sim 0.18$, would produce a 25% neutrino energy emissivity anisotropy.

If the SMS is both transparent to neutrinos and static, this emissivity asymmetry would not be imprinted on the neutrinos escaping to infinity. The reason for this is simple: Neutrino emission from each volume element in the core will produce a symmetric neutrino emission pattern, radiating neutrinos isotropically, and in a completely neutrino-transparent, spherically symmetric star where each volume element is at rest, the neutrino radiation seen by distant observers will be spherically symmetric and static. However, many of these conditions are violated in a real, collapsing star. A collapsing star, where fluid elements *move*, will lock-in some of the temperature variation-created local emission anisotropy discussed above. The mechanism for this is rooted in the non-equivalence of neutrino directions in the collapsing star and, in particular, a direction-dependent differential blueshift-redshift akin to the integrated Sachs-Wolfe (ISW) effect in cosmology [86].

Neutrinos emitted into an inwardly-directed pencil of directions will escape from the star with significantly less energy flux than they were born with. Of course, that is true for any redshifted neutrino, but the point here is that the extent of the unbalanced blueshift-redshift is emission angle-dependent. This breaks spherical symmetry in the neutrino-transparent star. Neutrinos will gain energy, i.e., experience blueshift, as they stream toward the center of the star (homologous core or BH) and lose energy, suffer redshift, as they stream away from the center. However, the key point is that this geometry is not *static*, and the SMS is collapsing. In the time frame over which most of the neutrinos are produced, the SMS has significantly collapsed, causing the gravitational potential well to become correspondingly deeper. Consequently, the redshift will be larger than the blueshift. This represents a net gravitational redshift, along with absorption by the BH (the ultimate gravitational redshift) for some neutrino directions, implying that although the emission from a given incremental volume element is isotropic, the redshift and absorption of neutrinos produced by this volume element is not. Fig. 2.1 illustrates the geometry of this differential blueshift-redshift effect. This is how a net anisotropy in the neutrino emission from the SMS, as observed by a distant observer, can be generated.

In Appendix 2.C, we present an order of magnitude estimate of the transformation of a

neutrino emissivity anisotropy, η, (caused by, *e.g.*, modest SMS rotation) to a neutrino energy flux asymmetry, α, as measured by a distant observer, by this ISW-like mechanism. We stress that the model in the Newtonian treatment in Appendix 2.C is meant to be an order of magnitude estimate and is not meant to be a detailed analysis of the many general relativistic effects that may affect the result, which is beyond the scope of this work. Nevertheless, our intriguing results suggest that such a fully general relativistic study is warranted.

There are two important results from the Newtonian model in Appendix 2.C: that the neutrino energy flux asymmetry has the opposite sign from the neutrino emissivity asymmetry; and that is an order of magnitude smaller. If a rotation-created temperature asymmetry resulted in an $\eta = 0.25$ neutrino emissivity asymmetry, where mass elements at the poles emit 25% more neutrino energy than those at the equator, the ISW-like effect would result in an $\alpha \sim -0.02$ neutrino energy flux asymmetry, where the SMS emits roughly 2% less neutrino flux in the polar direction than the equatorial direction. This assumed number for rotation-induced temperature anisotropy is chosen for illustrative purposes only, with only the proviso that the rotation speeds be so modest as to not alter the collapse significantly.

Note that α and η have opposite signs. This is because the more emissive polar regions ($\eta > 0$) will create more neutrino energy flux in the equatorial directions than polar directions. This is because the inward directed flux will be suppressed by the ISW-like effect. In addition, α is smaller in magnitude than η because of an averaging effect over outward directed neutrino trajectories that reduces the size of the asymmetry.

Several factors stemming from the strong gravitational field and relativistic environment might also alter the neutrino energy flux asymmetry. Direction beaming effects will be most important when the matter moves at relativistic velocity. This will happen only near the BH formation point. In spite of that, the redshift will dominate over the beaming effects whenever the in-falling fluid elements are moving close to the speed of light [87]. As a result, the beaming contribution to the neutrino luminosity should not be dominant. Another factor to consider is the deflection of neutrino trajectory in the strong gravitational field regime. Again, reference [87],

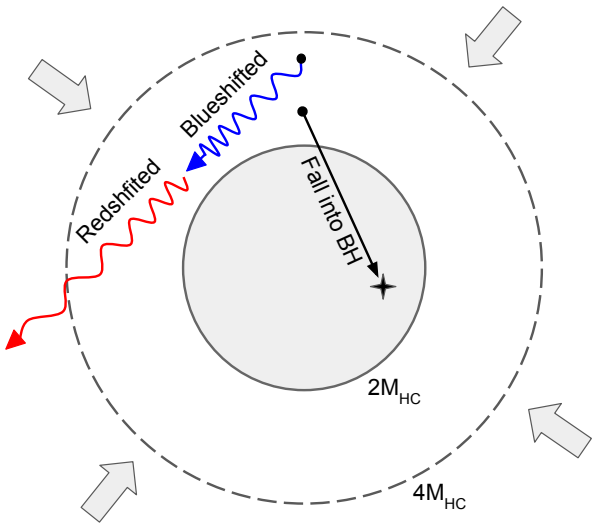

Figure 2.1. Illustration of anisotropic neutrino emission production by the integrated Sachs-Wolfe-like effect. Neutrinos moving toward the central core may fall into the BH or suffer an ISW-like differential blueshift-redshift effect driven by the increase of gravitational potential with time in a collapsing SMS.

studying the neutron star regime, shows that where this effect is significant, redshift is dominant. Just how significant the null trajectory-bending effect could be in altering the neutrino emission asymmetry requires a fully general relativistic simulation, which is beyond the scope of this paper.

2.3 Gravitational waves from anisotropic neutrino emission

Anisotropic neutrino energy transport and emission can radiate gravitational waves so long as there is a time-changing quadrupole moment in the neutrino flux. This type of gravitational wave signal was first analyzed by Epstein [75]. Since then the formalism has been applied to core-collapse supernovae in several studies [64–69].

In this paper, we use the same formalism but deal with a completely different object and environment. SMSs have mass density several orders of magnitude lower than the density of core-collapse supernovae. Even at the onset of black hole formation, the density in the center of the SMSs we consider is no more than $10^9\,\mathrm{g\,cm^{-3}}$, while the density of core-collapse supernovae

reaches nuclear matter density, $\sim 10^{14}\,\mathrm{g\,cm^{-3}}$, or higher. In core-collapse supernovae anisotropy in the neutrino emission and outgoing neutrino flux stems from inhomogeneity on the surface of the neutrino-sphere, roughly the proto-neutron star surface. By contrast, as discussed in the last section, in the SMS case anisotropy in the neutrino emission and outgoing flux is produced by temperature anisotropy in the homologous core.

2.3.1 Collapsing SMSs and gravitational radiation

Consider the collapse of a SMS that anisotropically emits a burst of neutrinos with total energy $E_{\nu,\,\mathrm{loss}}$ over a burst time scale Δt. The gravitational wave strain measured distance d away from this prodigious neutrino burst can be estimated with the quadrupole moment approximation, $h \approx 2\ddot{I}/d$. If α represents the polar-equatorial neutrino emission asymmetry, the neutrino mass-energy density will have an asymmetric component $\alpha E_{\nu,\,\mathrm{loss}}/(4\pi R^2 \Delta t)$, where R is the radius of the homologous core. This corresponds to a quadrupole moment $I = \alpha E_{\nu,\,\mathrm{loss}} R^3/(15\Delta t)$.

The characteristic neutrino burst time is the dynamical timescale of the collapsing homologous core, which is approximately the light crossing time across the homologous core near BH formation, $\Delta t \approx 2M^{\mathrm{HC}}$. This is also roughly the free-fall time near BH formation. Because of the steep temperature dependence of $e^{\pm}$-pair annihilation neutrino energy emissivity, most neutrinos are radiated close to BH formation. Consequently, we take R as the Schwarzschild radius of the homologous core, $2M^{\mathrm{HC}}$. Assuming the total energy release in neutrinos is a fraction β of the homologous core rest mass, the gravitational wave strain can be estimated as

$$h \approx 6.5 \times 10^{-20} \alpha\beta \left(\frac{M^{\mathrm{HC}}}{10^5\,M_\odot}\right)\left(\frac{10\ \mathrm{Gpc}}{d}\right). \tag{2.1}$$

Note that cosmological redshift will increase the burst duration at the detector. The neutrino burst time Δt in the source's rest frame (including SMS gravitational redshift effects) will be redshifted to $\Delta t_m = \Delta t\,(1+z)$ in the detector's rest frame. Table 2.1 shows the characteristics of gravitational wave signals from collapsing SMSs at redshift $z = 7$ and with a 2% neutrino

Table 2.1. Gravitational waves from collapse of SMS at redshift 7 with a 2% neutrino emission asymmetry.

$M^{\rm HC} = 1 \times 10^5\, M_\odot$	Shi & Fuller	Linke et al.
$E_{\nu,\ \rm loss}$	3.6×10^{57} erg	1.1×10^{56} erg
Fraction of rest mass β	2×10^{-2}	5×10^{-4}
GW strain h	3.0×10^{-23}	8.3×10^{-25}

emission asymmetry. This table presents these estimates for two different calculations of $E_{\nu,\ \rm loss}$.

Of course, the strain derived by using Eq. (2.1) is only an order-of-magnitude estimate. One flaw in this estimate is the approximation of the time-derivative as the inverse of the characteristic neutrino burst time, which would imply a single-frequency wave. However, because the neutrinos emitted during SMS collapse are gravitationally unbound, the gravitational wave generated by the neutrino burst is a GWM with broad-band characteristics. To get the correct power spectrum of the gravitational radiation, one should include Fourier components at all frequencies. Nevertheless, Eq. (2.1) serves to capture the GWM strain amplitude to be expected from the time-changing energy flux and quadrupole moment of the neutrino field associated with SMS collapse.

2.3.2 Neutrino burst-generated gravitational waves with memory

We follow the formalism in Ref. [75] to calculate the key features of the form of the gravitational wave with memory (GWM) generated by neutrino emission in SMS collapse. These results also can be derived via a time-changing quadruple moment approach, as detailed in Appendix 2.A. The gravitational wave measured at time t by an observer at distance d from the SMS source was generated by that source at retarded time $t' = t - d$. The corresponding

dimensionless gravitational wave strain is [65, 75]

$$\Delta h_{+}^{\mathrm{TT}} + i\Delta h_{\times}^{\mathrm{TT}} = \frac{2}{d}\int_{-\infty}^{t-d} L_{\nu}\left(t'\right) dt' \int F\left(t', \Omega'\right)\left(1+\cos\theta\right) e^{i2\phi}\, d\Omega' \tag{2.2}$$

where $L_{\nu}\left(t'\right)$ is the neutrino energy luminosity at the retarded time, $F\left(t', \Omega'\right)$ is the emission angular distribution function and $d\Omega' = \sin\theta'\, d\theta'\, d\varphi'$ is the solid angle enclosing the source. The superscript TT denotes the transverse traceless gauge and "strain" is the metric deviation, which is identical to the trace reverse in this gauge. Here we introduce the detector's (observer's) frame xyz and the source frame $x'y'z'$, as shown in Fig. 2.5 in Appendix 2.A – the detector is at a distant location d along the observer's z-axis in this figure. With the orientation of axes in this figure, the two gravitational wave polarizations at the detector are $h_{+}^{\mathrm{TT}} \equiv h_{xx}^{\mathrm{TT}} = -h_{yy}^{\mathrm{TT}}$ and $h_{\times}^{\mathrm{TT}} \equiv h_{xy}^{\mathrm{TT}} = h_{yx}^{\mathrm{TT}}$.

To simplify the calculation, we take the emission angular distribution to be time-independent and axisymmetric about the z' axis:

$$F\left(\Omega'\right) = \frac{1+\alpha\cos^2\theta'}{4\pi\left(1+\alpha/3\right)}. \tag{2.3}$$

The angular distribution of neutrino emission is enhanced at the two poles relative to the equator when $\alpha > 0$, and in the equatorial plane relative to the poles when $\alpha < 0$. The scenario that we describe in Sec. 2.2.2 has $\alpha < 0$. Because of the ϕ'-independence of the emission distribution in Eq. (2.3), it can be shown that the only relevant polarization in Eq. (2.2) is "plus" polarization, $h_{+}^{\mathrm{TT}} = h_{xx}^{\mathrm{TT}} = -h_{yy}^{\mathrm{TT}}$.

After integration over all solid angles in Eq. (2.2), the gravitational wave strain is:

$$\Delta h_{+}^{\mathrm{TT}} = \Delta h_{xx}^{\mathrm{TT}} = -\Delta h_{yy}^{\mathrm{TT}} = \frac{E_{\nu\ \mathrm{loss}}}{d} \times \frac{\alpha\sin^2\xi}{3+\alpha}. \tag{2.4}$$

As expected, the gravitational wave strain is zero when the detector is located along the polar

axis of the source ($\xi = 0$ or π) and maximal in magnitude when the detector is located in the source's equatorial plane ($\xi = \pi/2$).

As noted, the gravitational wave signal generated by anisotropic neutrino emission is a GWM. The "memory" effect is so named because this gravitational wave type results in a nonzero net strain after the signal has passed the detector. In other words, its passage imprints a permanent proper displacement between two freely falling masses. The GWM waveform in the time-domain would look like a DC offset signal, but with a rise time Δt_m:

$$h(t) = \begin{cases} 0 & t < -\Delta t_m, \\ \Delta h_{xx}^{\mathrm{TT}} (1 + t/\Delta t_m) & -\Delta t_m < t < 0, \\ \Delta h_{xx}^{\mathrm{TT}} & t > 0, \end{cases} \tag{2.5}$$

where $\Delta h_{xx}^{\mathrm{TT}}$ is calculated in Eq. (2.4).

2.4 The Signal To Noise Ratio

In this section we compute the signal-to-noise ratio of the neutrino burst-generated gravitational wave signals and we consider the prospects for detecting these signals with space-based laser interferometry. The sky-averaged squared signal-to-noise ratio is $\langle \mathrm{SNR}^2 \rangle = \int_0^\infty [h_c(f)/h_n(f)]^2 \, df/f$. Here $h_c(f)$ is the GWM's characteristic strain at frequency f and is defined as

$$h_c(f)_{\mathrm{mem}} = 2f \langle |\tilde{h}_+(f)|^2 \rangle^{1/2}, \tag{2.6}$$

where $\tilde{h}_+(f)$ is the Fourier transform of the GWM plus-polarization strain (metric deviation) in Eq. (2.5):

$$\tilde{h}_+(f) = \Delta h_{xx}^{\mathrm{TT}} \frac{-ie^{-\pi i f \Delta t_m}}{2\pi^2 f^2 \Delta t_m} \sin(\pi f \Delta t_m). \tag{2.7}$$

The $\langle ... \rangle$ in Eq. (2.6) denotes the average over the sky position and polarization of the source, *i.e.*, the average over ξ. $h_n(f)$ is the characteristic detector noise amplitude obtained after taking the

average of sky-location and polarization angle, *i.e.*, $h_n(f) = \sqrt{fS_n(f)}/\langle F_+^2(\theta,\phi,\psi)\rangle^{1/2}$, where $S_n(f)$ is the detector's one-sided noise spectral density and $F_+(\theta,\phi,\psi)$ is the detector's beam pattern function. The value of $\langle F_+^2\rangle$ for detectors like DECIGO and BBO is $1/5$, and 3/20 for detectors like LISA [80, 88–90].

In the low frequency limit where $f \ll 1/\Delta t_m$, Eq. (2.7) becomes $\tilde{h}(f) = \Delta h/2\pi i f$ and the dimensionless characteristic strain h_c approaches a frequency-independent value $\Delta h/\pi$ (here we use Δh to denote generically the metric deviation signals referred to above, e.g., $\Delta h_{xx}^{\mathrm{TT}}$, etc.). This is one of the interesting properties of the gravitational wave memory effect. These low frequency characteristics of GWM are sometimes referred to as the "zero frequency limit" [71, 76, 91].

In general, detectors with high sensitivity at low frequency are ideal for memory-type gravitational waves detection. Consider, for example, the pulsar timing array (PTA) [92, 93], which is most sensitive in the nano-Hertz frequency band. A gravitational wave memory signal in this band that can be treated as an extreme low frequency wave is potentially "audible" to PTA. But one important factor that limits the sensitivity of the PTA in detecting GWM signals is the resolution of the best clock in the world. The pulse arrival time shifted by gravitational waves is $\Delta t/t \sim \Delta h$; on the other hand, the stability of the best clock, which has a strain sensitivity at a level $\sim 10^{-15}$ after integrating the data for 10 years [94], is still far short of what is required to detect gravitational waves from collapsing SMSs, where we might expect $\Delta h \sim 10^{-23}$.

Fortunately, space-based gravitational wave detectors, for example DECIGO and BBO [35, 36], with optimal sensitivity to frequencies in the deci-Hertz band, and high peak sensitivity ($h_c \sim 10^{-24}$), could be ideal for detecting GWM from neutrino bursts from SMS collapse. Serendipitously, the SMS homologous core mass range giving the largest fraction of rest mass radiated as neutrinos also produces GWM with frequencies more or less coincident with the optimal sensitivity frequency range for DECIGO and BBO.

Figure 2.2 shows a comparison between the Shi & Fuller and Linke et al. integrated neutrino luminosity results for the sky-averaged characteristic strains of the SMS neutrino burst-generated GWM signals estimated here. LISA is a gravitational wave interferometry antenna in

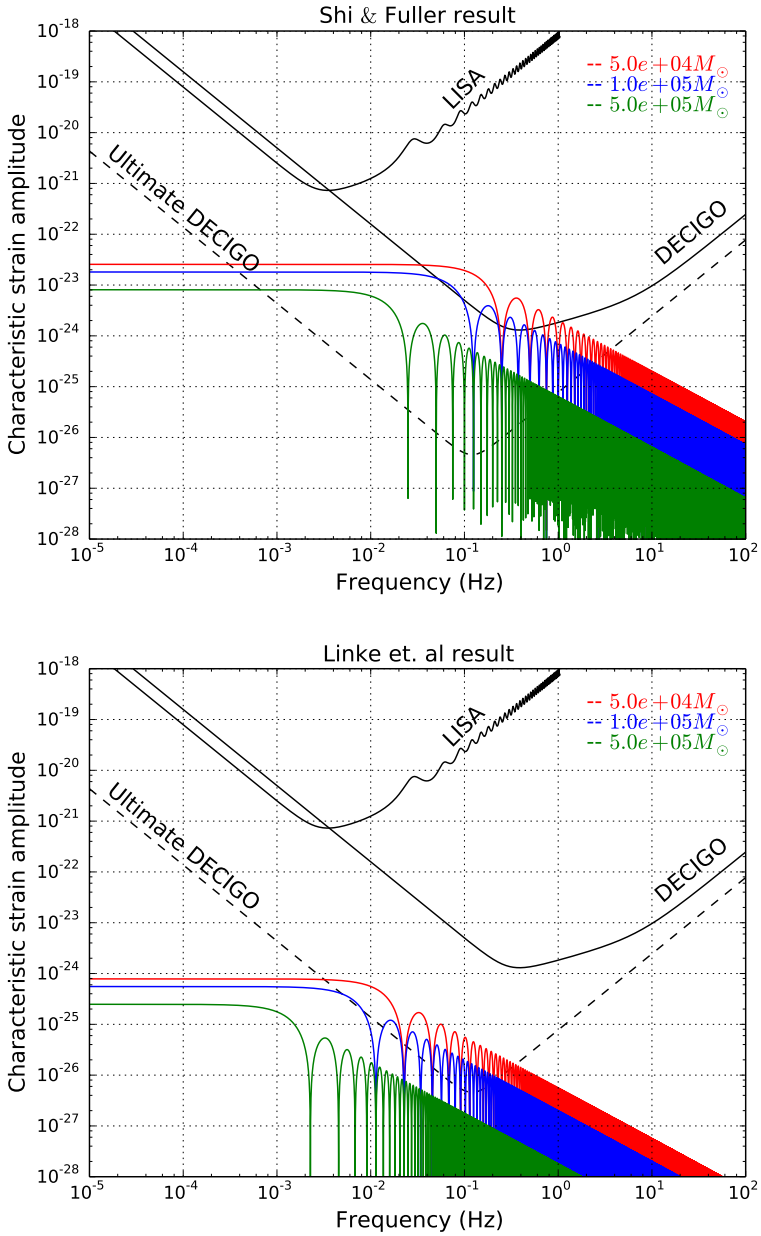

Figure 2.2. Sky-averaged characteristic strain h_c as a function of frequency from the neutrino burst-generated GWM signal accompanying the collapse of SMSs at $z = 7$, with $\alpha = -0.02$ and with homologous core masses $5 \times 10^4\, M_\odot$ (red curve), $10^5\, M_\odot$ (blue curve) and $5 \times 10^5\, M_\odot$ (green curve), as labeled. The panels on the top and the bottom are based on the results for integrated neutrino luminosity from Shi & Fuller and Linke et al., respectively. The two black solid lines and the black dash line denote the sky-averaged noise curves for LISA, DECIGO and Ultimate DECIGO, as labeled.

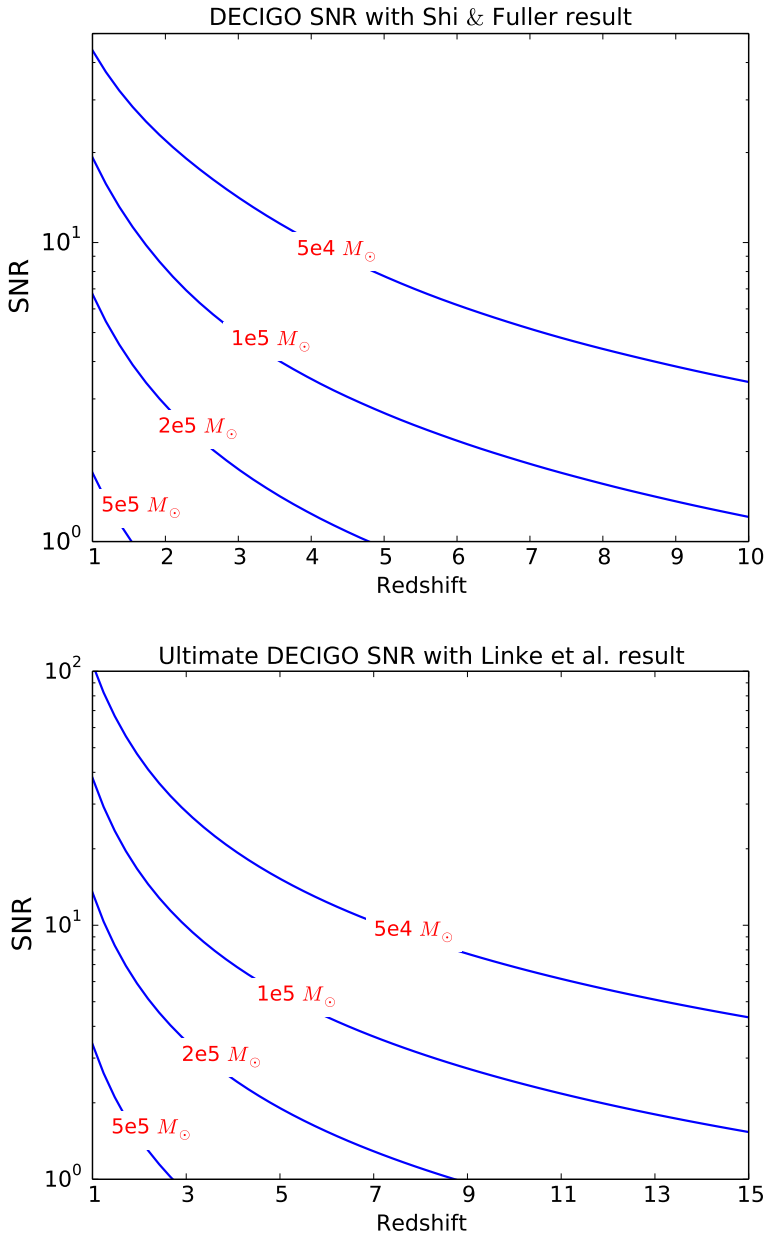

Figure 2.3. The vertical axes in the top and bottom panels show sky-averaged signal-to-noise ratios SNR for DECIGO with the Shi & Fuller result and Ultimate DECIGO with Linke et al. result for overall neutrino burst characteristics, respectively. Here we take asymmetry parameter $\alpha = -0.02$. Each contour line denotes the final homologous core mass of a collapsing SMS, as labeled.

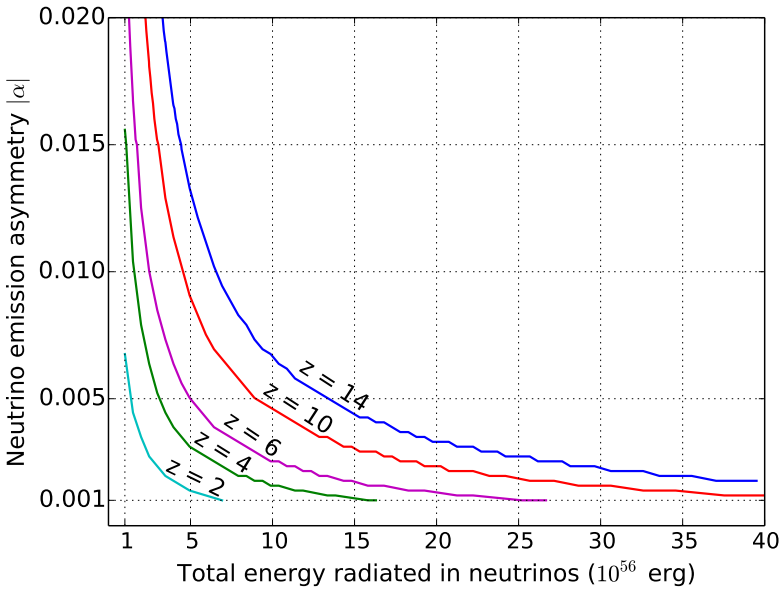

Figure 2.4. Contours of detectability redshift z (as labeled) as a function of the neutrino emission asymmetry and the total energy radiated in neutrinos. These results were calculated assuming an SMS homologous core mass $M^{\rm HC} = 10^5\,M_\odot$ with neutrino burst time calculated with the Linke et al. result. Each contour curve shows the redshift for which SNR = 5 for Ultimate DECIGO.

Earth-like solar orbit with arm length 2.5 Gm [95]. With the currently envisioned LISA design sensitivity, the gravitational wave signal from the collapse of SMSs at $z \gtrsim 0.1$ is too weak to be detected, for both results for overall neutrino emission.

DECIGO is also a gravitational wave interferometry antenna in Earth-like solar orbit, but with a 1000 km arm length and covering the mid-frequency (~ 0.1 Hz) gravitational wave band with $h_{\rm rms} \sim 2 \times 10^{-24}$ [54]. Its high sensitivity at $f \sim 0.1$ Hz is ideal for the detection of SMS neutrino burst-generated gravitational wave signals which have characteristic timescale $\sim$ 1 s to 10 s. With the Shi & Fuller result, a GWM signal for an SMS with $M^{\rm HC} \approx 5 \times 10^4\,M_\odot$ will be "audible" with DECIGO (here assuming a basic "set" [90] of detectors) at $z = 7$, and much higher redshifts for envisioned ultimate DECIGO design parameters [54]. The Linke et al. result has about a factor of 30 lower total neutrino energy release and a factor of 11 longer neutrino emission time than the Shi & Fuller result. These differences imply a reduction in strain amplitude and lower signal frequencies relative to results of calculations carried out

with the Shi & Fuller estimates. With the Linke et al result, a GWM signal for an SMS with $M^{\rm HC} \approx 5 \times 10^4 M_\odot$ is too faint to be seen at $z \gtrsim 0.1$ with the basic DECIGO configuration, but will be detectable with Ultimate DECIGO at $z = 7$.

Figure 2.3 gives examples of the expected SNR for our estimated SMS neutrino burst-generated GWM as a function of redshift for a range (contours) of homologous core masses. The results shown in this figure use both the Shi & Fuller (top panel) and Linke et al. (lower panel) estimates for overall neutrino burst luminosity. In each of these example calculations we take the neutrino energy flux asymmetry parameter to be $\alpha = -0.02$. This figure provides insight into the prospects for detection of these GWM signals. We show (upper panel) the most optimistic estimate of neutrino burst luminosity and most favorable (highest) rest frame frequency paired with the least sensitive version of DECIGO, and the least favorable estimate of neutrino emission and rest frame frequency range paired with the most sensitive and capable version of DECIGO planned, i.e., "Ultimate" DECIGO. Based on Shi & Fuller result, the GWM signal for an SMS with $M^{\rm HC} = 5 \times 10^4 M_\odot$ and $\alpha = -0.02$ could be detected by DECIGO with SNR > 5 out to redshift 7. With the same mass and asymmetry, the GWM signal with Linke et al. result is not detectable with basic DECIGO, but is detectable by Ultimate DECIGO with SNR > 5 out to redshift 13.

Figure 2.4 provides insight into detectability of neutrino-burst-generated GWM. In this figure we show contours of detectability redshift as a function of neutrino emission asymmetry and the total energy radiated in neutrinos for a SMS with homologous core mass $M^{\rm HC} = 10^5 M_\odot$. Here the contours of redshift "detectability" indicate a SNR≥ 5 in Ultimate DECIGO. The total neutrino emission for this particular example is 3.6×10^{57} ergs, as calculated with the Shi & Fuller neutrino emission result and approximately 10^{56} ergs with Linke et al. result. All of these estimates are intriguing, suggesting that deci-Hertz gravitational wave detectors may be able to probe massive black hole production and associated physics at redshifts at, and even well beyond, those of the epoch of re-ionization.

SMS collapse events with a given mass and given neutrino emission asymmetry could

be detected to even larger distances if nuclear burning prior to, or during, collapse causes the entropy to increase, in turn causing a larger fraction of SMS rest mass to be radiated as neutrinos. But nuclear burning and rotation also can decrease the chances for detection of SMS neutrino bursts.

In this vein, we should emphasize that all of our estimates are rough, and many issues in SMS physics remain open, as discussed above in Sec. 2.2. For example, the neutrino emission calculations in both Shi & Fuller and Linke et al. results do not include the possible effects of nuclear burning on the SMS's collapse adiabat, nor do they incorporate the phasing of this nuclear energy input with the post-collapse build-up of infall kinetic energy in the homologous core. Moreover, if significant pressure or centrifugal support resists the free fall of the homologous core, more neutrinos can be emitted, as there is more time for emission before the formation of a trapped surface. As a consequence of this effect, however, peak neutrino emission will be shifted to a lower frequency because the collapse time will be longer than the free-fall time near the BH formation point. As illustrated by the examples in Fig. 2.2, shifting the frequency of the neutrino burst-generated GWM to the low side of the DECIGO peak sensitivity frequency range impairs that detector's ability to "see" these signals at the higher redshifts.

On the other hand, the rapid release of nuclear binding energy may destroy the star in an explosion instead of forming a large remnant BH. Of course, this results in much less total neutrino emission. The calculation reported in Ref. [85] suggests a possible narrow SMS mass window, centered around $M_{\rm SMS} \approx 5.5 \times 10^4 M_\odot$, where a non-rotating, primordial (zero) metallicity SMS could experience rapid, "explosive" helium burning beginning just after the conclusion of hydrogen burning and in close coincidence with the post-Newtonian instability point. This could result in thermonuclear explosion, as not much infall kinetic energy will have been built up prior to the helium burning energy injection. Moreover, the coincidence of the triple-alpha ignition point and the onset of instability is likely what limits the SMS mass range for this behavior and targets the lower masses in the range of masses considered here – only the lower end our mass range would have a stable main sequence.

SMS produced at later epochs, or in scenarios involving tidal disruption or stellar coalescence in a dense star cluster, may have small but non-zero initial metallicity. These could also experience thermonuclear explosion rather than collapse to a BH. A small initial carbon, nitrogen, or oxygen (CNO) content could facilitate hydrogen burning via the CNO cycle, and thereby allow an *early* break-out into the rp-process. In turn, this break-out would result in a greater rate at which nuclear energy is added as compared to that in the proton-proton hydrogen burning regime characterizing the early stages of collapse in initially zero metallicity SMSs. Nuclear energy addition *immediately* after the post-Newtonian instability point, before the build-up of an infall kinetic energy "debt," enhances the chances for thermonuclear explosion.

Rotation can also enhance these chances. The study in Ref. [96] shows that a rotating SMS with a mass $M_{\rm SMS} \approx 5 \times 10^5\, M_\odot$ at initial angular speed $\gtrsim 2.5 \times 10^{-5}$ rad/s reduces the metallicity threshold for thermonuclear explosion to $Z_{\rm CNO} \approx 0.001$. Their result for a star that explodes this way shows a decrease of 10 orders of magnitude in total neutrino loss rate relative to a model that collapses to a BH. In any case, post-instability thermonuclear explosion of an SMS will decrease the total energy radiated in neutrinos and, at the same time, increase the neutrino burst timescale relative to that of a SMS that collapses to a BH. These features decrease the prospects for detecting a neutrino burst-generated GWM signal.

2.5 Other possible GWM sources

There are several other astrophysical sources which could produce a linear memory GWM signal with strain magnitude and overall timescale similar to those originating from a neutrino burst associated with a high-redshift SMS collapse. If a space-based laser interferometer gravitational wave observatory were to record a signal with characteristics along the lines of what we discuss above, how would we know it was actually a SMS collapse-generated GWM? Direct neutrino detection could constitute a confirmation, as the time dependence of the neutrino signal in principle could tag the event as having a SMS collapse origin [97, 98]. However, the neutrino

radiation from a high-redshift SMS collapse will be difficult to detect for redshift $z \gtrsim 0.2$, though below this redshift the SMS collapse time template may allow IceCube to extract this signal [98].

Detection of the gravitational-wave ringdown signal associated with the black hole produced in SMS collapse might be another way to tag the linear memory GWM signal as having a SMS collapse origin. In fact, the ringdown signal should follow neutrino burst-driven GWM by no more than one dynamical timescale, $\sim M_5^{\rm HC}$ s. However, a slowly rotating or a non-rotating SMS might not generate a gravitational-wave ringdown signal of high enough amplitude to be detected by the existing or proposed laser interferometers, especially if the SMS is at high redshift.

A non-detection of the gravitational-wave ringdown signal will force us to examine other possible sources, for example, conventional core collapse supernovae and hyperbolic binaries occurring in the local galactic group. A typical core collapse event radiates roughly $\sim 10^{53}$ erg in neutrinos in a few neutrino diffusion timescales, $\lesssim 10$ s. A supernova event occurring in the Andromeda galaxy, approximately 1 Mpc away from earth, could produce a neutrino burst-generated GWM signal with strain $\sim 10^{-23}$ on a timescale ~ 1 s to 10 s, similar to the characteristics of neutrino-burst generated GWM from high-redshift SMS collapse.

Fortunately, several other counterpart signals would be expected to accompany the supernovae GWM signal, for example, the strong gravitational-wave burst without memory from the motion of the baryonic component in the source, the electromagnetic (EM) radiation, and the burst of neutrinos. The latter may be problematic to detect if the source is at an appreciable distance outside the Galaxy. The detection of any of these counterparts could help to distinguish a GWM signal from local group core collapse supernova events and the GWM signal from a high-redshift SMS collapse. EM transients associated with conventional compact object sources should be detectable in most circumstances where their linear memory signals might be confused with those discussed here. Indeed, it is interesting to speculate on whether the EM signal from SMS collapse or explosion at high redshift might be detectable – the future prospects for such a detection are encouraging given the revolution occurring in time domain/transient astronomy

across the EM spectrum.

There can be other compact object sources of linear memory GWM signals. Among these are hyperbolic binaries, i.e., two stars in an unbound orbit, in essence "bremss-ing" off gravitational radiation. Two stars undergoing a close, but unbound encounter, can radiate GWM signals with strain magnitude $4\,m_{\rm A}\,m_{\rm B}/(b\,r)$ on the characteristic timescale b/v [72]. Here $m_{\rm A}$ and $m_{\rm B}$ are the masses of the two objects, b is the impact parameter, r is the distance from the observer to the hyperbolic binary source, and v is the relative velocity between the two objects at closest approach. Consider two neutron stars in the Andromeda galaxy (assumed 1 Mpc distant from earth for this example) flying past to each other with a relative speed $\sim 1000\,{\rm km\,s^{-1}}$ and an impact parameter $\sim 10^4\,{\rm km}$. The gravitational wave strain from this event would be $\sim 6\times10^{-23}$, and the timescale over which the amplitude of this gravitational radiation is appreciable is ~ 10 s. We would expect no significant EM or neutrino signatures from such an event.

However, the polarization of the expected gravitational radiation from a hyperbolic encounter will be different from the polarization in SMS neutrino burst-generated GWM. As shown in Ref. [72], the gravitational wave generated in the hyperbolic binary encounter have both linear and circular polarization, whereas the neutrino burst-generated GWM discussed in this work would have only linear polarization. A detection of a circularly polarized component of the GWM generally would indicate that the signal was not produced in the SMS scenario discussed here. But there is a loophole. Note that at some detector inclinations relative to the orbital plane of the hyperbolic binary, the observer would receive only the linearly polarized GWM component and not the circularly polarized one (see Fig. 2 in Ref. [72]). In that case, we would not be able to distinguish between the GWM signal coming from a hyperbolic binary and the GWM signal coming from high-redshift SMS collapse.

2.6 Conclusion

In this paper we point out an intriguing connection between neutrino burst-generated gravitational waves from the collapse of high entropy, fully convective SMSs at high redshift and the capabilities of proposed space-based gravitational wave observatories like BBO and DECIGO to detect linear memory gravitational wave signals with high sensitivity. We have made simple estimates of the expected linear memory gravitational waves (GWM) likely to be produced by SMS collapse-generated neutrino bursts and the response of these detectors to these signals. We conclude that detection of these GWM is possible in some cases and for some DECIGO detector configurations, even from SMS collapse at high redshift. Detections along these lines would open a new window on an old, but otherwise mysterious issue in relativistic astrophysics: the origin of supermassive black holes.

In the scenarios we examined, gravitational collapse of high entropy SMSs engineers prodigious neutrino production which, in turn, gives rise to a relatively unique gravitational wave signal, the GWM. The high entropy attendant to a hydrostatic SMS implies that these objects possess copious electron/positron pairs in electromagnetic equilibrium. This, coupled with the strong temperature dependence ($\propto T^9$) of $e^{\pm}$-pair annihilation into escaping neutrino pairs of all flavors, guarantees that SMS collapse constitutes an prodigious engine for neutrino production.

In fact, SMSs with homologous core masses in the range $5 \times 10^4\, M_\odot$ to $5 \times 10^5\, M_\odot$ will radiate an optimal fraction of their rest mass in a burst of neutrinos, mostly produced close to the black hole formation point because of the T^9 neutrino emissivity dependence. Neutrinos from lower mass stars will likely suffer scattering-induced trapping, cutting down the amplitudes and decreasing the frequency of gravitational waves produced, while higher mass SMSs do not get hot enough to radiate a significant fraction of their mass in neutrinos before black hole formation. The collapse of a $10^5\, M_\odot$ SMS is likely accompanied by a few percent of its gravitational binding energy being radiated as neutrinos, on a timescale $\sim$ 1 s to 10 s. An asymmetry in the outgoing neutrino energy flux can create a characteristic GWM signal, observable in the frequency bands

where DECIGO and BBO are most sensitive.

For example, a modest rotation of the SMS could result in a small temperature and neutrino emission asymmetry. In an otherwise static and neutrino-transparent SMS, this would not produce an appreciable quadrupole moment in the neutrino field. However, in a non-static, collapsing SMS, the neutrino direction symmetry is broken, and a differential blueshift-redshift effect, much like the integrated Sachs-Wolfe (ISW) effect for photons propagating through evolving density fluctuations/potential wells in the early universe, serves to imprint any temperature asymmetry or inhomogeneity on the outgoing neutrino energy flux – this can give a time-changing quadruple moment in the neutrino mass-energy field and, hence, gravitational radiation. Using Shi & Fuller's result for neutrino energy luminosity, the neutrino burst-generated GWM signal produced from the collapse of an $M^{\rm HC} = 5 \times 10^4 M_\odot$ SMS could be observed with SNR > 5 for DECIGO out to redshift 7 and for Ultimate DECIGO out to redshifts of order ~ 100. Using Linke et al.'s result for the neutrino energy luminosity, they would be observable with out to redshift $z \sim 13$ with SNR > 5 in the Ultimate DECIGO configuration. The unique characteristics of the DECIGO detector response to a linear memory gravitational wave should allow this detector to tag this signal as a GWM.

There are many pitfalls and unresolved issues in our estimates. We have discussed several of these, including the effects of nuclear burning and the phasing of this energy input with hydrostatic SMS evolution, collapse, and neutrino emission. Near BH formation, the collapse timescale - over which most of the neutrinos are emitted - may be significantly larger than the free-fall timescale we have employed in our calculations. This could shift the timescale of the GWM longer and out of the most sensitive frequency range of the detectors like BBO/DECIGO.

Hydrodynamic evolution itself could be impacted by the competing processes of nuclear burning and neutrino energy loss. For example, radiation pressure will resist the infall of the homologous core, resulting in a collapse timescale larger than the free-fall timescale. On the other hand, a more extended collapse time will increase the integrated neutrino emission, and therefore increase the GWM strain. The coupled nuclear, weak interaction, rotation, and hydrodynamic

evolution of SMS stars remains a fascinating, if complicated story. How these issues play out in detail could affect the GWM estimates we make here. Obviously, a key conclusion of our work here is that more sophisticated calculations including these and other effects are warranted.

It remains an open question whether high entropy, fully convective SMSs form at high redshifts, and if they do form, whether the BHs they produce are the seeds for the formation of high redshift SMBHs. For the purposes of this study, we are agnostic on these issues. However, the detection of GWM signals attributable to the neutrino burst from these high redshift SMSs may provide an intriguing hint toward solving, or narrowing, the problem of the formation of SMBHs in the high redshift universe. It is remarkable that the envisioned space-based gravitational wave observatories like BBO/DECIGO could be poised to probe this physics in a nearly unique way.

2.7 Acknowledgments

We thank Chris Fryer, Lee Lindblom, Wei-Tou Ni, S. Tawa, and Massimo Tinto for valuable discussions. This work was supported in part by National Science Foundation Grants No. PHY-1307372 and No. PHY-1614864. We also would like to acknowledge a grant from University of California Office of the President.

This chapter is, in part, a reprint of material from published work done in collaboration with George M. Fuller and Chad T. Kishimito, as it appears in the Physical Review D 98 (2), 023002. The dissertation author was the primary investigator and author of this material.

2.A Quadrupole moment approximation

Epstein [75] has given a rigorous derivation of gravitational radiation generated from a neutrino burst via direct integration of the *linearized* inhomogeneous Einstein field equations. In the following, we derive this result in the weak-field quadrupole moment approximation.

We can break up the neutrino burst into N components and label them by index $\alpha = 1, 2,$

3, ..., N. The mass-energy density distribution can be written in the point-mass description:

$$\rho_\nu\left(t_r,\mathbf{x}'\right)=\sum_\alpha \frac{M_\alpha}{\sqrt{1-v_\alpha^2}}\,\delta\left(\mathbf{x}'-\mathbf{r}_\alpha\right), \tag{2.8}$$

where M_α, v_α and $\mathbf{r}_\alpha$ are the rest mass, velocity and position of the αth neutrino.

Assuming constant neutrino velocity, the second time-derivative of the mass quadrupole moment tensor becomes

$$\begin{aligned}\ddot{I}^{jk}\left(t_r\right)&=2\sum_\alpha \frac{M_\alpha}{\sqrt{1-v_\alpha^2}}\,v_\alpha{}^j\,v_\alpha{}^k\\&=2\int \rho_\nu\left(t_r,x'\right)\,\frac{n^j n^k}{1-\vec{\mathbf{N}}\cdot\hat{\mathbf{n}}}\,d^3x'\end{aligned} \tag{2.9}$$

where $\vec{\mathbf{N}}$ is the unit vector between the source and the detector and $\hat{\mathbf{n}}$ is the unit vector of the neutrino flux directed into the solid angle $d\Omega'$. The second step of Eq. (2.9) assumes neutrinos travel at the speed of light and we interpret the $M_\alpha/\sqrt{1-v_\alpha^2}$ to be the αth neutrino's energy measured in the detector's rest frame. The $(1-\vec{\mathbf{N}}\cdot\hat{\mathbf{n}})^{-1}$ term comes from the Lienard–Wiechert solution. Now apply the gravitational wave quadrupole formula and obtain

$$\Delta h_{\mathrm{TT}}^{jk}\left(t,\mathbf{x}\right)=\frac{4}{d}\int_{-\infty}^{t-d}\int \frac{d^2E_\nu}{dt'd\Omega'}\left[\frac{n^j n^k}{1-\vec{\mathbf{N}}\cdot\hat{\mathbf{n}}}\right]^{\mathrm{TT}} d\Omega'\,dt'. \tag{2.10}$$

Here d is the distance from the source to detector; $d\Omega'$ is the solid angle enclosing the source; E_ν is the total energy emitted as neutrinos. Evaluating Eq. (2.10) yields gravitational waves with linear memory (GWM) from a burst of neutrinos: gravitational wave strain $h_{\mathrm{TT}}^{jk}=0$ before the GWM arrives and accumulates to a nonzero value $\Delta h_{\mathrm{TT}}^{jk}$ after the gravitational wave passes the detectors.

If the emission has spherical symmetry, then there is no gravitational signature – this is Birkhoff's theorem; but if there is a small anisotropy in the neutrino emission $dE_\nu/d\Omega'$, then the integral in Eq. (2.10) is nonzero and therefore the memory strain accumulates to a nonzero value.

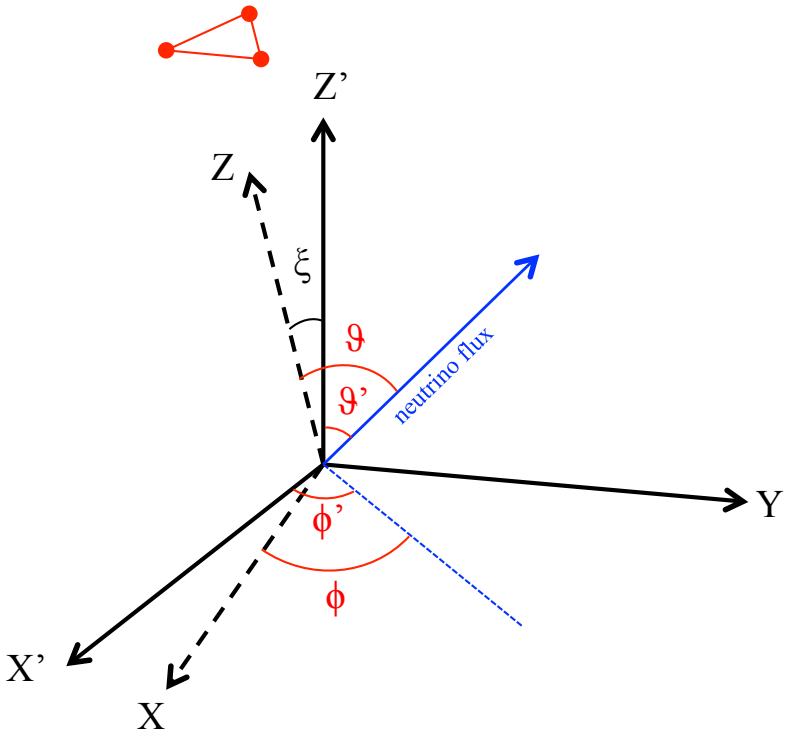

Figure 2.5. xyz and $x'y'z'$ are coordinate systems of the detector and the source, respectively. The source is located at the origin and the detector is far out in the $\hat{z}$ direction. We choose the neutrino emission distribution to be axisymmetric about the z' axis. The $x-z$ and $x'-z'$ planes are coplanar and differ by a rotation by angle ξ about the y axis.

The function $d^2E_\nu/d\Omega' dt'$ in Eq. (2.10) can be written as $L_\nu(t')\,F(t',\Omega')$, where $L_\nu(t')$ is the neutrino luminosity and $F(t',\Omega')$ is the emission angular distribution with $\int F(t',\Omega')\,d\Omega' = 1$.

Placing the detector at the transverse direction of the gravitational wave, say along the z axis in Fig. 2.5, the two polarizations are $h_+^{\rm TT} \equiv h_{xx}^{\rm TT} = -h_{yy}^{\rm TT}$ and $h_\times \equiv h_{xy}^{\rm TT} = h_{yx}^{\rm TT}$. Eq. (2.10) can be written as

$$\Delta h_+^{\rm TT} + i\Delta h_\times^{\rm TT} = \frac{2}{d}\int_{-\infty}^{t-d} L_\nu(t')\,dt' \int F(t',\Omega')\,(1+\cos\theta)\,e^{i2\phi}\,d\Omega', \tag{2.11}$$

where θ is the angle between the flux going into $d\Omega'$ and the direction to the detector, and ϕ is the azimuthal angle with respect to the x axis in the xy plane. From Eq. (2.11) it's clear that the rise time for the non-oscillatory gravitational wave memory signal to reach its final strain is the same as the duration of the neutrino burst in the detector's rest frame.

2.B Detector's response to a GWM signal

The GWM is a non-oscillatory signal which causes a permanent displacement of the detector's arm length after this wave train has passed. Its effect on two freely falling masses is a "DC" offset-like signal, with the rise time equal to the signal burst time Δt_m. As an example, we can estimate the strain as a function of detector frame time based on the total neutrino emission and burst time taken from the Shi & Fuller neutrino luminosity and timescale result. This estimate results in the solid curve in Fig. 2.6. It shows the full GWM waveform for $M^{\rm HC} = 10^5\, M_\odot$ SMS collapse at $z = 7$.

Laser interferometry gravitational wave detectors' sensitivity curves are frequency dependent, so only a narrow frequency band is "audible" to such detectors. To mimic DECIGO's response to the GWM signal, we use a bandpass filter in the frequency band $[0.01, 1]$ Hz. The green dashed curve in Fig. 2.6 represents the response of DECIGO to the GWM signal (the solid curve). The waveform after the filtering will not resemble a "DC"-like signal because of the suppression of low frequencies.

2.C Neutrino absorption by BH trapped surface

Local neutrino emissivity ($\propto T^9$) and overall neutrino luminosity both increase as the core collapses and the temperature increases. Peak neutrino luminosity will occur very near where a trapped surface forms and gravitational redshift rather abruptly cuts off neutrino radiation to infinity. Just what that peak luminosity is and, concomitantly, the amplitude of the GWM signal both depend on details of relativistic effects near black hole formation. With our nearly Newtonian treatment, we can make only cogent, order of magnitude estimates, of these effects. The essence of the problem: The competition between increasing neutrino emissivity and gravitational redshift implies that most of the neutrinos are emitted at a thin spherical shell of radius somewhere between $1\,M^{\rm HC}$ and $2\,M^{\rm HC}$ within the dynamical time scale $2\,M^{\rm HC}$. The neutrino luminosity calculation from the Shi & Fuller result is based on the assumption that

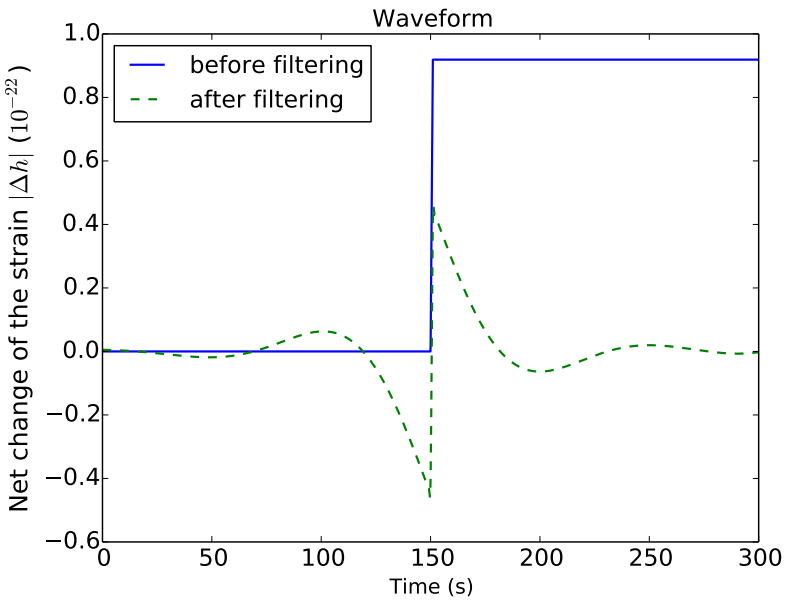

Figure 2.6. Estimated gravitational wave time series from a SMS collapse with $M^{\rm HC} = 10^5 M_\odot$ at $z = 7$ and the neutrino emission asymmetry $\alpha = -0.02$. The detector is placed at equatorial plane $\xi = \pi/2$. The blue solid line shows the detector's arm response to GWM signal. The green dashed line shows the time series filtered with a $10^{-2} - 10^0$ Hz bandpass filter to illustrate the signal seen by DECIGO.

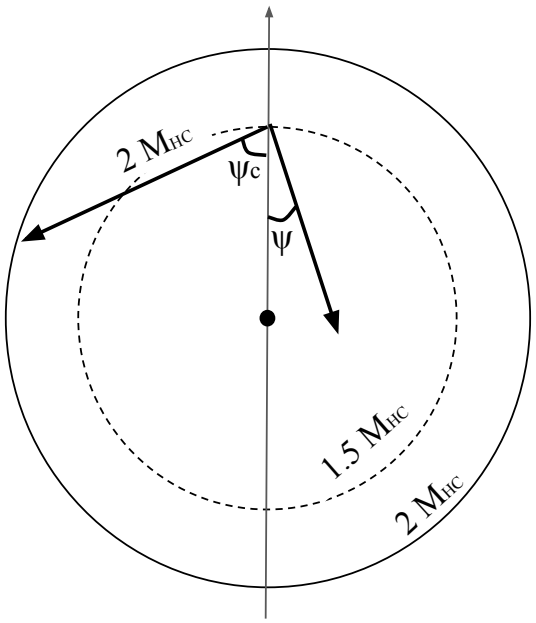

Figure 2.7. Illustration of neutrino absorption by BH trapped surface formation. The solid circle is the trapped surface after the BH is formed. The dashed circle is the radius of neutrino peak production site. Neutrinos moving toward the core at the angle $\psi < \psi_c$ will be trapped in the BH and therefore make no contribution to the neutrino emission asymmetry α.

neutrinos only move radially outward. Yet a significant fraction of neutrinos that move radially inward will not have enough time to pass through the Schwarzschild radius $2M^{\rm HC}$ at the onset of BH formation. The consequences are: (1) the actual neutrino luminosity is smaller than what is calculated in Shi & Fuller and (2) only the neutrinos that are not trapped in the BH can contribute the neutrino emission asymmetry via the ISW-like effect.

Assume that peak neutrino emission happens in a thin spherical shell with the radius $r_{\rm peak} \approx 1.5M^{\rm HC}$ within one dynamical time before the BH formation. Neutrinos emitted into an inwardly-directed pencil of directions with launch angle ψ (relative to radially inward-directed unit vector) smaller than the critical angle ψ_c have a time of flight greater than $2M^{\rm HC}$ and therefore will be inside the trapped surface when the BH is formed. The critical angle can be estimated easily in Euclidean geometry: $\psi_c \approx 68^\circ$ (see Fig. 2.7). As a result, the fraction of

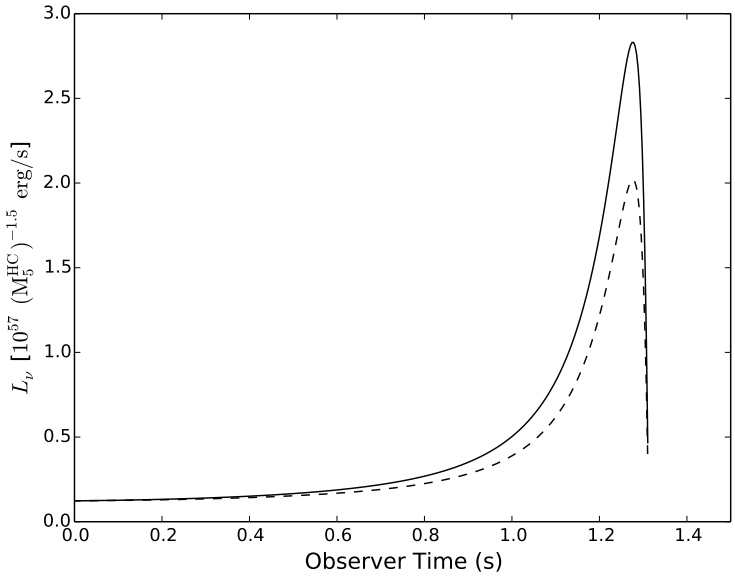

Figure 2.8. Time evolution of the neutrino luminosity. The solid curve is taken from Shi & Fuller, which assumes that neutrinos only move radially outward. The dashed curve takes account the neutrino luminosity loss due to the different time of flight at different emission angles.

neutrino luminosity loss, ε, is approximately

$$\varepsilon = \frac{1}{4\pi}\int_0^{2\pi}\int_0^{\psi_c} \sin\theta d\theta d\phi \approx 0.3 \tag{2.12}$$

Fig. 2.8 shows the time evolution of neutrino luminosity for an observer at infinity. The solid curve is taken from the Shi & Fuller result, which assumes all neutrinos move radially outward. The dashed curve is the neutrino luminosity after taking account of the energy loss ε stemming from different time of flight along trajectories at different emission angles.

Here we show a crude estimate simply to illustrate how the BH trapped surface could change the neutrino luminosity. Certainly, more sophisticated, fully relativistic 3-dimensional hydrodynamical simulations together with a numerical spacetime/gravitational wave calculation are warranted. Nevertheless, throughout this paper, to facilitate a parameter survey and to illustrate the basic effects we adopt the neutrino luminosity functions taken from the Shi & Fuller and Linke et al. results.

Neutrino trapping by trapped surface formation also impacts estimates of the neutrino emission asymmetry. Neutrino born on trajectories with angle ψ less than the critical angle ψ_c will be trapped in the BH. These will not make any contribution to the neutrino emission asymmetry α. Neutrinos moving on trajectories with angles $\psi > \pi/2$ will not experience any ISW-like effect because they do not stream into the collapsing core. Only neutrinos moving on trajectory angles between ψ_c and $\pi/2$ can experience the differential blueshift-redshift effect and still escape to contribute to the neutrino emission asymmetry.

Using the Newtonian picture, a neutrino directed toward the collapsing core of the SMS will lose a fraction of its energy, $\delta E/E \sim \delta M/r$, from the ISW-like, angle-dependent, differential redshift-blueshift effect. The timescale necessary for the neutrino to stream through the core and back to its initial radius is $\delta t = 2r\cos\psi$, where ψ is the angle between the neutrino trajectory and the radial line. The increase in the enclosed mass is $\delta M \sim \bar{\rho} \times (4\pi r^2) \times (2r\cos\psi)$, where $\bar{\rho}$ is the average density of the homologous core close to the BH formation. The fractional energy loss is $\delta E/E \sim (r/r_s)\cos\psi$.

Most of the neutrinos are emitted in a relatively thin spherical shell of radius somewhere at $r_{\rm peak} \approx 1.5M^{\rm HC}$. Consequently, in this paper, we approximate the fractional energy loss in a radius-independent form $\delta E/E \sim \frac{3}{4} \times \cos\psi$. Note that this function is only meant to represent the energy loss due to the ISW-like effect. It does not include the absorption accompanying trapped surface formation.

As a simple model, let the neutrino emissivity in the peak emission shell be parameterized by $Q_\eta(\theta) = Q_0\left(1+\eta\cos^2\theta\right)$, where η is the neutrino emissivity asymmetry between volume elements along the polar direction and the equatorial plane and Q_0 is proportional to the volume-averaged emissivity, $\langle Q_\eta \rangle = Q_0(1+\eta/3)$. To estimate the polar-equatorial neutrino energy flux anisotropy, we need to estimate the neutrino energy fluxes that experience the differential blueshift-redshift effect and stream into a solid angle $d\Omega$ in the polar direction, along the negative

z-axis ($\phi^{(\mathrm{pol})}$), and an equatorial direction, along the negative y-axis ($\phi^{(\mathrm{eq})}$):

$$\phi^{(\mathrm{pol})} = \int_0^{2\pi} \int_{\psi_c}^{\pi/2} \left(1 - \frac{3}{4}\cos\theta\right) Q_\eta(\theta) \sin\theta \, d\theta \, d\phi, \tag{2.13}$$

$$\phi^{(eq)} = \int_0^{2\pi} \int_{\psi_c}^{\pi/2} \left(1 - \frac{3}{4}\cos\theta'\right) Q_\eta(\theta) \sin\theta' \, d\theta' \, d\phi', \tag{2.14}$$

where θ is the polar angle from z-direction and θ' is the new polar angle measured from y-direction. Here we take ψ_c to be 68°. Parameterizing the polar-equatorial neutrino energy flux asymmetry, α, as the ratio of the total flux in the polar direction to the flux in the equatorial directions subtracted by unity, and using $\eta = 0.25$, we estimate a neutrino emission asymmetry:

$$\alpha = \frac{2\pi\langle Q_\eta \rangle + \phi^{(\mathrm{pol})}}{2\pi\langle Q_\eta \rangle + \phi^{(\mathrm{eq})}} - 1 \approx -0.02. \tag{2.15}$$

The emission asymmetry parameter α will depend on the SMS initial rotation speed. A faster rotation will induce a larger emissivity asymmetry, leading to a larger neutrino emission asymmetry. But given that the initial state of the SMS is unknown, α should be treated as a free parameter. Nevertheless, for illustrative purposes we will use $\alpha = -0.02$ throughout this paper.

2.D An electromagnetic analogue for linear wave memory

In this appendix, we demonstrate a similar wave memory effect from the classical electrodynamics. We start with comparing the wave equations in General Relativity and classical electrodynamics. The linearized Einstein equation in a Lorentz gauge, $\bar{h}^{\mu\nu}{}_{,\nu} = 0$, is given as

$$\Box \bar{h}^{\mu\nu} = -\frac{16\pi G}{c^4} T^{\mu\nu}, \tag{2.16}$$

where $\bar{h}^{\mu\nu} \equiv h^{\mu\nu} - \frac{1}{2}\eta^{\mu\nu} h^{\alpha}{}_{\alpha}$ is the trace reverse of $h^{\mu\nu}$, $\Box \equiv -\partial^2/\partial t^2 + \nabla^2$ is D'Alembertian operator, and $T^{\mu\nu}$ is stress-energy tensor. The inhomogeneous electromagnetic wave equation in

Gaussian units and the Lorentz gauge, $A^{\mu}{}_{,\mu}$, is given as

$$\Box A^{\mu} = -4\pi J^{\mu}, \tag{2.17}$$

where $A^{\mu} = (\phi, \mathbf{A})$ is electromagnetic four-potential and $J^{\mu} = (\rho, \mathbf{J})$ is four-current. Comparing Eqs. (2.16) and (2.17), we see that A^{μ} is analogous to $h^{\mu\nu}$ and J^{μ} is analogous to $T^{\mu\nu}$.

From our analysis in the main body of the text of Chapter 2, we learn that a gravitationally unbounded source can generate a permanent strain h and, consequently, a permanent change of the proper length between two free-falling masses. The change of proper length can be observed via the interference of two groups of photons acquiring different phases. Based on a comparison between Eqs. (2.16) and (2.17), we also expect that an unbounded electric charge current density $\mathbf{J}$ can produce a permanent non-zero vector potential $\mathbf{A}$ – it is a memory of vector potential "imprinted" in space. In principle, this permanent $\mathbf{A}$ can be observed via the interference of two charged particles acquiring two different phases as they propagate along different paths in space.

The solutions for Eq. (2.17) are given as

$$\begin{aligned} \phi(t,\mathbf{r}) &= \int d^3x' \frac{1}{|\mathbf{r}-\mathbf{r}'|}\left[\rho\left(t',\mathbf{r}'\right)\right]_{\text{ret}}, \\ \mathbf{A}(t,\mathbf{r}) &= \int d^3x' \frac{1}{c|\mathbf{r}-\mathbf{r}'|}\left[\mathbf{J}\left(t',\mathbf{r}'\right)\right]_{\text{ret}}, \end{aligned} \tag{2.18}$$

where t' is the retarded time which is defined as $t' \equiv t - |\mathbf{r}-\mathbf{r}'|/c$, $\mathbf{r}$ is the location of the observer, and $\mathbf{r}'$ is the charge distribution. The electric and magnetic fields are given as

$$\begin{aligned} \mathbf{E}(t,\mathbf{r}) = &\underbrace{\int d^3x' \frac{\hat{\mathbf{R}}}{|\mathbf{r}-\mathbf{r}'|^2}\rho\left(t',\mathbf{R}'\right)_{\text{ret}}}_{\mathbf{E}_1} \\ &+ \underbrace{\int d^3x' \frac{\hat{\mathbf{R}}}{c|\mathbf{r}-\mathbf{r}'|}\left[\frac{\partial\rho(t',\mathbf{r}')}{\partial t'}\right]_{\text{ret}}}_{\mathbf{E}_2} + \underbrace{\int d^3x' \frac{-1}{c^2|\mathbf{r}-\mathbf{r}'|}\left[\frac{\partial\mathbf{J}(t',\mathbf{r}')}{\partial t'}\right]_{\text{ret}}}_{\mathbf{E}_3}, \end{aligned} \tag{2.19}$$

and

$$\mathbf{B}(t,\mathbf{x}) = \underbrace{\int d^3x' \frac{-\hat{\mathbf{R}}}{c|\mathbf{r}-\mathbf{r}'|^2} \times \mathbf{J}\left(t',\mathbf{r}'\right)}_{\mathbf{B}_1} + \underbrace{\int d^3x' \frac{-\hat{\mathbf{R}}}{c^2|\mathbf{r}-\mathbf{r}'|} \times \left[\frac{\partial \mathbf{J}(t',\mathbf{r}')}{\partial t'}\right]_{\text{ret}}}_{\mathbf{B}_2}, \tag{2.20}$$

where we define the unit separation vector $\hat{\mathbf{R}} = (\mathbf{r}-\mathbf{r}')/|\mathbf{r}-\mathbf{r}'|$.

We consider a charge emitter located at the origin and emitting charged particles moving at a speed of light. Now, let this emitter emit a positively charged current, I, in the $+z$ direction and a negative current, $-I$, in the $-z$ direction. We further assume that the magnitude of the positive current and the negative current are the same so that the net change of charge density is zero, i.e., $\partial\rho/\partial t' = 0$. We like to know the $\mathbf{E}$ and $\mathbf{B}$ fields radiated from the source during the initial stage of current emission, at which time the size of the charge distribution, $\mathbf{r}' \sim ct'$, is still much smaller than the distance between the source and the observer. Under these conditions, we find:

1. $\mathbf{E}_1$ is the electrostatic field, which goes as $1/r^2$,
2. $\mathbf{E}_2$ is zero since $\partial\rho/\partial t' = 0$,
3. $\mathbf{B}_1$ is the magnetostatic field, which goes as $1/r^2$,
4. The combination of $\mathbf{E}_3$ and $\mathbf{B}_2$ forms an electromagnetic radiation generated by the time-changing charge currents. Furthermore, $\mathbf{E}_3 \gg \mathbf{E}_1$ and $\mathbf{B}_2 \gg \mathbf{B}_1$ when the observer is far from the source.

As a result, the leading order contribution of $\mathbf{E}(t,\mathbf{r})$ comes from $\mathbf{E}_3$. Performing the volume integration, we can write $\mathbf{E}(t,\mathbf{r})$ as

$$\mathbf{E}(t,\mathbf{r}) = -\frac{2\hat{\mathbf{z}}}{rc}\frac{dQ_+(t')}{dt'}, \tag{2.21}$$

where $Q_+(t')$ is the total amount of positive charges emitted out from the source at the retarded

time t'.

Suppose the charge emitter emits a total amounts of positive charge $Q_{+,\text{tot}}$ and negative charge $-Q_{+,\text{tot}}$ during $0 \leq t' \leq \Delta t'$. An EM pulse with the width $c\Delta t'$ is then radiated out from the origin. In the region that has been swept by this EM pulse, the change of the vector potential, $\Delta\mathbf{A}$, is given as

$$\Delta\mathbf{A}\left(t,\mathbf{r}\right) = -\int_0^{\Delta t'} c\mathbf{E}\left(t',\mathbf{r}\right) dt' = \frac{2Q_{+,\text{tot}}}{r}\,\hat{\mathbf{z}}. \tag{2.22}$$

From Eq. (2.22), we see that $\Delta\mathbf{A}$ reaches a constant value after the EM pulse has fully passed by point $\mathbf{r}$, and the total change of $\mathbf{A}$ is proportional to the total charges emitted from the emitter. The constant $\mathbf{A}$ is the "memory" imprinted in the spacetime by the EM pulse. This memory effect happens when the charged particles are ejected out from the source and become unbounded from the system.

2.D.1 Interference

In quantum mechanics, a constant vector potential can change the phase angle of the wavefunction of a charged particle. Two wavefunctions with two different phases could interfere with each other, causing the quantum interference. This effect allows us to observe the increase of the constant vector potential in the spacetime. Here we design a thought experiment to demonstrate how a constant vector potential "imprinted" in the region behind the electromagnetic pulse can be observed by the quantum interference experiment.

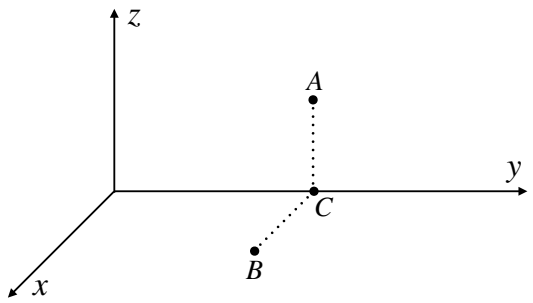

Figure 2.9. Let two charged particles start at point C and set their phases to be the same. Move one particle to point A and the other to point B, and bring them back to point C after the EM pulse passes by point C.

We consider a wavefunction $\phi(x)$ of a charged particle that undergoes a U(1) gauge transformation, $\phi(x) \to e^{i\Lambda(x)}\phi(x)$, where $\Lambda(x)$ follows $A_\mu(x) \to A_\mu(x) + \frac{1}{e}\partial_\mu\Lambda(x)$.

1. First, we consider a EM pulse moving along $+y$ axis, as shown in Fig. 2.9. Let the cross-section of the pulse on the xz plane be small enough so that, far from the y-axis, the **E** and **B** can be neglected.

2. Before the EM pulse arrives point C, we prepare two identical particles at point C and let two particles have equal phases.

3. Bring the first particle along $\hat{\mathbf{z}}$-direction to point A and the second particle along $\hat{\mathbf{x}}$-direction to point B.

4. After the EM pulse has passed by point C, the two particles still have equal phases as there is no EM pulse passing through point A or B.

5. Bring both particles back to point C. Since the second particle moves in the direction perpendicular to **A**, the second particle does not gain any additional phase. On the other hand, the first particle moves in the direction (anti-)parallel to **A** and acquires an additional phase $-e\int \Delta\mathbf{A}\cdot dz\hat{\mathbf{z}}$ as it moves from point A to point C. When the two particles meet at point C again, they have different phases. The difference of the two phases can be observed through the quantum interference experiment.

From this experiment, we see that the electromagnetically unbound charge currents emit a unique EM pulse that imprints a constant, permanent vector potential, or memory of EM field, on the spacetime and changes the quantum phase of the particles. This phenomenon is very similar to the linear gravitational wave memory effect, in which case the gravitationally unbound matter emits a particular gravitational wave that imprints a constant change of metric on the spacetime.

Chapter 3

Probing dark photons in the early universe with big bang nucleosynthesis

We perform calculations of dark photon production and decay in the early universe for ranges of dark photon masses and vacuum coupling with standard model photons. Simultaneously and self-consistently with dark photon production and decay, our calculations include a complete treatment of weak decoupling and big bang nucleosynthesis (BBN) physics. These calculations incorporate all relevant weak, electromagnetic, and strong nuclear reactions, including charge-changing (isospin-changing) lepton capture and decay processes. They reveal a rich interplay of dark photon production, decay, and associated out-of-equilibrium transport of entropy into the decoupling neutrino seas. Most importantly, the self-consistent nature of our simulations allows us to capture the magnitude and phasing of entropy injection and dilution. Entropy injection-induced alteration of the time-temperature-scale factor relation during weak decoupling and BBN leads to changes in the light element abundance yields and the total radiation content (as parametrized by $N_{\rm eff}$). These changes suggest ways to extend previous dark photon BBN constraints. However, our calculations also identify ranges of dark photon mass and couplings not yet constrained, but perhaps accessible and probable, in future Stage-4 cosmic microwave background experiments and future high precision primordial deuterium abundance measurements.

3.1 Introduction

The early universe and the increasingly sophisticated observations that constrain its history together comprise a promising "laboratory" for dark sector physics. Vetting new physics with this laboratory demands accurate modeling of the effects of this physics on the evolution of key parameters in the early universe and the impact of those effects on observables. In this paper we examine in a self-consistent way how dark photons in a specific range of masses and couplings with the standard model affect neutrino decoupling, associated relic energy density, and light element abundances.

Weak interaction decoupling and big bang nucleosynthesis (BBN) in the early universe are protracted and intertwined processes. Together they proceed over many Hubble times, roughly spanning temperature regimes from $T \sim 10\,\mathrm{MeV}$ to $T \sim 10\,\mathrm{keV}$. In strictly standard model cosmology, neutrino charged- and neutral-current scattering on electrons and positrons continues to facilitate energy and entropy transfer to the plasma of electrons, positrons, photons, and nucleons even down to temperatures near alpha particle formation ($T \sim 100\,\mathrm{keV}$), although the effectiveness of this transfer decreases significantly with falling temperature. Likewise, charged current weak processes involving neutrinos and charged leptons continue alteration of the neutron-to-proton (n/p) ratio throughout this epoch [99].

If there are out-of-equilibrium Beyond Standard Model (BSM) particles decaying and injecting energy and entropy into the plasma during the weak decoupling epoch, then there will be an extra (over and above the standard model) entropy flow between the neutrino and plasma sectors. This effect not only alters the n/p ratio from standard model cosmology, but also changes the phasing of these quantities in time relative to the dynamics of nuclear reactions involving light elements. In broad brush, these nuclear reactions proceed in the context of a freeze-out from nuclear statistical equilibrium (NSE). In addition, entropy generation from out-of-equilibrium particle decay in such BSM scenarios will dilute the neutrino radiation density and decrease the relativistic degrees of freedom (parameterized by N_{eff}). In principle, these alterations from

standard cosmology can be calculated with a self-consistent treatment of neutrino energy spectra, plasma temperature, and the strong, electromagnetic, and weak nuclear reactions. A comparison of $N_{\rm eff}$ and light element abundances (principally deuterium and helium) emerging from this epoch with observationally-inferred values of these allows us to explore BSM physics and in some cases to make constraints on the model parameters of this new physics. This program is all the more alluring given anticipated high precision Stage-4 cosmic microwave background (CMB) experiments [100] ($N_{\rm eff}$ and primordial ^{4}He) and the advent of 30-m class telescopes [101, 102] (deuterium, hereafter D). The possibility of increased precision in these measurements holds out the promise of better probes of BSM and dark sector physics.

While there are several portals to dark sector physics, we choose to concentrate here on the kinetic mixing portal of a dark photon [103, 104]. This portal is tractable and relatively simple, yet possesses a potentially rich phenomenology of outcomes. Exploration of this portal has gained popularity in recent years. In part, this is because a dark photon could be a dark mediator between a dark sector and SM particles [105, 106]. This physics may also explain the muon $g-2$ anomaly [107]. Moreover, standard model photons manifest as collective modes (e.g., plasmons) in medium. These collective plasma effects can enable resonant (e.g., enhanced) dark photon-photon inter-conversion. In turn, this could produce unique and fruitful dark sector signatures in various plasma environments ranging from compact objects to the early universe [48, 108–121].

For our purposes the dark photon will be a new $U(1)'$ vector particle that has a kinetic mixing with the SM photon [103, 104]. Below the electroweak energy scale the relevant low-energy vacuum Lagrangian we adopt for the dark and standard model electromagnetic sectors is

$$\mathscr{L} \supset -\frac{1}{4}F_{\mu\nu}F^{\mu\nu} - \frac{1}{4}F'_{\mu\nu}F'^{\mu\nu} + \frac{\kappa}{2}F_{\mu\nu}F'^{\mu\nu} + \frac{1}{2}{m_{A'}}^2 A'_\mu A'^\mu, \tag{3.1}$$

where here, and hereafter, vector potential A_μ and field tensor $F^{\mu\nu}$ will refer to the SM photon and electromagnetic fields, while the primed versions, A'_μ and $F'^{\mu\nu}$, will refer to the corresponding

dark photon field. Here κ is the vacuum kinetic mixing parameter and $m_{A'}$ is the dark photon mass. As for the origin of $m_{A'}$, it could come from a new Higgs mechanism with new light degrees of freedom, or from the Stueckelberg mechanism in which a very heavy dark sector Higgs boson has been integrated out from the theory. In this work, we will consider only the Stueckelberg mechanism alternative.

Previous work investigating the effect of dark photon decay on light element synthesis in the early universe suggested constraints on ranges of dark photon mass and coupling parameter space [122, 123]. Specifically, the authors in Ref. [122] consider the electromagnetic and hadronic energy injection from dark photon decay, the subsequent photo-dissociation of light nuclei, and the creation of a neutron excess. Their abundance-derived bounds are based on the following features of their calculations: (1) D and ^{4}He are under-produced relative to standard model cosmology, a consequence of out-of-NSE ("post-BBN") destruction of nuclei when the dark photon decays to e^+e^-; (2) D and ^{4}He over-production stemming from an increase in the n/p-ratio when the dark photon decays to $\pi^+\pi^-$ or K^+K^- prior to NSE-freezeout, $T > 100\,\mathrm{keV}$; and (3) D over-production from an injection of neutrons facilitated by dark photon decay. Comparing the calculated yields of D, ^{3}He, and ^{4}He with the precision measurements of the D/H ratio from the high-redshift quasar absorption systems [124, 125], they exclude several regions in the model parameter space as shown in figure 3.10.

A more detailed calculation for the fraction of photons induced from dark photon decay capable of photo-dissociating D and ^{4}He has been shown in Ref. [123]. In that paper, the authors show that the amounts of photo-dissociated D and ^{4}He nuclei stemming from dark photon decay are lower than the amounts reported in Ref. [122]. They conclude that demanding that the ^{3}He/D ratio not exceed the observational limits does not lead to a constraint on the dark photon model parameter space.

In addition to the dark photon considerations in Refs. [122, 123], a generic scenario of sub-GeV particles and electromagnetic energy injection from their decays has also been studied, for example in Refs. [126–129]. In particular, Ref. [127] has included a full electromagnetic cascade

(photon and electron) to study the photo-dissociation of the primordial light elements abundances in the post-BBN epoch ($T < 10\,\mathrm{keV}$). This study suggests constraints on late-decaying particles with lifetimes larger than $10^4\,\mathrm{sec}$ (i.e., post-BBN epochs). Expanding on Ref. [127], the authors of Ref. [128] have updated their discussions on electromagnetic injection by taking into account non-universality in the photon cascade spectrum relevant for BBN. Reference [129] similarly incorporates an electromagnetic cascade, but additionally evaluates the effects of a non-standard Hubble rate and baryon-to-photon ratio on the predicted primordial nuclear abundances.

In this work, we follow the general scheme of Refs. [122, 123, 127–129], albeit with a completely self-consistent treatment of nuclear reactions and temperature-time-scale factor phasing and entropy flow between the neutrinos and the photon-electron/positron-baryon plasma, as described above. However, we do not treat the post-BBN epoch ($T < 10\,\mathrm{keV}$), and we consider dark photon masses only between $2\,\mathrm{MeV}$ and $200\,\mathrm{MeV}$. In that range of dark photon rest masses, the dominant decay product is into e^-/e^+-pairs. We are interested in the range of dark photon kinetic mixing in which the dark photons are produced abundantly early on and, at the same time, have a lifetime such that they decay and inject entropy into the plasma at a time which is in the general time frame of weak decoupling and BBN. In this scenario, the entropy-per-baryon during the BBN epoch will start out with a lower value compared to the CMB-determined value measured at a time (e.g., the recombination epoch at $T \approx 0.2\,\mathrm{eV}$) well after the end of BBN. Our calculations are then iterated so that out-of-equilibrium dark photon decay injects the right amount of entropy into the plasma to give the correct CMB-determined value. The upshot is that the plasma in the case of dark photon decay starts out "colder" than in the case of standard cosmology, with entropy added by decay, altering the time-temperature-scale factor relation over that of standard cosmology. This leads to two consequences, both potentially of use in leveraging comparisons with observations into better probes of dark photon mass and coupling.

The first is a consequence of entropy generated from the decay of dark photons depositing energy into the plasma. This phenomenon has an effect in some ways analogous to e^+/e^- "annihilation" in the standard cosmology case. In the standard case, where the entropy in a

comoving volume (or entropy per baryon) is constant, the disappearance of the $e^{\pm}$-pairs in equilibrium means that the entropy they carried is transferred to the photon-electron-baryon plasma, but not to decoupled neutrinos. Hence, eventually the "temperature" of the decoupled neutrino component will be lower than that of the photons. Now consider what happens if additionally, because of out-of-equilibrium particle decay, the co-moving entropy is not constant. Entropy generation from dark photon decay dilutes the radiation energy density (as parametrized by $N_{\rm eff}$) and makes the relic neutrinos even colder relative to the photons than in the case of standard cosmology [130]. Some of the calculations we discuss below also include a complete Boltzmann neutrino transport scheme, similarly self-consistently calculated along with all nuclear reactions and dark photon decay processes [131]. During the protracted weak decoupling and BBN epoch, entropy transfer between the plasma and the decoupling neutrinos is effected by out of equilibrium neutrino scattering on $e^{\pm}$ pairs, even at temperatures well below $T = 1\,\mathrm{MeV}$. This late entropy transfer is a small effect in standard cosmology, but may be larger in non-standard scenarios, such as the one we consider here.

The second consequence of out-of-equilibrium dark photon decay arises from the changes in the history of weak, electromagnetic, and strong nuclear reaction rates that accompany entropy injection and dilution. A beginning (lower) value of the entropy-per-baryon during the BBN epoch means that the plasma starts out with a higher value of the baryon-to-photon ratio, η, compared to the standard cosmology case. As entropy is added by dark photon decay, the time-temperature-scale factor history is altered relative to that in standard cosmology. Entropy is a significant determinant of the abundances of the light elements [132], affecting both the NSE abundance tracks and the course of the nuclear reactions when the system cools to the point where NSE cannot be maintained and individual nuclear reactions become important. Moreover, the alteration in time-temperature-scale factor also affects the history of the neutron-to-proton ratio, n/p. This ratio also influences both NSE and non-equilibrium nuclear reactions. These effects combine to alter light element abundance yields, especially for deuterium and helium, relative to those emerging from a standard cosmology.

The combined effects of dark photon out-of-equilibrium decay may alter each of, for example, $N_{\rm eff}$ and the primordial ^{2}H and ^{4}He yields in a way characteristic of the dark photon mass and vacuum mixing with the standard model sector. This could enable a comparison of our calculations to high precision observations to provide constraints on, or find signatures of, dark photon physics.

In section 3.2 we discuss the physics of dark photon production and decay in the early universe, specialized for the range of masses and standard model couplings as outlined above. Appendices 3.A, 3.B, and 3.C, expand on this physics, with discussions of the polarization tensor, in-medium effects, and dark photon production rates, respectively. In section 3.3, we begin with an exposition of the relevant thermodynamics of the early universe and a discussion of our BBN and neutrino decoupling calculations. We then discuss entropy generation, alterations of neutrino energy spectra, radiation energy density, and nucleosynthesis that accompany dark photon production and decay. Conclusions are given in section 3.4. In what follows we will use the natural units $\hbar = c = 1$ throughout this paper unless otherwise specified. The electric charge is $e = \sqrt{4\pi\alpha} \approx 0.303$ with $\alpha \approx 1/137$ being the fine-structure constant.

3.2 Thermally-produced dark photons in the early universe

In this section we describe our calculations for the production and decay of dark photons in the early universe. For the ranges of dark photon masses and couplings to the standard model and the epochs in the early universe we consider here, dark photon equilibrium does not occur. Instead, competition between out-of-equilibrium dark photon production and decay produces an ephemeral freeze-in abundance of these particles. Since the time history of this population of dark photons determines the history of, for example, entropy generation and dilution, and since our constraints are predicated on alteration of observables stemming from those histories, our calculations must accurately capture the physical state of the plasma, neutrino, and dark photon components self-consistently.

3.2.1 Pair-annihilation in a dense medium

Freeze-in dark photons can be produced coherently via photon-dark photon adiabatic conversion or incoherently from interactions with electromagnetic (EM) charge currents. While the former production channel could play an important role in the relic dark photon production at late times, it is suppressed for the case where $m_{A'} >$ MeV, with peak production occurring before or during BBN. This is because the scattering rate between photon and SM charged particles at the resonance temperature is large enough that the build-up of the relative phase between photon and dark photon states is strongly suppressed [109] – this is essentially a quantum Zeno effect.

As for the latter production mechanism, there are several possible incoherent production channels, e.g., Compton-like scattering, lepton-pair annihilation into one dark photon, or the same annihilation into one dark photon and one SM photon. When $T \ll m_e$, Compton-like scattering is the dominant channel for dark photon production. When $T \gtrsim m_e$, pair annihilation into one dark photon is the dominant channel. The same annihilation into one dark photon and one SM photon is suppressed by a factor $\alpha \approx 1/137$ due to an additional vertex which makes this channel subdominant. In this work we are interested in the dark photons that are produced abundantly early on, and then decay away during the weak decoupling and BBN epochs. The ranges of dark photon mass and standard model couplings we consider, together with this target range of decay lifetime, picks out epochs with $T \gtrsim m_e$ where lepton- or quark-pair annihilation into one dark photon are the dominant production channels.

In general, the conditions of finite temperature and density characteristic of the early universe plasma will affect the pair-annihilation dark photon production rate [133, 134]. The origin of these effects can be put into the language of classical physics: the electric field of the propagating EM wave causes acceleration of free electrons in the medium, altering the dielectric function (dispersion relation) of the EM wave. This in-medium plasma effect produces a standard model (SM) photon self energy. If there is dark photon kinetically mixed with SM photon, then this effect also alters the effective kinetic mixing between SM photon and dark

photon. A consequence of this is an enhanced dark photon emission rate.

The plasma medium-induced self-energy of a SM photon is described by adding an additional potential term $-\frac{1}{2}A_\mu \Pi^{\mu\nu} A_\nu$ to the vacuum Lagrangian in equation (3.1), where $\Pi^{\mu\nu}$ is the EM polarization tensor. Rotating away the kinetic mixing term and projecting the vector fields onto one single polarization at a time, we obtain the in-medium Lagrangian for polarization a presented in the mass basis quantities $\tilde{A}_a$ (or $\tilde{F}_{a,\mu\nu}$) and $\tilde{A}'_a$ (or $\tilde{F}'_{a,\mu\nu}$) as (see appendix 3.B)

$$\begin{aligned}\mathscr{L}_{\mathrm{IM},a} \supset & -\frac{1}{4}\tilde{F}_{a,\mu\nu}\tilde{F}_a^{\mu\nu} - \frac{1}{4}\tilde{F}'_{a,\mu\nu}\tilde{F}'^{\mu\nu}_a + \frac{1}{2}{m_{A'}}^2 \tilde{A}'_{a,\mu}\tilde{A}'^{\mu}_a \\ & + \frac{1}{2}\pi_a \tilde{A}_{a,\nu}\tilde{A}^\nu_a + e\left(\tilde{A}_{a,\mu} + \frac{\kappa m^2_{A'}}{m^2_{A'} - \pi_a}\tilde{A}'_{a,\mu}\right) J^\mu_{\mathrm{em}},\end{aligned} \tag{3.2}$$

where a is either one of the two transverse modes ($\pm$T) or the longitudinal mode (L), and J^μ_{em} is the electric charge current. The function $\pi_a = \pi_a(\omega, \mathbf{k})$ is the EM polarization function for the polarization state a. Explicit forms for these are given in equations (3.29) and (3.30). From the last term in equation (3.2), we see that the *effective* coupling between the dark photon $\tilde{A_\mu}'$ and the standard model electric charge current J^μ_{em} is

$$e\kappa_{\mathrm{eff},a} = \frac{e\,\kappa m^2_{A'}}{\sqrt{\left(m^2_{A'} - \mathrm{Re}\,\pi_a\right)^2 + \left(\mathrm{Im}\,\pi_a\right)^2}}. \tag{3.3}$$

Certainly, the physics should be independent of the basis we choose. So in the following discussion, we will refer to the rotated (mass state) $\tilde{A}'$ as the dark photon and designate this simply as A'.

The physical meaning of the real and imaginary parts of π_a follows from considerations of finite temperature field theory. The real part can be interpreted as the effective photon mass in the plasma. With the polarization vectors chosen in equations (3.26) and (3.27), the dispersion relation for EM waves follows the form $\omega^2 = |\mathbf{k}|^2 + \mathrm{Re}\,\pi_a$ for $a = \pm$T and L.

The imaginary part of π_a describes the rate at which the non-equilibrium dark photon distribution function evolves toward thermal equilibrium. Quantitatively, it is $\mathrm{Im}\,\pi_a =$

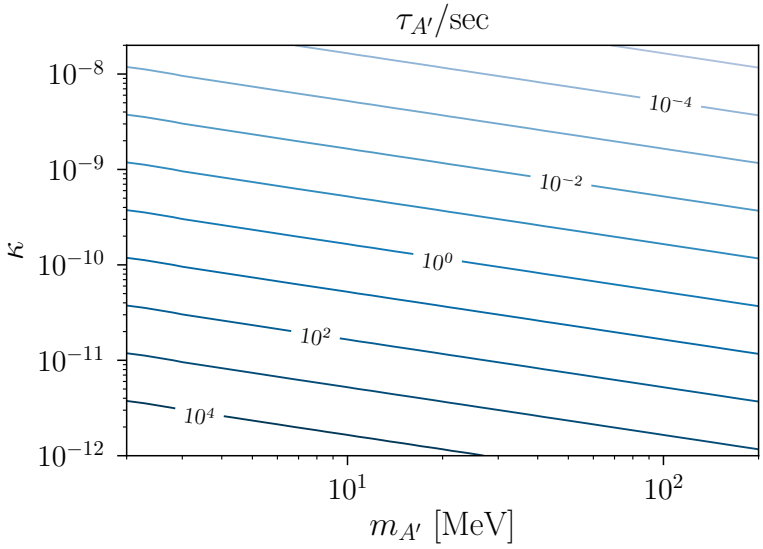

Figure 3.1. Contours of constant dark photon life time $\tau_{A'}$ (in seconds) as functions of κ and $m_{A'}$.

$-\omega\left(\Gamma^{\mathrm{abs}}_{A_a}-\Gamma^{\mathrm{prod}}_{A_a}\right)$, where $\Gamma^{\mathrm{abs}}_{A_a}$ and $\Gamma^{\mathrm{prod}}_{A_a}$ denote the absorption rate and spontaneous production rate, respectively [135]. In a local thermal (steady state) equilibrium, detailed balance would dictate that $\Gamma^{\mathrm{prod}}_{A_a}=e^{-\omega/T}\Gamma^{\mathrm{abs}}_{A_a}$.

Specifically, $\Gamma^{\mathrm{prod}}_{A_a}$ in this work denotes the annihilation rate for lepton or quark pairs into one SM photon and is evaluated as (see appendix 3.C)

$$\Gamma^{\mathrm{prod}}_{A_a}(\omega)=\frac{1}{2\omega}\int\frac{d^3\mathbf{p}}{(2\pi)^3\,2E_{\mathbf{p}}}\frac{d^3\mathbf{q}}{(2\pi)^3\,2E_{\mathbf{q}}}\frac{1}{e^{E_{\mathbf{p}}/T}+1}\frac{1}{e^{E_{\mathbf{q}}/T}+1}\sum_{\mathrm{spin}}|\mathscr{M}_{l\bar{l}\to A_a}|^2\,(2\pi)^4\,\delta^{(4)}\left(k-p-q\right), \tag{3.4}$$

where $\mathscr{M}_{l\bar{l}\to A_a}$ is the matrix element for lepton-pair (momenta $\mathbf{p}$ and $\mathbf{q}$) annihilation to one vector boson through a standard EM vertex and the sum is over initial lepton spin states. As a result, the dark photon emission rate in a dense medium is $\kappa^2_{\mathrm{eff},a}\Gamma^{\mathrm{prod}}_{A_a}$. The evolution of the total number density of dark photons can be calculated from the Boltzmann equation as

$$\dot{n}_{A'_a}+3Hn_{A'_a}=\int\frac{d^3\mathbf{k}}{(2\pi)^3}\,\kappa^2_{\mathrm{eff},a}\,\Gamma^{\mathrm{prod}}_{A_a}(\omega)-n_{A'_a}\,{\tau_{A'}}^{-1}, \tag{3.5}$$

where H is the Hubble parameter and ${\tau_{A'}}^{-1}$ is the dark photon decay rate and is given by [122]

$$ {\tau_{A'}}^{-1} = \frac{1}{3}\,\alpha\kappa^2 m_{A'}\left(1+2\frac{m_l^2}{{m_{A'}}^2}\right)\sqrt{1-4\frac{m_l^2}{{m_{A'}}^2}}, \tag{3.6} $$

with m_l the appropriate lepton rest mass. In figure 3.1, we show the contours of dark photon lifetime, $\tau_{A'}$, as functions of κ and $m_{A'}$.

3.2.2 Resonant vs. continuum production

It is clear from the effective coupling expression in equation (3.3) that the dark photon production rate is enhanced when $m_{A'} = \mathrm{Re}\,\pi_a$. Satisfying this "resonance" condition is tantamount to mode matching, requiring a mode solution $(\omega, \mathbf{k})$ such that the dispersion relation for the dark photon is $\omega^2 = |\mathbf{k}|^2 + m_{A'}^2$ and that for in-medium photon mode is $\omega^2 = |\mathbf{k}|^2 + \mathrm{Re}\,\pi_a(\omega,\mathbf{k})$. We can explore the range of temperature conditions in the early universe where the resonance condition can be satisfied by graphically showing the dark photon and in-medium SM photon dispersion relations. We show these in figure 3.2 for both longitudinal and transverse modes in a relativistic plasma ($T \gg m_e$). From these plots, we see that: (1) resonant dark photon emission of the transverse mode occurs in a narrow range of temperature between $8\,m_{A'}$ and $10\,m_{A'}$; and (2) resonant emission of longitudinal mode occurs at $T \gtrsim 10\,m_{A'}$, which is much higher than the temperature condition for the transverse resonance. In both cases, however, the resonant emission always ceases as $T \lesssim 8\,m_{A'}$.

When the kinetic mixing is off-resonance, i.e., $|{m_{A'}}^2 - \mathrm{Re}\,\pi_a| \gg |\mathrm{Im}\,\pi_a|$, the effective coupling constant becomes $e^2\kappa_{\mathrm{eff},a}^2 = e^2\kappa^2 {m_{A'}}^4/\left({m_{A'}}^2 - \mathrm{Re}\,\pi_a\right)^2$. In the low temperature regime where $\mathrm{Re}\,\pi_a \ll m_{A'}^2$, the effective kinetic mixing reduces to the vacuum value κ. The continuum dark photon emission width in this regime is just $\kappa^2\Gamma_a^{\mathrm{prod}}$. In the high temperature regime where $\mathrm{Re}\,\pi_a \gg m_{A'}^2$, the effective coupling reduces to $\kappa {m_{A'}}^4/{\mathrm{Re}\,\pi_a}^2$, so the continuum emission rate is suppressed by a factor ${m_{A'}}^4/{\mathrm{Re}\,\pi_a}^2$ relative to the rate in the low temperature regime [114]. Moreover, there is always more time to produce dark photons at low temperatures than at high

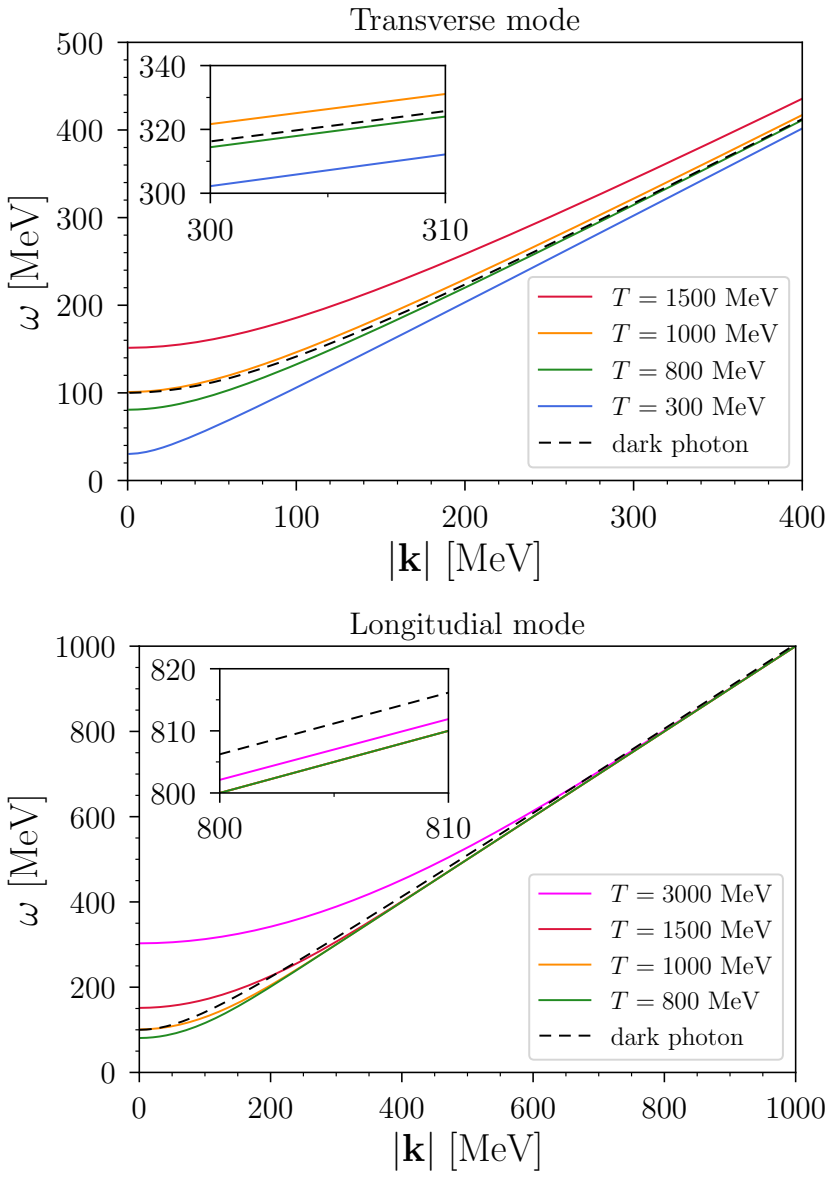

Figure 3.2. Dispersion relations of the transverse and longitudinal modes for SM photons in a relativistic plasma. The solid curves denote the SM photon dispersion relation at various plasma temperatures. The black dashed curve denotes the dispersion relation of a dark photon model with $m_{A'} = 100\,\text{MeV}$. (**top**) The transverse SM photon dispersion relation curve crosses the dark photon dispersion relation curve in the range $8\,m_{A'} \lesssim T \lesssim 10\,m_{A'}$. Emission of dark photons in either of the two transverse modes is resonantly enhanced in this temperature range. (**bottom**) The longitudinal SM photon dispersion relation curve crosses the dark photon dispersion relation curve when $T > 10\,m_{A'}$. Emission of dark photons in the longitudinal mode is resonantly enhanced in this range. (**inset**) The insets show a restricted range in $|\mathbf{k}|$ where the dispersion relations are close to their asymptotic limits with respect to one another.

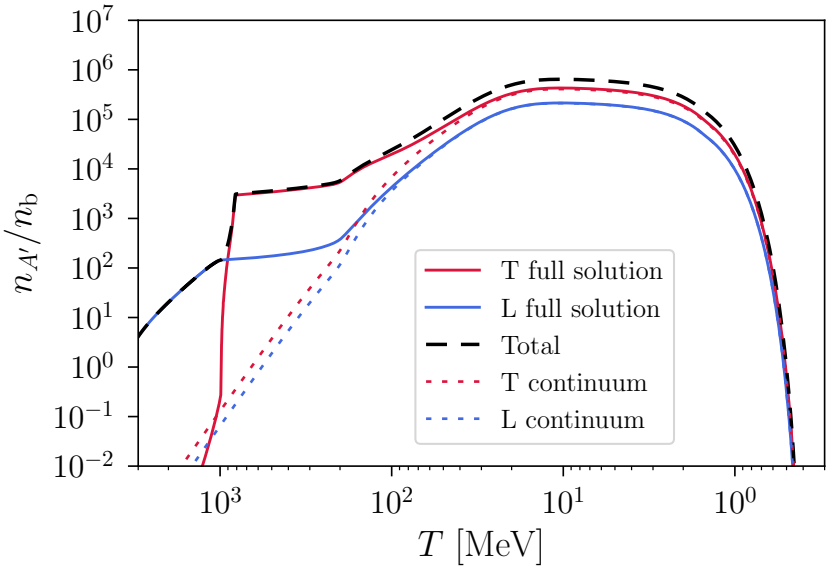

Figure 3.3. Evolution of the ratio of dark photons to baryons plotted against plasma temperature for a model where $m_{A'} = 100\,\text{MeV}$ and $\kappa = 10^{-10}$. Red (blue) lines give the transverse (longitudinal) mode. For a given mode, dotted lines show the production history if we ignore plasma effects at all temperatures, i.e., $\kappa_{\text{eff,a}} = \kappa$. The result of ignoring the plasma effects gives the continuum contribution. Conversely, solid lines show the complete production history if we include the plasma effects encapsulated in equation (3.3). The dashed black line gives the total number of dark photons for the three modes ($a = \pm\text{T}, \text{L}$) in the full solution. Resonant production within the plasma occurs at early times ($T \gtrsim 8\,m_{A'}$) while continuum production dominates at late times ($T \lesssim m_{A'}$).

temperatures because the Hubble expansion rate in these radiation dominated conditions drops with decreasing temperature, $H \sim T^2/m_{\text{pl}}$ with m_{pl} the Planck mass. As a result, the continuum dark photon production is always more significant at low temperatures than at high temperatures.

We would like to understand the role of the resonant production channel in contributing to the overall dark photon yield, and assess its significance relative to continuum production. As an example, in figure 3.3 we show the dark photon production history for a specific dark photon mass $m_{A'} = 100\,\text{MeV}$. The solid lines show the full solutions for dark photon emission with in-medium plasma effect included. The solid lines are color coded for longitudinal and transverse modes. On the other hand, the dashed lines show the production histories when no plasma effects are included. The rapid rise in dark photon number density in the temperature range $8\,m_{A'} < T < 10\,m_{A'}$, and at $T > 10\,m_{A'}$, is a consequence of resonant production of transverse and

longitudinal modes. These histories agree with those shown in figure 3.2. For the lepton/quark-pair annihilation production channel, we can conclude from the calculations shown in the figure that longitudinal mode resonant production is insignificant relative to resonant transverse mode production. See, for example, Ref. [48] for a discussion of stellar conditions in the regime where the dark photon mass is less than the plasma frequency, $m_{A'} < \omega_{\rm p}$, and where, consequently, the resonant dark photon emission production of longitudinal modes dominates over the resonant transverse mode production rate. On the other hand, the continuum production rates for both transverse and longitudinal modes are initially small at $T > 10\, m_{A'}$ as a consequence of the extra suppression factor ${m_{A'}}^4/\mathrm{Re}\,{\pi_a}^2$, but these eventually dominate the total dark photon emission when $T \lesssim m_{A'}$. Comparing the full and continuum solutions, we see that: (1) resonant production is important only at $T \gtrsim 8\, m_{A'}$; and (2) eventually the continuum production dominates over the resonant production. Overall, the dark photon yield from the resonant production channels contributes only $\mathcal{O}\,(\lesssim 5\%)$ to the total dark photon abundance at $T \approx 0.1\, m_{A'}$. Our calculations employ the same thermal effects on dark photon production as in Ref. [122], with similar results.

For the numerical simulations presented in the following sections, we include only the continuum emission channels for dark photon production in both the transverse and longitudinal modes. Resonant emission is not included in these calculations.

3.3 Alteration of relic neutrino density and nucleosynthesis yield

The key result of out of equilibrium dark photon decay will be to add entropy, altering the time-temperature-scale factor relationship relative to a standard-model-only cosmology. The *final* baryon-to-photon ratio of the universe we live in is a measured quantity. We can infer the entropy per baryon from this quantity. The entropy per baryon, in units of Boltzmann's constant

$k_{\rm b}$, for the plasma of electrons, positrons, and photons is

$$\begin{aligned} s_{\rm pl} &= \left(\frac{\pi^4}{45\,\zeta\,(3)}\right)\left(\frac{g_{\star S}}{\eta}\right) \\ &\approx \left(5.91\times 10^9\right)\left(\frac{g_{\star S}}{2}\right)\left(\frac{6.09\times 10^{-10}}{\eta}\right), \end{aligned} \tag{3.7}$$

where $\eta \equiv n_b/n_\gamma$ is the baryon-to-photon ratio and $g_{\star S}$ is the effective number of degrees of freedom carrying the entropy [132]. The PLANCK satellite derives $\eta_{\rm cmb} = 6.09\times 10^{-10}$ at the time of recombination ($T \sim 0.2$ eV) [136], which yields $s_{\rm pl,cmb} = 5.91\times 10^9$. In standard cosmology with temperature low enough that the baryon number is conserved, $s_{\rm pl}$ is a co-moving invariant. With the presence of entropy injection from dark photon decay, however, the plasma would start out with a lower value of $s_{\rm pl}$ so that its final value at the recombination epoch will match the CMB-determined value, $s_{\rm pl,cmb}$.

3.3.1 Entropy generation and BBN computation

We use our code BURST [131] to calculate the effects of the production and decay of dark photons during the weak decoupling and BBN epochs. BURST primarily evolves the plasma temperature, neutrino energy spectra, and primordial abundances through these epochs. Adding dark photon physics to this calculation induces three related changes to the standard model case, namely

1. A different Hubble expansion rate H,
2. A different plasma temperature versus scale factor (and time) history,
3. An evolving baryon-density and $s_{\rm pl}$.

To self-consistently follow the three changes we introduce an energy-density variable for the dark photons

$$\rho_{A'} = m_{A'} n_{A'}, \tag{3.8}$$

where $n_{A'}$ is the total proper number density of dark photons as given by the solutions to equation (3.5). In writing equation (3.8) we have ignored the kinetic contribution to the dark photon energy density. Therefore, our calculations give underestimates of the effects induced by the presence of dark photons. Neglecting the kinetic energy content of the dark photon field makes only small changes, especially where most decays occur for $m_{A'} \gg T_{\rm decay}$.

We add $\rho_{A'}$ to the energy densities of the other components to calculate the Hubble expansion rate H. During dark photon production and decay, we assume the energy density of the electromagnetic plasma instantly equilibrates, which induces a change in the plasma temperature time-derivative [137]

$$\frac{dT}{dt} = -3H \frac{\rho_{\rm pl} + P_{\rm pl} + \frac{1}{3H}\left.\frac{dQ}{dt}\right|_T}{\frac{d\rho_{\rm pl}}{dT}}, \tag{3.9}$$

where $\rho_{\rm pl}$ is the energy density of the plasma (less baryons); $P_{\rm pl}$ is the pressure exerted by all plasma components; $dQ/dt|_T$ is the rate of heat gain or lost from nuclear reactions, neutrino scattering/decoupling, and dark photon evolution; and $d\rho_{\rm pl}/dT$ is the temperature derivative of the plasma energy density components (including baryons). We model the energy subtraction (injection) from dark photon production (decay) using the heat sink (source)

$$\left.\frac{dQ}{dt}\right|_T = -\left.\frac{dQ}{dt}\right|_{\rm nuc} + \left.\frac{dQ}{dt}\right|_\nu - \left.\frac{dQ}{dt}\right|_{A' \leftrightarrow l\bar{l}}, \tag{3.10}$$

$$= -\left.\frac{dQ}{dt}\right|_{\rm nuc} + \left.\frac{dQ}{dt}\right|_\nu + m_{A'}\frac{dn_{A'}}{dt}. \tag{3.11}$$

$$\tag{3.12}$$

An injection of heat will raise the entropy per baryon within the plasma $s_{\rm pl}$, which is equivalent to diluting the baryon number density. Therefore, we start with a low entropy-per-baryon and allow the dark photon decays to raise the entropy per baryon (or lower the baryon number density) to a value consistent with photon decoupling, namely $s_{\rm pl} = 5.91 \times 10^9$ [136]. For each dark photon model (set of dark photon mass and coupling parameters), we iterate on the starting entropy to

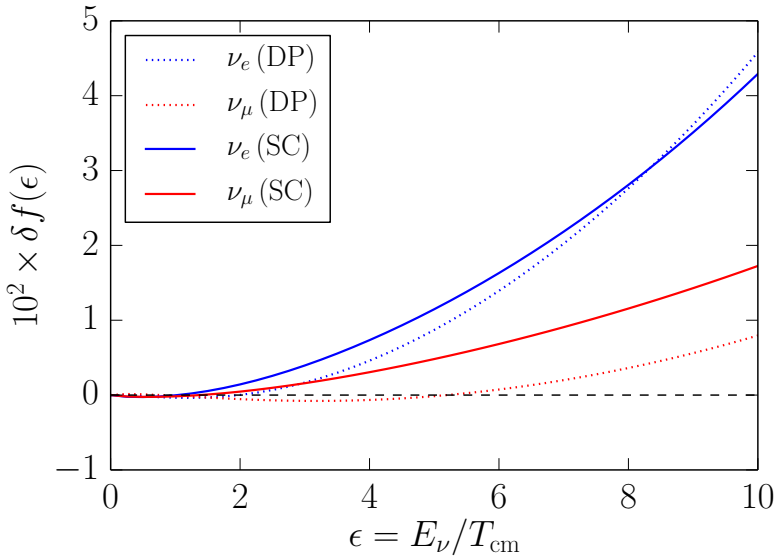

Figure 3.4. Relative differences from FD [equation (3.14)] for a dark photon model (dotted) and standard cosmology (solid) versus ε at freeze-out. The parameters for the dark photon model are $m_{A'} = 10\,\mathrm{MeV}$ and $\kappa = 2 \times 10^{-10}$.

find the final entropy consistent with Ref. [136], $s_{\rm pl,cmb}$.

3.3.2 Neutrino Spectra

As the dark photons decay, they inject heat into the electromagnetic plasma. This heat flow changes the temperature of the plasma giving a different thermal history for the early universe as compared to the standard cosmology. For the dark photon masses we consider in this work, the neutrinos cannot directly partake in this heat flow from dark photon decay. However, a warmer plasma will precipitate a larger heat flow from the plasma into the neutrino seas during neutrino decoupling. As a result, dark photon decays do affect the neutrino spectra indirectly.

As an illustrative example, we take a specific case for dark photon rest mass and coupling to the standard model and calculate in depth how the production and decay of this particle affects weak decoupling and entropy flow. In particular, we show the neutrino energy spectral distortions

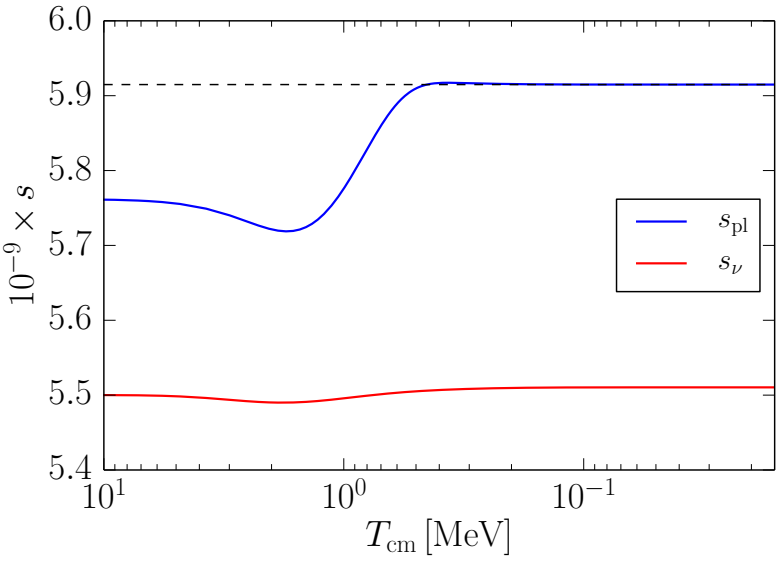

Figure 3.5. The plasma (blue) and neutrino (red) entropies per baryon versus $T_{\rm cm}$ for a dark photon model. The parameters for the dark photon model are $m_{A'} = 10\,\text{MeV}$ and $\kappa = 2 \times 10^{-10}$. The black dashed line is the entropy per baryon as inferred from the CMB in Ref. [136].

and the evolution of entropy in figures 3.4, 3.5, and 3.6. For this example case we choose

$$m_{A'} = 10\,\text{MeV}, \quad \kappa = 2 \times 10^{-10}, \tag{3.13}$$

and use the standard cosmological model (i.e., a zero dark photon density) for a baseline comparison. We have picked this particular dark photon model in equation (3.13) because of the associated large change in the entropy per baryon during neutrino decoupling. Figure 3.4 shows the relative changes in the occupation number from FD (Fermi-Dirac) equilibrium

$$\delta f(\varepsilon) = \frac{f(\varepsilon) - f^{(\text{eq})}(\varepsilon)}{f^{(\text{eq})}(\varepsilon)}, \quad f^{(\text{eq})}(\varepsilon) = \frac{1}{e^{\varepsilon} + 1}, \tag{3.14}$$

plotted against the comoving invariant $\varepsilon = E_\nu / T_{\rm cm}$, where E_ν is the neutrino energy and $T_{\rm cm}$ is a proxy for (inverse) scale factor [138]. Solid curves give the deviations from FD equilibrium in the case of the standard cosmology, whereas the dotted lines are for the dark photon model

in equation (3.13). The blue curves are for the electron-flavor neutrino and the red for μ-flavor. The τ-flavor neutrinos are degenerate with μ-flavor and the antineutrinos are degenerate with the neutrinos in our model of neutrino transport sans oscillations. The black dashed line at zero represents FD equilibrium. The dashed and solid lines deviate from one another, showing two unique histories for neutrino decoupling, one with the dark photon with the assumed parameters, one without.

As the dark photons decay, the entropy increase in the plasma dilutes the neutrino seas and changes the thermal history of the early universe. We show the entropic history for the dark photon decay scenario in figure 3.5. In this figure, entropy is plotted as a function of the comoving temperature quantity, $T_{\rm cm}$. The blue curve gives the entropy per baryon in the plasma, $s_{\rm pl}$, and the red curve the entropy per baryon residing in the neutrino seas, s_ν. We calculate the plasma entropy from equilibrium thermodynamics. The neutrino seas are out-of-equilibrium so we calculate that entropy using non-equilibrium statistical mechanics, i.e., Boltzmann neutrino energy transport (see section IV in Ref. [131]). Both quantities count the number of microstates available to the two subsystems. The dashed black horizontal line in figure 3.5 is the entropy-per-baryon inferred from Ref. [136]. There is a small increase in s_ν arising from neutrino transport and equivalently encapsulated in the dotted curves of figure 3.4 at freeze-out. This small increase is accompanied by a small decrease in $s_{\rm pl}$ which is dwarfed by the large increase in the entropy from dark photon decay. The phenomenon of dilution is the increase in the ratio of the entropic quantities from early times to late. The change in the entropy gives a nonstandard thermal history for the early universe. We can summarize the thermal history using the ratio of $T_{\rm cm}$ to T at freeze-out

$$\left.\frac{T_{\rm cm}}{T}\right|_{\rm f.o.} = 0.7082 \quad m_{A'} = 10\,{\rm MeV}, \kappa = 2\times 10^{-10}, \tag{3.15}$$

$$\left.\frac{T_{\rm cm}}{T}\right|_{\rm f.o.} = 0.7138 \quad \text{Standard Cosmology (SC)}. \tag{3.16}$$

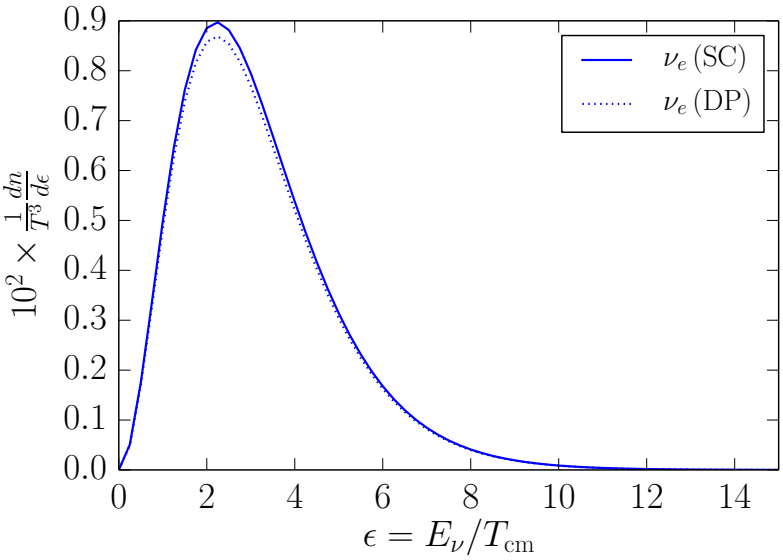

Figure 3.6. Differential ν_e number densities scaled by plasma temperature [equation (3.18)] for a dark photon model (dotted) and standard cosmology (solid) versus ε at freeze-out. The parameters for the dark photon model are $m_{A'} = 10\,\mathrm{MeV}$ and $\kappa = 2 \times 10^{-10}$.

Figures 3.4 and 3.5 show that the neutrinos experience two competing and opposing effects: an increase in the heat flow from the plasma to the neutrino seas at the level of a few percent deviation (figure 3.4); and dilution of the neutrino seas at a level of 20% (figure 3.5). The former effect raises the number of neutrinos at a given energy bin ε and $T_{\rm cm}$, which we write as a differential number density

$$\frac{dn_i}{d\varepsilon} = T_{\rm cm}^3 \frac{\varepsilon^2}{2\pi^2} f_i(\varepsilon), \tag{3.17}$$

for a given neutrino flavor i. The later effect decreases the number of neutrinos with respect to photons which we encode in the ratio of $T_{\rm cm}/T$. Figure 3.6 encapsulates both effects, showing a scaled differential number density

$$\frac{1}{T^3}\frac{dn}{d\varepsilon} = \left(\frac{T_{\rm cm}}{T}\right)^3 \frac{\varepsilon^2}{2\pi^2} f(\varepsilon), \tag{3.18}$$

plotted against ε. We only plot the scaled differential number densities for electron-flavor

neutrinos in the dark photon decay scenario (dotted line) and the standard cosmology (solid line). The μ-flavor quantities are qualitatively identical. The scaled differential number density is a scale-dependent quantity, so we plot figure 3.6 at the respective freeze-out epochs for each scenario which would occur at different T and $T_{\rm cm}$.

The previous exposition has delved into the details of neutrino transport with dark photons. For the specific model we considered, the dominant effect on the neutrino number density (and by extension energy density) was dilution. Energy flow from neutrino transport adds on order an 1% increase to the total neutrino energy density. The increase is dependent on the particular model of dark photons. $\mathcal{O}(1\%)$ contributions may be important in future high-precision modeling of BSM cosmologies and we emphasize the need for such calculation if/when the data warrant it. For the purposes of this work, we will focus on dilution when discussing the dark photon parameter space in its entirety, and discuss sub-dominant transport effects for specific models.

3.3.3 Radiation energy density

The first observable consequence of entropy injection and dilution is decreasing the neutrino radiation energy density (as parameterized by $N_{\rm eff}$) compared to the value predicted in the standard cosmology. In this subsection, we first calculate the dilution effect in the dark photon model and show the changes in $N_{\rm eff}$ for the full model parameter space; this would be for the case without including energy transport between neutrinos and the plasma. We then discuss the effect of neutrino-energy transport on $N_{\rm eff}$ for a few sets of dark photon model parameters and show the non-linear scaling of the $N_{\rm eff}$ correction with either $m_{A'}$ or κ.

Sharp neutrino decoupling

The energy density of the neutrino seas is solely a function of $T_{\rm cm}$

$$\rho_\nu = 6\left(\frac{7}{8}\right)\left(\frac{\pi^2}{30}\right)T_{\rm cm}^4 \tag{3.19}$$

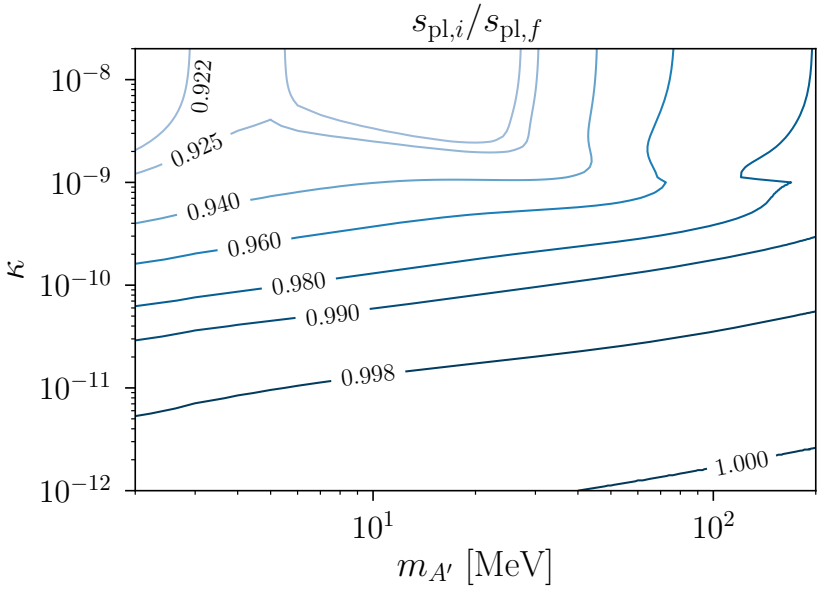

Figure 3.7. Contours of constant initial-to-final entropy ratios ($s_{\mathrm{pl},i}/s_{\mathrm{pl},f}$) plotted in the κ versus $m_{A'}$ parameter space. The contours with values below 1.0 indicate an increase in entropy due to the dark photon production and decay.

when ignoring out-of-equilibrium contributions. The CMB power spectrum is sensitive to the radiation energy density, ρ_{rad}, of the early universe, which we parameterize using the quantity N_{eff} and plasma temperature T

$$\rho_{\mathrm{rad}} = \left[2 + \frac{7}{4}\left(\frac{4}{11}\right)^{4/3} N_{\mathrm{eff}}\right] \frac{\pi^2}{30} T^4. \tag{3.20}$$

If we take the radiation energy density to be the sum of the photon and neutrino components, we find

$$N_{\mathrm{eff}} = 3\left(\frac{11}{4}\right)^{4/3}\left(\frac{T_{\mathrm{cm}}}{T}\right)^4. \tag{3.21}$$

After weak decoupling, dark photon decay injects entropy only into the electromagnetic plasma. This process results in the dilution of both the baryon number and the neutrino energy densities. If $s_{\mathrm{pl},i}$ is the entropy per baryon in the plasma at an initial epoch, and $s_{\mathrm{pl},f}$ is the same

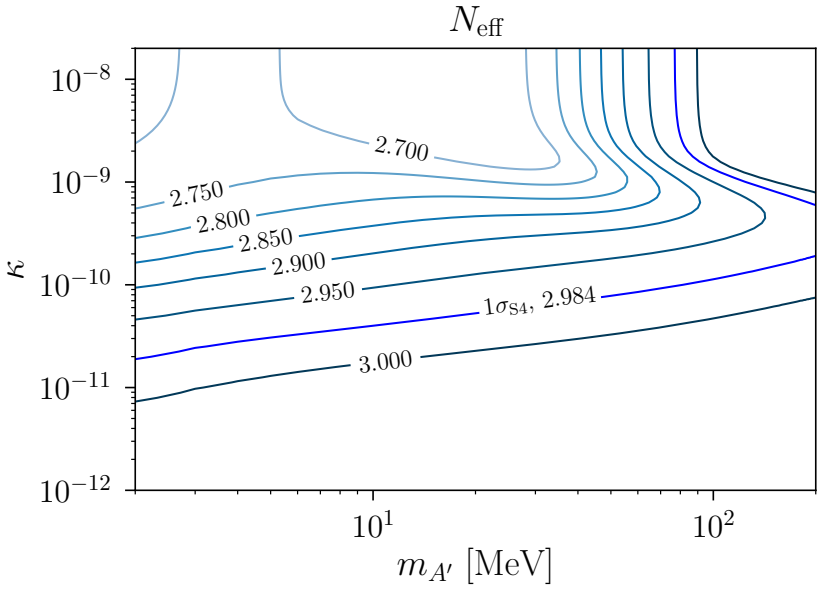

Figure 3.8. Contours of $N_{\rm eff}$ are shown for values of dark photon mass $m_{A'}$ and mixing parameter κ. For reference, we also plot the QED-only prediction of $N_{\rm eff} = 3.011$ in the absence of neutrino-energy transport. The blue contour is down from 3.011 by $1\,\sigma_{\rm S4}$ where we quote the measurement uncertainty $1\,\sigma_{\rm S4} = 0.027$ from the CMB Stage-4 science book [100].

quantity at a final epoch, then the ratio behaves like the following

$$\frac{s_{{\rm pl},i}}{s_{{\rm pl},f}} = \left(\frac{\frac{2\pi^2}{45} g_{\star S}^{(i)} T_i^3}{\frac{2\pi^2}{45} g_{\star S}^{(f)} T_f^3}\right)\left(\frac{n_{b,f}}{n_{b,i}}\right) = \frac{g_{\star S}^{(i)}}{g_{\star S}^{(f)}}\left(\frac{T_i a_i}{T_f a_f}\right)^3 = \frac{11}{4}\left(\frac{T_{\rm cm}}{T}\right)^3_{\rm f.o.}, \tag{3.22}$$

where we have selected the initial epoch such that $T_{{\rm cm},i} = T_i$ and the final epoch such that the ratio $T_{\rm cm}/T$ has reached a freeze-out value, i.e., all of the plasma entropy resides in SM photons. Figure 3.7 shows the contours of $s_{{\rm pl},i}/s_{{\rm pl},f}$ in the κ vs. $m_{A'}$ parameter space. All contours are less than or equal to unity, showing that the physics of dark photons precipitates dilution.

If we compare equation (3.22) to equation (3.21) evaluated at freeze-out, we find

$$N_{\rm eff} = 3\left(\frac{s_{{\rm pl},i}}{s_{{\rm pl},f}}\right)^{4/3}. \tag{3.23}$$

As a result, we expect contours of $N_{\rm eff}$ to correspond directly to the contours of $s_{{\rm pl},i}/s_{{\rm pl},f}$ in figure 3.7. That is, a smaller value of $s_{{\rm pl},i}/s_{{\rm pl},f}$ (a larger dilution effect) would lead to a smaller

value of $N_{\rm eff}$ (a more diluted neutrino radiation density). Figure 3.8 shows the contours of $N_{\rm eff}$ as functions of κ and $m_{A'}$ in the case of dark photon decay. Indeed, the $N_{\rm eff}$ contours do follow the same general trend of the dilution contours in figure 3.7. For low $m_{A'}$, a large value of κ induces rapid dark photon production and results in a non-negligible abundance. In addition, peak production occurs in the temperature range $0.1\,m_{A'} \lesssim T_{\rm peak} \lesssim m_{A'}$. For the low end of our mass-range study, peak production occurs after the sharp neutrino decoupling we have instituted for the parameter space scan. This added entropy from dark photon decay dilutes the thermal neutrino seas and lowers $N_{\rm eff}$ to a value smaller than 3. At large κ and $m_{A'} \gtrsim 100$ MeV, the dark photons are both created and decay away before neutrino decoupling, and thus there is little or no dilution on the neutrino energy density. The difference in the contour patterns between figures 3.7 and 3.8 is a result of how we calculate the initial entropy. We fix the initial epoch at $T = 30\,\mathrm{MeV}$ regardless of $m_{A'}$. For large $m_{A'}$, the entropy is changing in this initial regime and so the respective contours in figure 3.7 do not meet the criteria used to derive equation (3.23), and hence diverge from the more precise contours of figure 3.8.

We plot a blue contour at $N_{\rm eff} = 2.984$ on figure 3.8. This contour uses a $1\,\sigma_{\rm S4} = 0.027$ uncertainty in $N_{\rm eff}$ from a CMB Stage-4 forecast [100]. The $1\,\sigma_{\rm S4}$ difference is between the contour level and the QED-only prediction of $N_{\rm eff} = 3.011$ in the absence of heat flow from neutrino-energy transport [138]. The specific location in the dark-photon parameter space for the $1\,\sigma$ contour would be the same if transport were to add an offset to all of the contour levels, although $N_{\rm eff}$ would take on a value ≈ 3.02 for the $1\,\sigma$ contour in that scenario. However, this procedure relies on the assumption that the effect of transport is independent of the dark photon physics. We expand upon this detail in the following section.

Effects from neutrino energy transport

The contours of figure 3.8 are for a model of neutrino decoupling which does not include energy transport between neutrinos and charged leptons. In this scenario, the baseline QED-only calculation would yield $\Delta N_{\rm eff} \equiv N_{\rm eff} - 3 = 0.011$, where the departure from exactly three is due

Table 3.1. Table of values related to $N_{\rm eff}$. First and second columns are the dark photon mass and coupling, respectively. Third and fourth columns are the value of $N_{\rm eff}$ with only QED effects and with transport included, respectively. Fifth column is the difference between the fourth and third columns. Sixth column is that difference scaled by the uncertainty in $N_{\rm eff}$ as forecast by CMB Stage-4 [100]. The first row gives the values calculated in the standard cosmology with our code.

$m_{A'}$ [MeV]	κ	$N_{\rm eff}$ (QED only)	$N_{\rm eff}$ (w/ trans.)	Diff	Diff$/\sigma_{\rm S4}$
SC		3.0113	3.0442	0.0329	1.2201
2.0	1×10^{-12}	3.0097	3.0426	0.0329	1.2192
2.0	1×10^{-11}	2.9961	3.0289	0.0327	1.2128
2.0	1×10^{-10}	2.8944	2.9237	0.0293	1.0834
2.0	1×10^{-9}	2.7201	2.7152	-0.0049	-0.1838
2.0	1×10^{-8}	2.6934	2.6838	-0.0096	-0.3560
10.0	2×10^{-12}	3.0101	3.0430	0.0329	1.2188
10.0	2×10^{-11}	2.9983	3.0306	0.0323	1.1970
10.0	2×10^{-10}	2.9012	2.9147	0.0135	0.5009
10.0	2×10^{-9}	2.7110	2.8807	0.1697	6.2866
10.0	2×10^{-8}	2.6656	2.8894	0.2238	8.2284

to finite-temperature QED effects which change the entropy of the plasma [139, 140] (see also Ref. [141] for a detailed treatment of QED effects in the early universe). In SC calculations of $N_{\rm eff}$ with neutrino transport, the effect of entropy/energy flow from the electromagnetic plasma to the neutrino energy seas increases $N_{\rm eff}$. The sole process of neutrino energy transport yields $0.033 < \Delta N_{\rm eff} < 0.035$ [142–148]. In general, the effects from transport and QED corrections cannot be incoherently summed to give the total change to $N_{\rm eff}$. The QED effects change the plasma temperature, which changes the rate of heat flow into the neutrino seas, which feeds back on the plasma temperature. However, in practice, this feedback loop is not important at the level of uncertainty in $N_{\rm eff}$ [136], and summing the two contributions gives a range $0.043 \lesssim \Delta N_{\rm eff} \lesssim 0.046$. A possible interpretation of this result is that the correction on $N_{\rm eff}$ from transport is a constant offset.

We ask the question as to whether transport provides an offset to $N_{\rm eff}$ in the BSM scenarios with dark photons. In Table 3.1, we show various values of $N_{\rm eff}$ with and without transport for a

selection of dark photon masses and couplings. For the models with $m_{A'} = 2.0\,\mathrm{MeV}$, we see that N_{eff} decreases with increasing κ whether transport is included or not. The difference between the two calculations also decreases with increasing κ, but for $\kappa \geq 10^{-9}$, the difference between the two calculations is negative. For these two models, the cooling of the plasma from dark photon production occurs during weak decoupling and induces an entropy flow from the neutrino seas to the plasma – the reverse of the process in the SC case. When dark photons begin to decay and warm the plasma, weak decoupling has nearly ceased and the neutrino seas do not partake in the increase in radiation energy density. For the models with $m_{A'} = 10.0\,\mathrm{MeV}$, we see that transport always increases N_{eff} for the range of values of κ in Table 3.1. The difference between the two calculations decreases with increasing κ, until $\kappa = 2 \times 10^{-10}$, which also is the model studied in detail in section 3.3.2. For models with $\kappa \geq 2 \times 10^{-9}$, transport precipitates larger heat flows than the baseline case of the SC, as shown in the first data row of Table 3.1. Although we only show full neutrino energy transport calculations for a small region of the parameter space in figure 3.8, it is clear that corrections from transport scale non-linearly with either $m_{A'}$ or κ and cannot be treated as an offset at the level of future precision. Lastly, we note Ref. [149] also considers the effects from neutrino energy transport in the dark photon decay scenario. Their N_{eff} result is qualitatively similar to ours.

3.3.4 Nucleosynthesis

Another observable consequence of entropy injection and dilution is the alteration of light-element abundance yields. As discussed before, an entropy injection from dark photon decay requires the plasma to start with a lower value of entropy per baryon such that dilution causes s_{pl} to rise to the CMB-determined value, namely $s_{\mathrm{pl,cmb}} = 5.91 \times 10^{9}$. From the scaling shown in equation (3.7), we see that a lower s_{pl} translates to a higher η, i.e., the primordial nucleosynthesis environment starts with more baryons in the plasma for the same T than in the case of standard cosmology. This alteration changes the nuclear reaction rates of light-element species relative to the standard cosmology case as the reactions freeze out from the NSE.

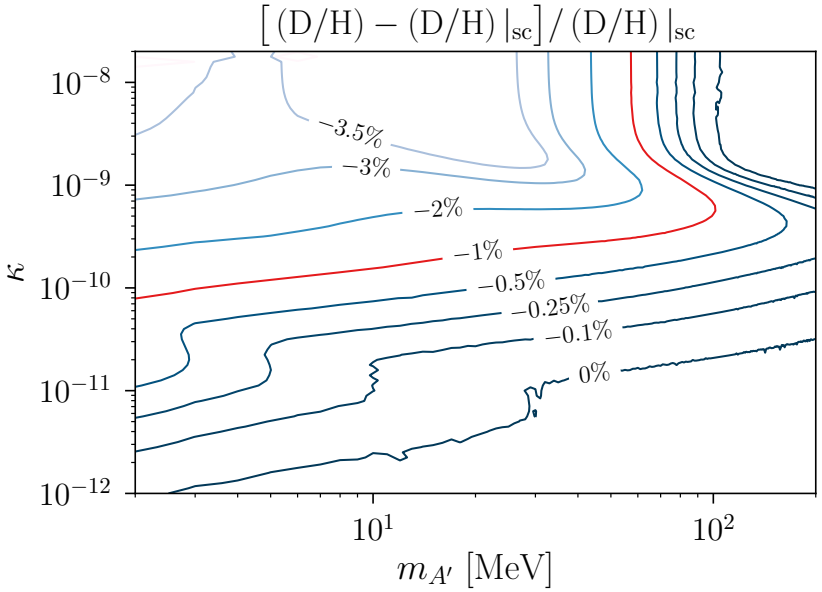

Figure 3.9. Same parameter space as figure 3.8, except here we give the percentage change of the primordial deuterium abundance yield in the dark photon model, D/H, as compared to our calculated standard model physics and standard cosmology result, $(\mathrm{D/H})|_{\mathrm{sc}} = 2.64 \times 10^{-5}$. The red contour is down from our standard model value by an assumed 1% uncertainty, i.e., $\sigma = 2.64 \times 10^{-7}$. The coarseness of the contour at 0% is a numerical artifact.

At temperatures above 100 keV, the deuterium abundance is in NSE with the free protons and neutrons. Once the free neutron abundance drops (principally from abrupt alpha particle formation) , deuterium departs from the NSE trajectory. At this point, the evolution of D/H proceeds out-of-equilibrium via the nuclear reactions, including but not limited to $n(p,\gamma)d$, $d(p,\gamma)^3\mathrm{He}$, $d(d,p)t$, and $d(d,n)^3\mathrm{He}$. A precise determination of the freeze-out (and hence primordial) ratio D/H requires data and calculations from ab initio [150, 151], lattice-QCD [152], experimental [153], and phenomenological [154–157] sources. The results of those efforts can be integrated into a BBN nuclear reaction network at the appropriate time to yield high-precision absolute BBN predictions. For the dark photon parameter space we study here, we anticipate that changes to D/H from updated reaction networks will not depend on the dynamics of dark photon decay, i.e., the effect of an updated network is to linearly perturb a baseline value. As a result, we give our D/H results as relative differences from a baseline instead of absolute abundance predictions.

Figure 3.9 shows the contours of primordial deuterium abundance yield as functions of mixing parameter and dark photon mass in the case of dark photon decay. The plot is presented as the percentage change of the primordial deuterium abundance in the dark photon model, D/H, as compared to our calculated standard model and standard cosmology result, $(\mathrm{D/H})|_{\mathrm{sc}} = 2.64 \times 10^{-5}$. At large κ and low $m_{A'}$, dark photons are created abundantly and their decay happens during BBN. That is, the plasma would start out with a lower value of s_{pl} (or higher value of η) at the BBN epoch than in the case of standard cosmology. This alters the final deuterium abundance yield. At large κ and $m_{A'} \gtrsim 100$ MeV, dark photons are both created and decay away too early (well before BBN) to have impact on primordial nucleosynthesis.

We use D/H as the diagnostic for BBN in figure 3.9 because it is well measured and is a priori the most sensitive to changes in entropy. Complementary to D/H, the helium mass fraction, Y_{P}, is also well measured and sensitive to the neutron-to-proton ratio n/p. The rates of the neutron-to-proton inter-conversion processes dictate the evolution of n/p down to low temperatures. These rates are sensitive to the distributions of neutrinos, anti-neutrinos, electrons, and positrons. In particular, four of these rates are sensitive to the dynamics of dark photons, namely

$$\nu_e + n \leftrightarrow p + e^- \tag{3.24}$$

$$e^+ + n \leftrightarrow p + \overline{\nu}_e. \tag{3.25}$$

As dark photons begin to decay, the temperature of the plasma increases. The Pauli blocking factors for the charged leptons suppress the forward rate in equation (3.24) and also the reverse rate in equation (3.25). Conversely, the FD occupation factors for the charged leptons enhance the reverse rate in equation (3.24) and the forward rate in equation (3.25). However, the two enhanced charged-lepton capture rates numerically differ from one another because of the mass threshold needed for the reaction to occur, specifically the electron in the reverse reaction in equation (3.24) must have enough kinetic energy ($\gtrsim 0.8\,\mathrm{MeV}$) to change the proton into a neutron.

Increasing the temperature increases the phase space for the electron, implying a larger rate for the reverse reaction in equation (3.24). The net effect on $n \leftrightarrow p$ inter-conversion is a slight decrease. We can make a similar argument with respect to the neutrino-capture rates, where the anti-neutrino in the reverse reaction of equation (3.25) has a threshold of $\sim 1.8\,\mathrm{MeV}$, implying that a suppression in the individual rates leads to a net increase in $n \leftrightarrow p$ inter-conversion. These two effects (along with a change in the Hubble expansion rate) cancel with one another, and n/p in the dark photon scenarios evolves similarly to the SC. There is a net decrease in Y_{P}, but this decrease is at most 1 part in 10^3 and is dwarfed by the change in D/H.

Our argument above relies on equilibrium FD distributions for the charged leptons and neutrinos. We showed in Table 3.1 that transport can induce changes in N_{eff} larger than 5%. The neutron-to-proton inter-conversion rates are sensitive to the out-of-equilibrium neutrino energy distributions, so the possibility exists that transport can induce larger changes. Indeed, the changes in Y_{P} from transport are an order of magnitude larger than those calculated with equilibrium spectra alone. However, this change is only for the most extreme models in our parameter space, is less than 1%, and still remains smaller than the relative changes in D/H.

3.3.5 Summary of results

The main results of this work are summarized by the two solid lines in figure 3.10. The blue line shows the N_{eff} value that is $1\,\sigma_{\mathrm{S4}}$ down from our baseline SC calculation of $N_{\mathrm{eff}} = 3.044$. Here we quote a measurement uncertainty $1\,\sigma_{\mathrm{S4}} = 0.027$ from CMB Stage-4 [100]. Our following conclusion includes the effect of neutrino-energy transport as a constant offset to the dilution physics from dark-photon decay. We caution against applying such an offset to all models. However, Table 3.1 shows that applying an offset is problematic for large values of κ which the $1\,\sigma$ contour largely avoids, i.e., the top-left portion of figure 3.8. We suggest the following interpretation of the blue contour in figure 3.10. Suppose future CMB Stage-4 experiments measure N_{eff} within $1\,\sigma_{\mathrm{S4}}$ down from the SC-predicted value, $N_{\mathrm{eff}} = 3.044$. From this outcome, we cannot conclude there is entropy generation and dilution from late decay of

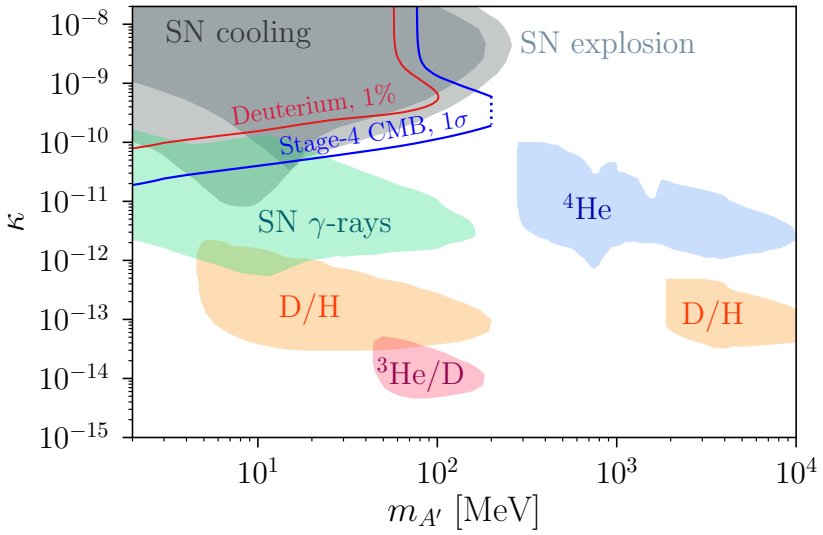

Figure 3.10. The color-shaded regions show existing bounds on dark photon mass and mixing parameters (as in figures 3.8 and 3.9). These bounds, obtained in previous studies, include: SN1987a cooling bound (dark grey) [49]; progenitor envelope bound from core-collapse SN (light grey) [158]; non-observation of γ-rays from SN1987a (green) [159]; and BBN bounds derived from photo-dissociation and neutron excess (orange, red, blue) [122]. (Note the D/H and ^{3}He/D bounds have been updated in Ref. [123].) Dark photon parameters lying along the blue line give deviations in $N_{\rm eff}$ which are $1\,\sigma_{\rm S4}$ (where the uncertainty is the CMB Stage-4 science book value, $1\,\sigma_{\rm S4} = 0.027$) below our baseline SC-calculated result with neutrino transport, $N_{\rm eff} = 3.044$. Likewise, the red line shows the dark photon parameters giving a 1% deviation of our calculated deuterium yield from our standard model and standard cosmology result, $10^5 \times ({\rm D/H})\,|_{\rm sc} = 2.64$. The blue dotted line denotes the location of the upper value of the dark photon mass range, $2\,{\rm MeV} \leq m_{A'} \leq 200\,{\rm MeV}$, studied in this work.

dark photons during weak decoupling. In that case, we can exclude the narrow range of the model parameter between the blue line and the light grey region (labeled as "SN explosion") from the dark photon model since that range of parameter space reduces the $N_{\rm eff}$ by more than $1\,\sigma_{\rm S4}$. As an alternative, suppose CMB Stage-4 experiments measure $N_{\rm eff}$ more than $1\,\sigma_{\rm S4}$ down from $N_{\rm eff} = 3.044$. In that case, it suggests there may be late decay of dark photons that cause the dilution of thermal neutrinos during the weak decoupling epoch.

The red line in figure 3.10 shows the deviation of the primordial deuterium abundance yield corresponding to a value of D/H that is down from our calculated standard model physics and standard cosmology value, $({\rm D/H})\,|_{\rm sc} = 2.64 \times 10^{-5}$, by an assumed 1% uncertainty,

i.e., $\sigma = 2.64 \times 10^{-7}$. This 1%-level determination of the primordial deuterium abundance has nearly been obtained via the observation of quasar absorption lines [160], which gives $(\mathrm{D/H})|_{\mathrm{obs}} = (2.527 \pm 0.030) \times 10^{-5}$. The mismatch of the deuterium abundance between our calculated standard model physics result and the measurement reported in Ref. [160] is due to the uncertainties in our nuclear reaction network which we do not claim as a source of tension. This source of uncertainty restricts us from making constraints on the model parameters with the absolute value of D/H. However, we project that uncertainties from the nuclear reaction network will be overcome in the near future (as discussed in section 3.3.4) and that the D/H from the standard model physics and standard cosmology calculation can eventually be directly compared to the observations. Under that assumption, we can make a *potential* bound by applying an assumed 1%-level uncertainty to the deuterium abundance yield in our calculation: for the model parameters circled by the red contour line (i.e., the region at the top-left portion of figure 3.10), the predicted primordial deuterium abundance with the indicated dark photon parameters is under-produced, that is, down by more than 1% from our standard model value. Hence, these dark photon parameters could be potentially ruled out.

We note that while our potential deuterium bound overlaps with the existing supernova bounds [49, 158], it is obtained from a self-consistent treatment of weak decoupling and BBN physics in the early universe environment. Therefore, our result provides a complementary verification of the supernova bounds derived from the stellar cooling argument.

In figure 3.10, we also show the existing constraints on the dark photon model as the various color-shaded regions. The dark grey region, labeled as "SN cooling", is the bound derived from the anomalous cooling of SN1987a due to the emission of dark photons [49]. The light grey region, labeled as "SN explosion", is the bound derived from the energy deposition in the progenitor stellar envelopes via emission of dark photons in the proto-neutron star core [158]. The green region shows the bound on the non-detection of gamma-rays, which are produced from the decaying dark photons in supernovae [159]. These are the dark photon bounds based on an energy argument; they show the constraints on dark photon model parameters for $m_{A'} \lesssim 100\,\mathrm{MeV}$.

Also included in figure 3.10 are the collected BBN bounds from Ref. [122] based on the photo-dissociation of light nuclei and the creation of a neutron excess; they are labeled as ^{4}He, ^{3}He/D and D/H.

3.4 Conclusion

Several conclusions can be drawn from the results of our calculations of dark photon production and decay in the early universe. First, our treatment of these dark photon processes allows for simultaneous, self-consistent calculation of electron-positron-photon-baryon and neutrino physics throughout the weak decoupling and BBN epochs. Dark photons decaying out of equilibrium during this extended period will inject entropy into the medium, leading to time-dependent dilution that modifies how temperature depends on time and expansion, and may modify charged current isospin-changing reactions and the neutron-to-proton ratio history as well. Any such alteration of the time-temperature-scale factor relation from the standard model prediction can result in a concomitant alteration in light element abundance yields and $N_{\rm eff}$. (Note, unlike Refs. [122, 123], we do not treat cascade nucleosynthesis but only thermal BBN, and therefore cannot constrain the effects of dark photon decays for temperatures $T < 10$ keV.) Exploiting this fact allows us to identify ranges of dark photon mass and couplings with standard model photons that are not currently constrained, but that may be subject to constraint, or probes, with future high precision cosmological data. In particular, CMB Stage-4 measurements promise significant improvements in the precision ($\sim 1\%$) with which the primordial helium abundance and $N_{\rm eff}$ can be measured. Likewise, the primordial deuterium abundance arguably is already known to high precision ($\sim 1\%$), and the advent of 30-m class telescopes promises to increase the confidence in this result.

Key uncertainties in BBN physics remain, for example, in the nuclear reaction rates associated with deuterium production and destruction, and in the effects of quantum kinetic evolution of neutrino flavor during weak decoupling [161]. Calculations of absolute light

element abundances and $N_{\rm eff}$ cannot yet attain the projected precision of the observational data. Consequently, we have presented here *deviations* of these quantities relative to our baseline standard model calculations for ranges of dark photon properties. In the end, our results suggest how to extend current limits on these, or even how to look for the "fingerprints" of dark photons. The latter would be patterns of deviations in deuterium, helium, and $N_{\rm eff}$ unique to particular ranges of dark photon mass and standard model coupling that are not otherwise constrained.

However, our calculations have revealed an issue which complicates high accuracy calculations of the effects of dark photon production and decay in the early universe. One set of calculations we did, the dark photon parameter survey calculations, are done self-consistently but with an assumption that the neutrino component is completely decoupled. However, neutrinos do not decouple abruptly at the beginning of the weak decoupling epoch, $\sim 10\,{\rm MeV}$. The process of out of equilibrium scattering of neutrinos on $e^{\pm}$-pairs continues to transfer entropy from the plasma into the decoupling neutrino seas, introducing small distortions in the relic neutrino energy spectra. This is a small effect in standard model cosmology, but can be bigger in non-standard ones. For a set of selected dark photon mass and coupling parameters we have performed fully self-consistent simulations that include full Boltzmann neutrino transport to capture the effects of out of equilibrium neutrino scattering.

As described above, the results of the full transport calculations are sobering. For some ranges of dark photon coupling and mass (the larger values in the ranges we consider) we find that transport can alter the calculated deviations in D/H and $N_{\rm eff}$ from our decoupled-neutrino estimates by of order the projected CMB measurement uncertainties in these quantities. This means that looking for the subtle fingerprints of dark photons (generally lower $N_{\rm eff}$ and D/H but no change in primordial helium) by comparing observational data with calculations will require that those calculations include full scattering-induced neutrino energy transport.

Probing a conjectured dark sector is an alluring prospect, but questions arise. How unique are the fingerprint signatures revealed by the calculations discussed above? Conceivably, a particle other than a dark photon could decay in a way that mimics the entropy injection and

dilution history that accompany the production and decay history of a dark photon. Moreover, we have assumed that the dark photon decay is entirely into standard model particles which instantly thermalize. What if the dark sector is rich enough in structure that the dark photon has decay branches into other, presumably lighter, dark sector particles? Were that the case, our calculations would be over-estimates of the entropy injection. Likewise, what if the dark photon, or other dark sector particle, decays during the weak decoupling epoch into standard model neutrinos? Again, entropy injection would be altered but could be tractable with the Boltzmann neutrino transport code described above.

In any case, the weak decoupling and BBN epochs and are promising laboratories for vetting new possibilities for dark sector and BSM physics. Future CMB and deuterium measurements may provide tantalizing clues about a putative dark sector. Here we have shown some of what must be done on the calculation side to translate those clues into insights into new physics.

3.5 Acknowledgments

We thank Susan Gardner and Tongyan Lin for valuable discussions. J. T. L. is supported by a Government Scholarship to Study Abroad from the Taiwan government. We acknowledge the N3AS NSF Hub, supported by NSF Grant No. PHY-1630782 and the Heising-Simons Foundation (2017-228). Additionally, we acknowledge NSF Grant No. PHY-1914242 at UCSD.

This chapter is, in full, a reprint of material from published work done in collaboration with George M. Fuller and Evan Grohs, as it appears in the Journal of Cosmology and Astroparticle Physics 12 (2020) 049. The dissertation author was the primary investigator and author of this material.

3.A Electromagnetic polarization tensor

In this appendix we review the calculation of the transverse and longitudinal photon polarization functions. Our discussion follows that in Refs. [133, 134].

For a photon field A_μ propagating in the z direction with the four-momentum $k^\mu = \left(k^0, \mathbf{k}\right) = (\omega, 0, 0, |\mathbf{k}|)$, we choose the basis vectors of the transverse ($\pm$T) and longitudinal polarization directions, respectively, as

$$\hat{e}^\mu_{\pm\mathrm{T}} = \frac{1}{\sqrt{2}}(0, 1, \pm i, 0), \tag{3.26}$$

$$\hat{e}^\mu_{\mathrm{L}} = \frac{|\mathbf{k}|}{\sqrt{\omega^2 - |\mathbf{k}|^2}}\left(1, 0, 0, \frac{\omega}{|\mathbf{k}|}\right). \tag{3.27}$$

Each basis vector is normalized, that is, $\hat{e}_a{}^\mu \hat{e}_{a\mu} = -1$ for $a = \pm$T or L. We parametrize the photon polarization tensor in an unmagnetized and isotropic plasma as

$$\Pi^{\mu\nu}(K) \equiv \sum_{a=\pm\mathrm{T},\mathrm{L}} \pi_a(\omega, \mathbf{k})\, \hat{e}^\mu_a \hat{e}^{*\nu}_a, \tag{3.28}$$

where π_T and π_L are transverse and longitudinal polarization functions, respectively. The leading order of $\Pi^{\mu\nu}$ is obtained by evaluating the one-loop photon self-energy insertion and taking the average over the fermion distributions. Approximating the momentum integral by evaluating it at the characteristic fermion velocity, $v_* \equiv \omega_1/\omega_\mathrm{p}$, the analytic forms for polarization functions to $\mathscr{O}(\alpha)$ can be approximated as

$$\pi_\mathrm{T}(\omega, \mathbf{k}) = \frac{3\omega_\mathrm{p}^2}{2v_*^2}\left(\frac{\omega^2}{|\mathbf{k}|^2} - \frac{\omega^2 - v_*^2|\mathbf{k}|^2}{|\mathbf{k}|^2}\frac{\omega}{2v_*|\mathbf{k}|}\ln\frac{\omega + v_*|\mathbf{k}|}{\omega - v_*|\mathbf{k}|}\right), \tag{3.29}$$

$$\pi_\mathrm{L}(\omega, \mathbf{k}) = \frac{3\omega_\mathrm{p}^2}{v_*^2}\left(\frac{\omega^2 - |\mathbf{k}|^2}{|\mathbf{k}|^2}\right)\left(\frac{\omega}{2v_*|\mathbf{k}|}\ln\frac{\omega + v_*|\mathbf{k}|}{\omega - v_*|\mathbf{k}|} - 1\right), \tag{3.30}$$

where

$$\omega_{\rm l}^2 \equiv \frac{4\alpha}{\pi}\int_0^\infty dp\frac{p^2}{E}\left(\frac{5}{3}v^2 - v^4\right)\left[f_l(E) + f_{\bar{l}}(E)\right], \tag{3.31}$$

$$\omega_{\rm p}^2 \equiv \frac{4\alpha}{\pi}\int_0^\infty dp\frac{p^2}{E}\left(1 - \frac{1}{3}v^2\right)\left[f_l(E) + f_{\bar{l}}(E)\right]. \tag{3.32}$$

With the conventions used in equations (3.27) and (3.30), the dispersion relation is written in the form $\omega^2 = |\mathbf{k}|^2 + \pi_a(\omega,\mathbf{k})$ for $a = \pm$T and L modes, and $\omega_{\rm p}$ is the plasma frequency. In these expressions, f_l and $f_{\bar{l}}$ are the lepton and anti-lepton occupation probabilities, respectively.

The electrons and positrons in equilibrium in the high entropy-per-baryon plasma of the early universe plasma are relativistic when $T \gg 1\,\text{MeV}$ and these particles have negligible chemical potentials (i.e., $T \gg |\mu_{e^+}|, |\mu_{e^-}|$). In this limit, all electrons and positrons have velocity $v = v_\star = 1$ and the plasma frequency is $\omega_{\rm p} = \sqrt{4\pi\alpha T^2/9}$.

In the limit of a non-relativistic and neutral electron-proton plasma (e.g., the plasma in the sun), the transverse and longitudinal photon polarization functions are given as

$$\pi_{\rm T}(\omega,\mathbf{k}) = \omega_{\rm p}^2\left(1 + v_{{\rm th},e}^2\frac{|\mathbf{k}|^2}{\omega^2}\right), \tag{3.33}$$

$$\pi_{\rm L}(\omega,\mathbf{k}) = \omega_{\rm p}^2\left(\frac{\omega^2 - |\mathbf{k}|^2}{|\mathbf{k}|^2}\right)\left(\frac{|\mathbf{k}|^2}{\omega^2} + 3v_{{\rm th},e}^2\frac{|\mathbf{k}|^4}{\omega^4}\right), \tag{3.34}$$

where $v_{{\rm th},e} \equiv \sqrt{T/m_e}$ is related to the electron thermal speed. The plasma frequency in this limit is $\omega_{\rm p} = \sqrt{4\pi\alpha n_e/m_e}$.

We note that another popular convention for the longitudinal basis vector is

$$\hat{e}_{\rm L}^{\mu} = \left(1, 0, 0, \frac{\omega}{|\mathbf{k}|}\right), \tag{3.35}$$

and its corresponding longitudinal polarization function takes the form

$$\pi_{\rm L}(\omega,\mathbf{k}) = \frac{3\omega_{\rm p}^2}{v_*^2}\left(\frac{\omega}{2v_*|\mathbf{k}|}\ln\frac{\omega + v_*|\mathbf{k}|}{\omega - v_*|\mathbf{k}|} - 1\right). \tag{3.36}$$

With this convention, the dispersion relation for the longitudinal mode is $|\mathbf{k}|^2 = \pi_{\mathrm{L}}$. However, throughout this paper we follow the convention used in equations (3.27) and (3.30).

3.B In-medium effect to dark photon couplings

The effective couplings of a massive dark photon depends strongly on the properties of SM photon polarization in the dense medium. In this appendix we review the in-medium Lagrangian and the conditions required for resonant dark photon emission [162].

The self energy of the photon field A^μ in a dense medium is described by including an additional potential term $-\frac{1}{2}A_\mu \Pi^{\mu\nu} A_\nu$ in the vacuum Lagrangian in equation (3.1). After making a field redefinition $A_\mu \to A_\mu + \kappa A'_\mu$ to rotate away the kinetic mixing term, the in-medium Lagrangian of the relevant terms to $\mathcal{O}(\kappa)$ becomes

$$\mathscr{L}_{\mathrm{IM}} \supset -\frac{1}{4}F_{\mu\nu}F^{\mu\nu} - \frac{1}{4}F'_{\mu\nu}F'^{\mu\nu} + \frac{1}{2}{m_{A'}}^2 A'_\mu A'^\mu - \frac{1}{2}A_\mu \Pi^{\mu\nu} A_\nu - \kappa A_\mu \Pi^{\mu\nu} A'_\nu + e(A_\mu + \kappa A'_\mu) J^\mu_{\mathrm{em}}. \tag{3.37}$$

Next, we project the photon and dark photon fields onto transverse ($\pm$T) and longitudinal (L) directions and consider only one polarization at a time. This can be done by decomposing a given vector field V^μ into its three polarization states as

$$V^\mu = \sum_{a=\pm\mathrm{T},\mathrm{L}} V_a \hat{e}^\mu_a \equiv \sum_{a=\pm\mathrm{T},\mathrm{L}} V^\mu_a, \tag{3.38}$$

where again each basis vector satisfies $\hat{e}_a{}^\mu \hat{e}_{a,\mu} = -1$. As a result, the in-medium Lagrangian of one given single polarization state a is

$$\begin{aligned}\mathscr{L}_{\mathrm{IM},a} \supset & -\frac{1}{4}F_{a,\mu\nu}F_a^{\mu\nu} - \frac{1}{4}F'_{a,\mu\nu}F'^{\mu\nu}_a + \frac{1}{2}{m_{A'}}^2 A'_{a,\mu}A'^\mu_a \\ & + \frac{1}{2}\pi_a A_{a,\nu}A^\nu_a + \kappa\pi_a A_{a,\mu}A'^\mu_a + e(A_{a,\mu} + \kappa A'_{a,\mu})J^\mu_{\mathrm{em}}.\end{aligned} \tag{3.39}$$

The mixing between the photon and dark photon fields can be rotated away by making another

field redefinition,

$$\begin{aligned} A_{a,\mu} &= \tilde{A}_{a,\mu} + \frac{\kappa\pi_a}{m_{A'}^2 - \pi_a}\tilde{A}'_{a,\mu}, \\ A'_{a,\mu} &= \tilde{A}'_{a,\mu} - \frac{\kappa\pi_a}{m_{A'}^2 - \pi_a}\tilde{A}_{a,\mu}. \end{aligned} \tag{3.40}$$

Eventually, we arrive at the in-medium Lagrangian of the polarization state a presented in the mass basis as[1]

$$\begin{aligned} \mathscr{L}_{\mathrm{IM},a} \supset &-\frac{1}{4}\tilde{F}_{a,\mu\nu}\tilde{F}_a^{\mu\nu} - \frac{1}{4}\tilde{F}'_{a,\mu\nu}\tilde{F}'^{\mu\nu}_a + \frac{1}{2}{m_{A'}}^2\tilde{A}'_{a,\mu}\tilde{A}'^{\mu}_a \\ &+ \frac{1}{2}\pi_a\tilde{A}_{a,\nu}\tilde{A}^{\nu}_a + e\left(\tilde{A}_{a,\mu} + \frac{\kappa m_{A'}^2}{m_{A'}^2 - \pi_a}\tilde{A}'_{a,\mu}\right)J^{\mu}_{\mathrm{em}}. \end{aligned} \tag{3.41}$$

It is clear from equation (3.41) that the effective coupling between $\tilde{A}'_a$ and J_{em} is

$$e\kappa_{\mathrm{eff},a} = \frac{e\kappa{m_{A'}}^2}{\sqrt{\left({m_{A'}}^2 - \mathrm{Re}\,\pi_a\right)^2 + \left(\mathrm{Im}\,\pi_a\right)^2}}, \tag{3.42}$$

and the dark photon emission rate will be enhanced when $\mathrm{Re}\,\pi_a$ approaches ${m_{A'}}^2$.

3.B.1 Example: resonant dark photon emission in a nonrelativistic plasma

References [48, 108, 112] have pointed out the importance of plasma effects in the dark photon emission rate in the sun and in horizontal branch stars when $m_{A'} < 10\,\mathrm{eV}$. Here we use the plasma dispersion relation to interpret these results.

In compact objects, the electron plasma frequency is many orders of magnitude higher than electron cyclotron frequency. As far as the ordinary electromagnetic (transverse) and electrostatic (longitudinal) modes are concerned, the plasma in such conditions can be treated as unmagnetized and isotropic. A SM photon propagating in this environment would then acquire an effective in-medium mass, $\mathrm{Re}\,\pi_a$, where the general form of π_a is given in equations (3.29) and (3.30). With the presence of a dark photon with mass $m_{A'}$, dark photon resonant emission occurs

[1] We note that the form of effective kinetic mixing presented in equation (3.41) works for all three polarization states since they satisfy the same form of normalization, $\hat{e}^{\mu}_a\hat{e}_{a,\mu} = -1$.

when ${m_{A'}}^2 = \mathrm{Re}\,\pi_a$. This statement is equivalent to saying that the resonance happens when there is a solution of $(\omega, \mathbf{k})$ that satisfies both the dispersion relations for the dark photon, $\omega^2 = |\mathbf{k}|^2 + m_{A'}^2$, and for in-medium SM photons, $\omega^2 = |\mathbf{k}|^2 + \mathrm{Re}\,\pi_a(\omega, \mathbf{k})$. While these two dispersion relations are similar in structure, they dictate quite different behavior in a nonrelativistic plasma such as that in the sun or in horizontal branch stars.

In figure 3.11, we take the sun as an example of the nonrelativistic plasma environment and show the dispersion relations for in-medium photons and for a dark photon. We consider a range of radius r from the center of the sun to 95% of the solar radius, $r \leq 0.95\,R_\odot$. Electrons and protons in the sun are nonrelativistic. The dispersion relation for longitudinal EM oscillation in such an environment is $\omega \approx \omega_\mathrm{p}$ when $|\mathbf{k}| \lesssim 1/\lambda_\mathrm{D}$, where λ_D denotes Debye screening length. This behavior is evident for the solid lines in the left plot of figure 3.11. When $m_{A'}$ is less than the plasma frequency at around the edge of the sun, $\omega_\mathrm{p}|_{r=0.95R_\odot} \sim 1\,\mathrm{eV}$, the dispersion relation curve for the longitudinal EM oscillation may cross the dispersion relation curve for the dark photon at any given radius. That is, nearly the entire sun could radiate longitudinal dark photons resonantly. On the other hand, the transverse dark photon dispersion relation curve never intersects the dark photon dispersion relation curve, as is evident in the right plot of figure 3.11.

3.C Dark photon emission rate

In this appendix, we calculate the lepton-pair annihilation rate and the relevant corresponding matrix elements. Here we follow the discussion of this physics in appendix B of Ref. [122].

The $\Gamma^\mathrm{prod}_{A_a}$ shown in equation (3.4) is the annihilation rate for the processes $l\bar{l} \to A_a$ or $q\bar{q} \to A_a$. In the following, we take the lepton-pair annihilation case as an example. Denoting p and q as the four-momenta of two annihilating leptons, and $k = p + q$ as the four-momentum for

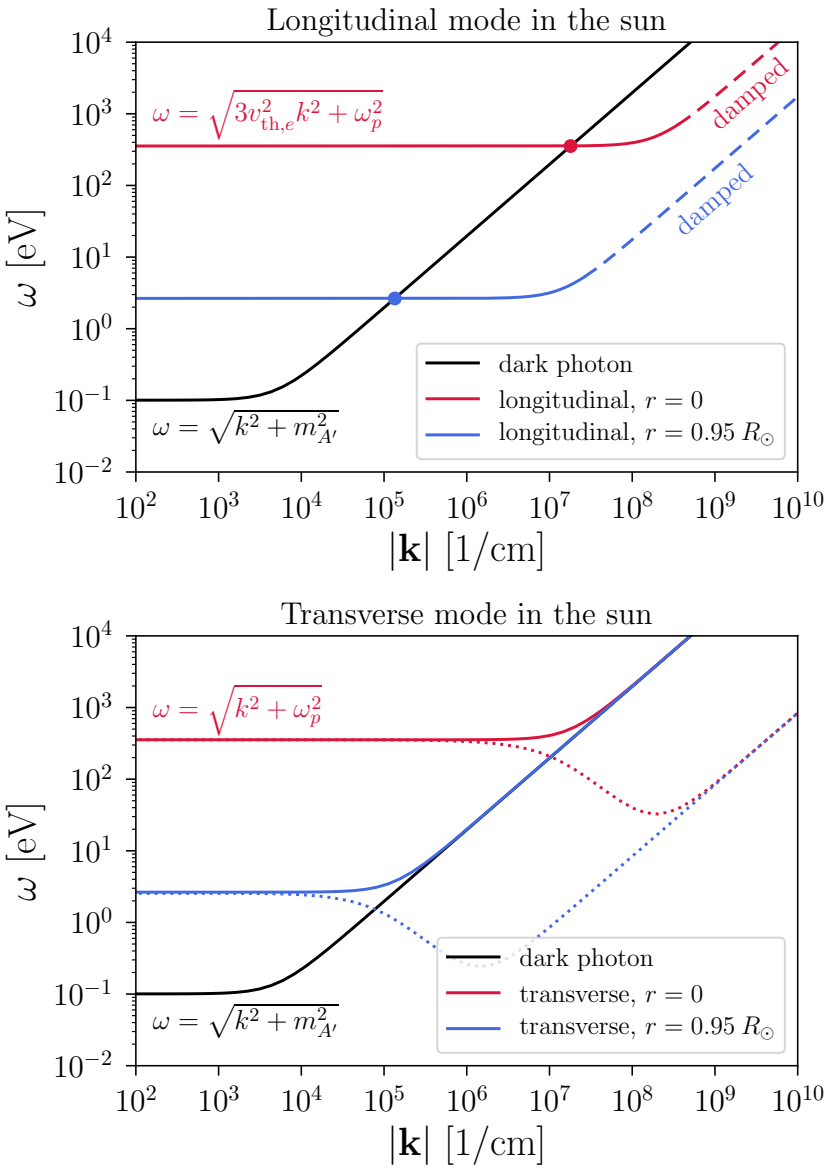

Figure 3.11. Dispersion relations for the transverse (**bottom**) and longitudinal (**top**) modes of SM photons in the sun. (**top**) The red and blue solid curves denote the dispersion relations of the longitudinal mode at the center and at the edge of the sun, respectively. The black curve shows the dispersion relation for a dark photon in a model with $m_{A'} = 10^{-1}$ eV. Dark photon resonant emission can occur when the SM photon longitudinal dispersion curve intersects the dark photon dispersion curve. This can happen for the range of $|\mathbf{k}|$ values bounded between the intersection points (circles) on the red and blue curves. We note that the longitudinal plasma wave for $|\mathbf{k}| \gtrsim 1/\lambda_{\mathrm{D}}$ in a nonrelativistic plasma suffers strong Landau damping as shown by the dashed lines. (**bottom**) The colored solid curves denote the dispersion relations for the transverse mode in the sun. The red (blue) dotted curve is the difference between red (blue) solid curve and the black dark photon curve for each $|\mathbf{k}|$ value. The dispersion relation curve for SM photons in the transverse mode never intersects the dispersion relation curve for a dark photon.

A_a, the annihilation rate for the process $l\bar{l} \to A_a$ is

$$\begin{aligned}\Gamma^{\text{prod}}_{A_a}(\omega) &= \frac{1}{2\omega}\int \frac{d^3\mathbf{p}}{(2\pi)^3 2E_{\mathbf{p}}}\frac{d^3\mathbf{q}}{(2\pi)^3 2E_{\mathbf{q}}}(2\pi)^4\,\delta^{(4)}(k-p-q)\,f_l(E_{\mathbf{p}})\,f_{\bar{l}}(E_{\mathbf{q}})\left|\mathscr{M}_{l\bar{l}\to A_a}\right|^2 \\ &= \frac{1}{16\pi\omega}\int \frac{|\mathbf{p}|^2 d|\mathbf{p}|\,d\cos\theta}{E_{\mathbf{p}}E_{\mathbf{q}}}\,f_l(E_{\mathbf{p}})\,f_{\bar{l}}(E_{\mathbf{q}})\;\delta(\omega-E_{\mathbf{p}}-E_{\mathbf{q}})\;\left|\mathscr{M}_{l\bar{l}\to A_a}\right|^2,\end{aligned} \tag{3.43}$$

where θ denotes the angle between the three-vectors $\mathbf{k}$ and $\mathbf{p}$. Using the identity $\delta(g(x)) = \sum_i \delta(x-x_i)/|g'(x_i)|$, we write the Dirac delta function shown in equation (3.43) as

$$\delta(\omega-E_{\mathbf{p}}-E_{\mathbf{q}}) = \sum_i \delta(\cos\theta-\cos\theta_i)\Bigg/\left|\frac{|\mathbf{p}||\mathbf{k}|}{\sqrt{m_l^2+|\mathbf{p}|^2+|\mathbf{k}|^2-2|\mathbf{p}||\mathbf{k}|\cos\theta_i}}\right|, \tag{3.44}$$

where $\cos\theta_i = \frac{2\omega E_{\mathbf{p}} - {m_{A'}}^2}{2|\mathbf{p}||\mathbf{k}|}$. Since $\cos^2\theta_i \leq 1$, we obtain the maximum and minimum values of $E_{\mathbf{p}}$,

$$E_{\mathbf{p},\max} = \frac{\omega}{2}+\frac{|\mathbf{k}|}{2}\sqrt{1-4\frac{{m_l}^2}{{m_{A'}}^2}},\ \text{and}\quad E_{\mathbf{p},\min} = \frac{\omega}{2}-\frac{|\mathbf{k}|}{2}\sqrt{1-4\frac{{m_l}^2}{{m_{A'}}^2}}. \tag{3.45}$$

(Note that $E_{\mathbf{p},\min} \geq m_e$.) Integrated over θ, the annihilation rate for lepton pairs in equation (3.43) becomes

$$\Gamma^{\text{prod}}_{A_a}(\omega) = \frac{1}{16\pi\omega|\mathbf{k}|}\int_{E_{\mathbf{p},\min}}^{E_{\mathbf{p},\max}} dE_{\mathbf{p}}\;f_l(E_{\mathbf{p}})\,f_{\bar{l}}(\omega-E_{\mathbf{p}})\left|\mathscr{M}_{l\bar{l}\to A_a}\right|^2. \tag{3.46}$$

The calculation of the annihilation rate for free quarks-pairs is the same as the above calculation for the annihilation rate of lepton-pairs.

The effective coupling of A'_a to J^μ_{em} shown in equation (3.2) indicates that the dark photon emission rate, $\Gamma^{\text{prod}}_{A'_a}$, is a factor κ_{eff} smaller than $\Gamma^{\text{prod}}_{A_a}$. As a result, the *integrated* dark photon emission rate in a dense medium is given by

$$\bar{\Gamma}^{\text{prod}}_{A'_a} = \int \frac{d^3\mathbf{k}}{(2\pi)^3}\;\kappa^2_{\text{eff},a}\,\Gamma^{\text{prod}}_{A_a}(\omega). \tag{3.47}$$

The matrix element in equation (3.46) is

$$\mathscr{M}_{l\bar{l}\to A_a} = \bar{v}\left(p_l\right)\left(-ie\gamma^\mu\right)u\left(q_{\bar{l}}\right)\varepsilon^*_{a,\mu}\left(k\right), \tag{3.48}$$

where ε_a^μ is the external polarization state of photon A^μ. The squared matrix element for the transverse mode is evaluated by summing over the initial lepton spin states and the two final transverse photon states. This gives

$$\begin{aligned}\sum_{l\bar{l}\text{ spins},\,\pm\mathrm{T}}\left|\mathscr{M}_{l\bar{l}\to A_{\pm\mathrm{T}}}\right|^2 &= 4e^2\,\mathrm{Tr}\left[\left(\not{q}-m\right)\gamma^\mu\left(\not{p}+m\right)\gamma^\nu\right](0,1,1,0)_{\mu\nu,\,\mathrm{diag}}\\ &= 16\pi\alpha\left({m_{A'}}^2-2|\mathbf{p}|^2\sin^2\theta\right).\end{aligned} \tag{3.49}$$

The squared matrix element for longitudinal mode is evaluated by summing over initial lepton spin states. This gives

$$\begin{aligned}\sum_{l\bar{l}\text{ spins}}\left|\mathscr{M}_{l\bar{l}\to A_\mathrm{L}}\right|^2 &= 4e^2\,\mathrm{Tr}\left[\left(\not{q}-m\right)\gamma^\mu\left(\not{p}+m\right)\gamma^\nu\right]\begin{pmatrix}k^2 & 0 & 0 & -\omega k\\ 0 & 0 & 0 & 0\\ 0 & 0 & 0 & 0\\ -\omega k & 0 & 0 & \omega^2\end{pmatrix}_{\mu\nu}\\ &= 16\pi\alpha\left[\frac{1}{2}{m_{A'}}^2-\frac{2}{{m_{A'}}^2}\left(|\mathbf{k}|E_\mathbf{p}-\omega|\mathbf{p}|\cos\theta\right)^2\right].\end{aligned} \tag{3.50}$$

Chapter 4

Dynamics of millicharged dark matter in supernova remnants

Dark matter could have a small electromagnetic charge, provided the charge-to-mass ratio is much less than that of electrons or protons. This candidate, commonly known as millicharged dark matter (mDM), would form a plasma and interact with the interstellar medium and electromagnetic fields within galaxies. In general, understanding the dynamics of mDM requires consideration of collective plasma effects. It has been proposed that mDM can be accelerated in supernova remnants, forming a dark cosmic ray population that would leave distinct experimental signatures. In this work, we study a microphysical model where mDM is shocked by a supernova remnant and isotropized in the frame of the expanding fluid. We find that for $|q_\chi/m_\chi| \gtrsim 10^{-13}e/\text{MeV}$, the isotropization length for electromagnetic plasma instabilities is much shorter than the size of the supernova remnant. This is a necessary, though not sufficient, first step for formation of a Fermi-accelerated mDM component, and determining the size of this component requires further study. We discuss additional implications of mDM interactions in supernova remnants.

4.1 Introduction

An important open question is whether dark matter (DM) has nongravitational interactions with Standard Model (SM) particles. In traditionally favored classes of DM candidates such as

the WIMP, axion, or sterile neutrino, the DM typically has short-range interactions with the SM through mediators at the weak scale (or heavier). Such candidates and interactions are being actively searched for in indirect detection, direct detection and collider experiments.

If DM has long-range electromagnetic (EM) interactions with the SM, there can be dramatic effects on astrophysical and cosmological scales. Consider particle DM that has mass m_χ and a small electromagnetic charge $|q_\chi|$, with equal parts $+q_\chi$ and $-q_\chi$ components. We will refer to this candidate by the often-used nomenclature of millicharged DM (mDM), although possible values of $|q_\chi|$ range many orders of magnitude.[1] For sufficiently small charge-to-mass ratios interactions, this DM candidate could have been undetected thus far. For instance, there are strong bounds from considering the scattering of mDM with the ionized plasma in the early universe, which leads to damping in the CMB anisotropies and matter power spectrum [165–167]. Current bounds [168–170] require that $|q_\chi|/e \lesssim 10^{-6}(m_\chi/\mathrm{GeV})^{1/2}$, assuming DM mass m_χ below a GeV and that this candidate forms 100% of the observed relic abundance.

Given such stringent constraints, what motivates our interest on the possibility of DM with fractional charge? First, it provides a simple model where the DM relic abundance can be obtained through only EM interactions. For charges $|q_\chi/e| \sim 10^{-11} - 10^{-10}$ it is possible to obtain the observed relic abundance through freeze-in [171, 172], where the DM is never in thermal equilibrium with the SM thermal bath. (Note the constraints on $|q_\chi|$ exclude the possibility that 100% of the DM came from thermal freeze-out of mDM.) This small fractional electric charge could be generated if DM has a small fractional hypercharge, or if the DM is charged under a nearly massless dark photon which has a kinetic mixing with the SM photon (see for example Ref. [173]).

The key idea is that even with such tiny charges, long-range EM interactions can give rise to observable signatures in experiments or in astrophysical environments. For instance, mDM has sizeable scattering rates in direct detection experiments, particularly through DM-electron

[1] A DM candidate which is much heavier than the proton and where $|q_\chi|/e$ is an $\mathcal{O}(1)$ number is more often referred to as a charged massive particle (CHAMP) [163, 164].

scattering [174]. Because the long-range interactions are enhanced for low momentum transfer scattering, a low-threshold experiment could probe values of $|q_\chi|$ where mDM is produced by freeze-in (or even smaller $|q_\chi|$). Direct detection experiments are now employing newly developed methods and technologies to search for this candidate and closely related models [175].

In addition, mDM has been of interest following the reported observation of an anomalous absorption in radio frequencies by the EDGES collaboration [52]. The observation has been interpreted as a 21cm absorption trough due to DM-baryon scattering at cosmic dawn; since DM is typically much colder than baryons at these redshifts, this would cool the baryons relative to the CMB. Investigations have focused on a long-range Rutherford-type interaction such as that from mDM, since the scattering is larger at late times [53, 176–178]. For mDM comprising 100% of the relic abundance, CMB bounds exclude the required charges to match the EDGES observation; however, there remain viable scenarios where mDM is only a fraction of the total DM [168, 179].

While the signatures discussed thus far focus on particle-particle interactions of mDM, the implications may be even more striking if we account for wave-particle interactions of mDM in galactic EM fields. Because of the tiny charges, mDM generally is not found in bound states and instead forms a dark plasma. In supernova remnants (SNR), this dark plasma can interact with the shock front and it has been suggested [164, 180] that there is an mDM component that undergoes diffusive shock acceleration (DSA), also known as first-order Fermi acceleration [181, 182]. Implicit in this scenario is the assumption that mDM efficiently scatters against the turbulent magnetic fields generated in a SNR. If this is the case, it was argued that the accelerated mDM is evacuated from the disk [180] (which would hinder their detection on Earth) or alternatively that there is a flux of the accelerated component at Earth [183, 184] (which would aid in their detection). Mergers of mDM halos could result in the formation of collisionless shocks through plasma instabilities, which would impact galaxy formation as well as observations of cluster mergers such as the Bullet cluster; a related scenario where DM has long-range dark photon interactions was studied in Refs. [185, 186]. Finally, it has

also been pointed out that the interactions of halo mDM passing through the magnetic field of the Milky Way disk would lead to angular momentum exchange and result in spin-down of the disk [187]. Clearly, understanding such signatures and possible constraints is needed to determine the viability and detectability of mDM as a DM candidate.

Our goal is to study the consequences of the long-range electromagnetic interactions of mDM in the environment of supernova remnants. Specifically, in this work we will determine the mDM parameter space where mDM can be swept up by SNR and discuss possible implications. Previous work assumed that mDM can efficiently undergo DSA in remnants similar to proton cosmic rays (CR) [180, 183, 184], but did not provide a microphysical justification or model. In fact, there are a number of stages for mDM dynamics in the SNR before they could be considered as undergoing DSA. The interaction of mDM with shocked ISM gas is a first necessary step, whereby the ambient mDM is swept up to $3/4$ of the shock speed and isotropized in the frame of the expanding fluid. Our approach is to develop a microphysical model for this process, where we can analyze the sweep-up timescale in the linear regime.

The basic idea is the following: viewed from the frame of the expanding SNR, the mDM plasma has a large bulk velocity and free energy, a configuration which is unstable to the generation of EM fields. If the growth times for these plasma instabilities are sufficiently fast, the bulk motion of the mDM is slowed down and it can become isotropized in the expanding remnant. Note that we will focus on the dynamics of the *bulk* of the mDM. After the mDM is swept up by the SNR, it is possible that a small fraction of the mDM could cross the shock front multiple times and start the DSA process. However, obtaining a robust quantitative prediction for the fraction and spectrum of accelerated mDM requires additional techniques beyond the scope of this work.

A summary of the main results can be found in the remainder of this introduction. In Sec. 4.2, we provide a review of supernova shock waves and acceleration of proton cosmic rays, make a comparison for mDM, and describe the plasma instabilities that we analyze. The detailed numerical results for the growth times are covered in Sec. 4.3 for electrostatic instabilities and

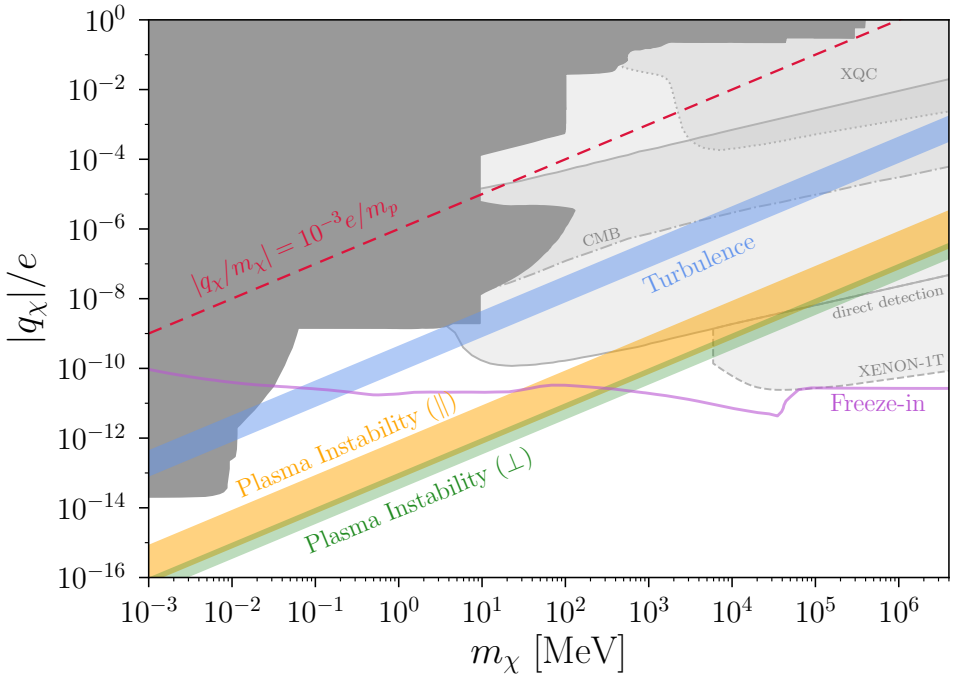

Figure 4.1. In this work, we only consider the parameter space below the red dashed line where $|q_\chi|/m_\chi < 10^{-3}(e/m_p)$. Above the colored bands, the mDM charge fraction $|q_\chi/e|$ is sufficiently large for it to be swept up by the SNR. The blue band gives the minimum $|q_\chi/e|$ for mDM diffusion due to CR proton-driven turbulence in a quasiparallel shock. Above the orange and green bands, there are mDM-driven plasma instabilities in parallel ($\parallel$) and perpendicular ($\perp$) shocks, respectively. The upper (lower) boundary of each band is for shock velocity $v_{\rm sh} = 1500$ km/s (300 km/s). The dark gray shaded region combines bounds on production of mDM in accelerator experiments [188–191], in stars [192, 193], in SN1987a [194], and during BBN [192, 195, 196]. The lighter shaded regions are reported direct constraints on mDM that assume standard density and velocity distributions, which may be impacted by mDM wave-particle interactions. These include combined direct detection bounds [50, 51], from XQC [197], and from CMB bounds on DM-baryon scattering [169].

in Sec. 4.4 for electromagnetic instabilities. We then discuss some consequences for the mDM distribution in the Milky Way and for the evolution of SNRs in Sec. 4.5, and conclude in Sec. 4.6. Appendix 4.A briefly reviews the derivation of the linear response and growth rates in a plasma.

4.1.1 Summary of results

The main result of this work is illustrated in Fig. 4.1. We have assumed here that mDM is 100% of the total DM relic abundance. We will only consider the parameter space below the red

dashed line, where the mDM charge-to-mass ratio is at least 10^3 times smaller than that of the proton, $|q_\chi|/m_\chi < 10^{-3}(e/m_p)$. Under this condition, the mDM Larmor frequency is at least 10^3 times smaller than the proton Larmor frequency, so we can safely assume that mDM crosses the supernova shock front undeflected and that mDM does not change the dispersion relation of existing plasma waves in the Milky Way at a noticeable level. Our conclusions are:

1. For quasiparallel shocks (i.e., the angle between ambient magnetic field and shock normal is less than 45°) and $|q_\chi|/m_\chi$ above the blue band, it is possible for mDM to undergo pitch-angle scattering off CR-driven turbulent magnetic fields. As discussed in Sec. 4.2.2, this is possible when the mDM Larmor radius does not exceed the maximum wavelength of CR-driven turbulence. A fraction of mDM particles might undergo Fermi acceleration by repeated scattering off the CR-driven turbulence upstream and downstream of the shock.

2. For quasiparallel shocks and $|q_\chi|/e$ between the blue and orange bands, there is a mDM-driven plasma instability. In this region, the mDM Larmor radius is sufficiently large that we approximate the magnetic fields as uniform. Then there is a plasma instability due to the large relative motion of the mDM and the expanding ionized fluid, which will act to reduce that relative velocity. In this part of the parameter space, the growth of the instability is sufficiently fast such that it saturates within one tenth of the SNR radius, and we treat the mDM as being effectively isotropized. A fraction of mDM particles could undergo Fermi acceleration by scattering off the mDM-driven turbulence.

3. For quasiperpendicular shocks, there is no Fermi acceleration of mDM. Similar to CR protons, the mDM cannot cross the shock multiple times in this case. However, above the green band, there is still a mDM-driven instability which affects the bulk dynamics of the mDM.

While the strength of the plasma instability depends on the density of mDM and shock properties, roughly speaking the growth rate can be approximated by the Larmor frequency

Ω_χ. The condition that the instability saturates within the SNR can therefore heuristically be given as $v_{\rm sh}/\Omega_\chi \ll R_{\rm sh}$, where $R_{\rm sh}$ and $v_{\rm sh}$ are the shock radius and velocity, respectively. This can be rewritten as the condition that the mDM Larmor radius is much smaller than the shock size, $r_{{\rm L},\chi} \ll R_{\rm sh}$, in agreement with naïve expectation. Our analysis demonstrates this condition robustly and takes into account the dependence of the instability on shock properties and ambient mDM density. In comparison to the wave-particle interactions, we note that everywhere below the red dashed line, i.e., $|q_\chi|/m_\chi < 10^{-3}(e/m_p)$, the mDM trajectory in the SNR would not be significantly altered by particle-particle Coulomb interactions. We can see this by writing the mean free path (mfp) of mDM-proton Coulomb scattering in the SNR [198],

$$\text{mfp} = \frac{m_\chi^2 V_0^4}{8\pi n_i q_\chi^2 e^2 \ln\Lambda} \approx 8100 \text{ pc} \left(\frac{10^{-3}}{\Omega_\chi/\Omega_i}\right)^2 \left(\frac{v_{\rm sh}}{300 \text{ km/s}}\right)^4 \left(\frac{1 \text{ cm}^{-3}}{n_i}\right) \left(\frac{25}{\ln\Lambda}\right), \qquad (4.1)$$

where $V_0 = 3v_{\rm sh}/4$ is the relative velocity between DM and shocked ISM, n_i is the proton number density, and $\ln\Lambda$ is the Coulomb logarithm. This is much larger than the maximum SNR radius, which is $\lesssim 100$ pc.

The darker gray shaded regions in Fig. 4.1 show collected bounds on production of mDM, which do not make any assumption on its relic density. There are bounds on emission of mDM in stars, which would lead to anomalous cooling; we show limits from horizontal branch, white dwarf, and red giant stars for $m_\chi \lesssim 100$ keV [192, 193] and from SN1987a for $m_\chi \lesssim 100$ MeV [194]. For $m_\chi \lesssim$ MeV, mDM can thermalize with the SM thermal bath, leading to changes in BBN abundances and the effective number of light degrees of freedom; these bounds come from Refs. [192, 195]. Also included are collected accelerator bounds [188–191]. The lighter shaded regions show constraints which make an assumption on the mDM density and/or velocity distribution. We show bounds assuming mDM is 100% of the DM content from direct detection [50], searches for charged DM with the XQC satellite [197], and the effect of DM-baryon scattering on the CMB [169]. The solid line gives values of $|q_\chi|/e$ where 100% of the DM relic abundance is comprised of mDM that is produced through freeze-in [171, 172];

values below this line lead to mDM that is a fractional component of DM, while larger $|q_\chi|/e$ requires additional interactions beyond EM.

Finally, in this paper we focus on a fermion mDM candidate with only EM interactions. As mentioned above, there are also models that generate the millicharge via a kinetically-mixed dark photon. DM interactions with the dark photon can lead to phenomenological differences in constraints and DM interactions with charged SM particles. This possibility deserves study, but will not be considered any more here.

4.2 Proton vs. millicharged dark matter dynamics in a supernova collisionless shock

In this section, we will overview the interaction between the supernova ejecta and the interstellar medium (ISM) and explain how mDM interacts differently with the supernova shock compared to the case of ISM gas. We will lay out the motivation and strategy for the plasma instabilities which we study in detail in Sec. 4.3 and 4.4. Throughout this work, "ion" refers to "proton" unless otherwise specified.

4.2.1 The visible sector: Protons and the supernova shock

A supernova explosion is one of the most violent events in galaxies. A typical Type Ia supernova can expel 1 $M_\odot$ ejecta with kinetic energy $\approx 10^{51}$ erg (i.e., with initial speed $\sim 10^4$ km/s).[2] Because the pressure in the ejecta is significantly higher than the pressure in the ambient interstellar medium, the ejecta will propel a shock wave to the ambient ISM. The ordinary matter bounded by this expanding shock wave–the ejecta from the explosion and the interstellar material swept up by the shock wave–is referred to as the *supernova remnant*. As the interstellar gas is swept up by the shock, entropy is generated and the ordered bulk kinetic energy of the gas in front of the shock is converted to thermal energy.

[2]Type II core-collapse supernova can expel $10-20\ M_\odot$ debris with kinetic energy as high as 10^{52} erg. For simplicity, we only consider Type Ia events in this work as a representative case.

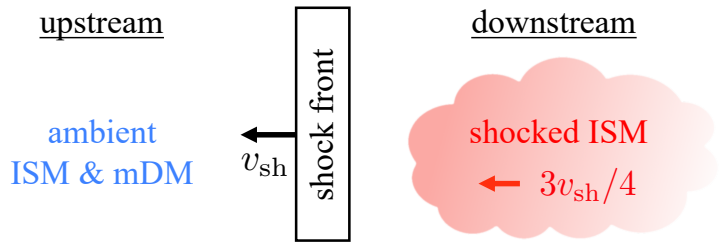

Figure 4.2. Schematic diagram for a supernova shock wave propagating in the interstellar medium (ISM). Just behind the shock front, the ISM has been shocked and moves at $3/4$ of the shock speed, whereas the mDM gas is at rest. The relative motion between the shocked ISM and the unshocked mDM provides the free energy to drive a plasma instability. If the instabilities occur, the mDM will be isotropized in the frame of the shocked ISM gas and be swept up by the expanding supernova remnant.

Figure 4.2 is a schematic representation of a shock wave. The cooler, unshocked region ahead of the shock front is called *upstream* and the hotter, shocked region is called *downstream*. The shock transition zone is where the dissipation happens, and it requires the particle velocity distribution be isotropized in the downstream frame. We can determine the downstream fluid speed, density, and temperature from the Rankine-Hugoniot (RH) jump conditions, which relate the upstream and downstream states assuming the conservation of mass, momentum and energy in an one-dimensional flow. For a high Mach shock wave propagating in the monatomic gas, the downstream fluid speed in the frame of the background ISM is $3/4$ of the shock speed $v_{\rm sh}$. The number density and the magnetic fields of the shocked gas in the downstream are 4 times the number density and the magnetic fields in the upstream.

As for the downstream temperature, we take a somewhat more realistic case. Including helium, with a ratio of helium number density to hydrogen number density of 0.1, the downstream ion temperature is $T_{2i} \approx 3\mu v_{\rm sh}^2/16$, where $\mu = 1.27 m_p$ denotes the mean mass per ion (Hydrogen and Helium nuclei) and m_p is the proton mass. Thus, the proton thermal speed in the downstream is $v_{{\rm th},i} \equiv \sqrt{2T_{2i}/m_p} \approx 0.69 v_{\rm sh}$. We note that electrons have different temperature from ions just behind the shock front. This is because the ion-ion and electron-electron Coulomb scattering only leads ions and electrons to each relax to their own Maxwellian velocity distributions. The ion-electron relaxation time is much greater than ion-ion and electron-electron relaxation times, so

the final temperature equilibration between ions and electrons happens at the deeper downstream.

Our discussion thus far requires the kinetic energy of the upstream ISM bulk flow to be converted into heat at the shock transition zone. For a supernova shock in interstellar space, it is collective plasma effects involving ions and plasma waves at the shock transition zone that cause the dissipation of the incoming ISM flow. This type of shock is referred to as a *collisionless shock* [199–201]. The formation and structure of the collisionless shock is complex as it involves several types of plasma instabilities and compression of the magnetic fields at the shock front. But in a broad brush, the collective plasma waves come from instabilities excited by a fraction of the ions reflected at the shock front. The thickness of the supernova collisionless shock is approximately a few ion Larmor radii, though it could be much larger if the ambient magnetic field is parallel to the shock normal [199].

In the following, we briefly review the evolution of supernova shocks and the generation of cosmic-ray protons. These will be important to understand the amount of mDM that can be affected by the shocks as well as the strength of preexisting turbulence in the downstream fluid.

A brief history of a supernova remnant

In the early evolution of the supernova remnant, the shock wave propagates radially outward along with the supersonic ejecta at nearly constant speed, $\sim 10^4$ km/s. This stage is called the *free-expansion phase*. As the shock wave sweeps up more and more ambient gas, the swept-up mass eventually exceeds the ejecta mass and begins to govern the shock wave dynamics. Taking the number density of molecules in the ISM as 0.25 cm^{-3}, this happens about ~ 330 years after the explosion.

Subsequently, the shock starts to slow down, and the kinetic energy of the ejecta is transferred to the shocked matter. The shock now enters the *Sedov-Taylor phase*. During this stage, the shock velocity and the distance it has traveled at time t after the explosion are governed by the initial kinetic energy of the ejecta, $E_{\rm SN}$, and the mass density of the swept-up gas, $\rho_{\rm ISM}$. Without considering the radiative losses and ambient gas pressure, the variables t,

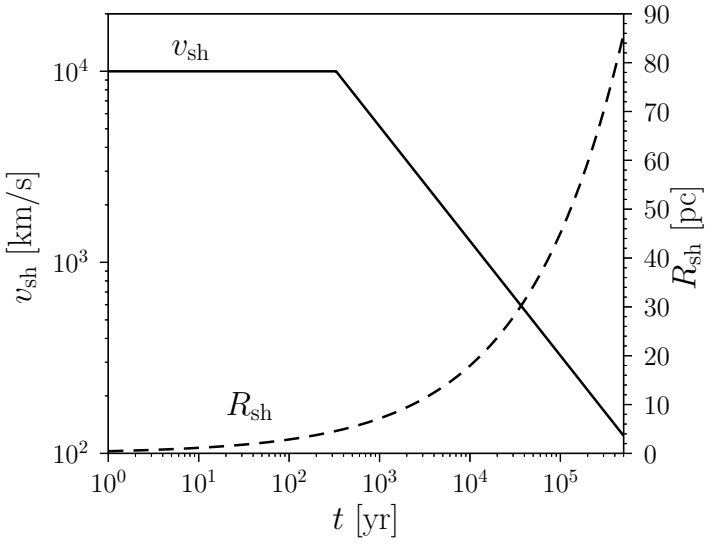

Figure 4.3. Typical expansion history for a Type Ia supernova remnant. The solid and dashed lines correspond to shock speed, $v_{\rm sh}$, and remnant radius, $R_{\rm sh}$, respectively. The free-expansion phase ends at ≈ 330 years after the explosion.

$E_{\rm SN}$ and $\rho_{\rm ISM}$ should be the dominant quantities that control the dynamics of the shock. Using dimensional analysis, we can construct the time evolution of the shock radius and velocity as $R_{\rm sh}(t) = \kappa E_{\rm SN}^{1/5} \rho_{\rm ISM}^{-1/5} t^{2/5}$ and $v_{\rm sh}(t) = 0.4\kappa E_{\rm SN}^{1/5} \rho_{\rm ISM}^{-1/5} t^{-3/5}$, respectively. For a monotonic gas, numerical calculations give $\kappa \approx 1.17$ [202]. In Fig. 4.3, we show the history of a Type Ia supernova remnant. Eventually, at even later times, radiative losses become important and the SNR merges with the ISM.

Diffusive shock acceleration of cosmic-ray protons

The standard picture for acceleration of cosmic-ray protons in the supernova shock relies on the presence of the interstellar magnetic field. This acceleration process is characterized by the angle θ between the shock normal and the background magnetic field. When θ is less (greater) than 45°, the shock is said to be quasiparallel (quasiperpendicular). For the special case of a shock with $\theta = 0^\circ$ (90°), we call it a parallel (perpendicular) shock.

In a quasiparallel shock, a small fraction[3] of the charged particles can undergo the

[3]Knowing the fraction of ions that are injected into the DSA process is one of the most difficult problems in cosmic ray physics. The standard acceleration theory utilizes the diffusion-convection equation [203]. It requires

DSA process and be Fermi-accelerated to relativistic speeds. They scatter on the magnetic irregularities upstream and downstream and diffuse across the shock multiple times, gaining energy in each crossing. However, these magnetic irregularities are not preexisting, rather they are self-generated by the accelerated particles. The energetic cosmic rays streaming ahead of the shock have a highly anisotropic velocity distribution and therefore drive plasma instabilities [208] and excite Alfvén waves in the upstream of the shock. The waves drifting at the upstream move slower than the shock front and are later advected to the downstream and amplified by the shock. The downstream is expected to be highly turbulent. On the other hand, DSA is not operative in quasiperpendicular shocks because the charged particles do not propagate more than one thermal ion Larmor radius ahead of the shock front. As a result, there is very little magnetic turbulence generation, and the downstream magnetic fields are expected to be uniform in quasiperpendicular shocks. Such features have been seen in observations of SN 1006 [209] as well as in hybrid simulations of ion acceleration [210, 211].

The characteristic lengths and amplitudes of the magnetic irregularities upstream and downstream can be inferred from the maximum energy of cosmic-ray protons. The observed cosmic-ray proton momentum spectrum is a power law with a nearly constant spectral index up to the "knee" energy, 10^6 GeV, which indicates that cosmic-ray protons are Fermi-accelerated by one mechanism in each acceleration site–the DSA mechanism in supernova remnants [212]. However, it was shown that considering the spatial dependence of the upstream diffusion coefficients and the finite lifetime of supernova remnants, the maximum energy of cosmic rays undergoing the DSA process is only 10^4 GeV [213]. This result is obtained with the assumptions that (1) the upstream magnetic irregularities are driven by streaming instability and (2) the diffusion coefficient at the downstream is the Bohm-type, i.e., $\delta B/B \sim 1$. Since the turbulent

isotropic pitch-angle distributions of the accelerated particles at the upstream and downstream of the shock and only works for particles with speed significantly greater than the shock speed [204]. The difficulty of determining the injection fraction is that the kinematics of low energy ions is extremely complicated as one has to simultaneously consider how the downstream thermal ions enter the upstream (or how the upstream ions are reflected by the potential barrier at the shock front [205]), drive a streaming instability, scatter at pitch angle, gain energy for the first few shock-crossings, escape the backstreaming Alfvén waves, and eventually diffuse across the shock front multiple times, all before being advected to the far downstream [206, 207]. This challenge is known as *injection problem*.

magnetic fields are excited by cosmic rays, we expect the characteristic wavelengths of the excited waves should be comparable to the Larmor radius of the cosmic-ray protons. So the largest scale turbulence has a wavelength of approximately one Larmor radius of 10^4 GeV cosmic-ray protons. Assuming a downstream magnetic field of 10 μG, the downstream magnetic turbulence in quasiparallel shocks is present for length scales up to $\approx 10^{-3}$ pc with turbulence strength $\delta B/B \sim 1$.

To accelerate cosmic-ray protons to the knee energy in the supernova remnants, the diffusion coefficient has to be increased beyond the Bohm limit. This can be achieved if the turbulent magnetic fields are amplified to the level $\delta B/B \sim 10 - 100$. Such large magnetic turbulence likely is achieved by nonresonant hybrid instability in fairly young supernova remnants ($R \lesssim 1$ pc) [214]. However, younger supernovae cover less volume and so their impact in sweeping up mDM (which we will discuss in Sec. 4.2.2) is relatively small compared to the older remnants. For simplicity, we will only consider magnetic turbulence driven by cosmic-ray protons with energy up to 10^4 GeV.

4.2.2 The dark sector: mDM plunging into the downstream plasma

The standard picture of the shock wave described above is restricted to the ions and electrons. We will take this as the leading dynamics for the supernova shock and treat mDM as test particles. Now we consider the dynamics of mDM particles as they enter the shock front. We will always work in the parameter space below the red dashed line in Fig. 4.1 so that the mDM Larmor radius is always several orders of magnitude larger than the ion Larmor radius, $r_{\mathrm{L}\chi}/r_{\mathrm{L}i} \gg 1$.

Unlike the ion and electron flows which are dissipated at the shock transition zone through collective plasma effects, the mDM flow would not be isotropized in the same region. This is because the mDM Larmor radius is much larger than the width of the shock transition zone (about a few ion Larmor radii). Instead, the mDM should pass through the shock transition zone undeflected and plunge into the downstream ion-electron plasma. In the following, we will

study how mDM particles interact with the downstream plasma so that they can be swept up by the supernova remnant. We will consider the possibility that mDM scatters on the magnetic turbulence driven by cosmic-ray protons as well as plasma waves driven by mDM particles.

The diffusion of mDM in quasiparallel shocks

In the presence of magnetic irregularities driven by cosmic rays in the quasiparallel shock, mDM particles can undergo pitch-angle diffusion, which permits the mDM to be deflected by an $\mathcal{O}(1)$ angle and thus be swept up by the supernova remnant. The diffusion happens when the mDM Larmor radius, $r_{\mathrm{L}\chi} = m_\chi c V_0/|q_\chi|B$, is comparable to the wavelength of the magnetic irregularities, λ. Here $V_0 = 3v_{\mathrm{sh}}/4$ denotes the speed of the mDM flow in the rest frame of the downstream fluid. The associated mean free path for mDM pitch angle scattering[4] through 90° is [217]

$$L_{\mathrm{mfp}} \approx \frac{r_{\mathrm{L}\chi}}{(\delta B/B)^2}. \tag{4.2}$$

To sweep up ambient mDM, (1) the pitch angle diffusion condition has to be satisfied, i.e., $r_{\mathrm{L}\chi} \approx \lambda$, and (2) the mean free path cannot exceed the size of the supernova remnant.

As we discussed previously, turbulent magnetic fields driven by cosmic-ray protons in a quasiparallel supernova shock exist for wavelengths up to $\lambda_{\mathrm{max}} \sim 10^{-3}$ pc with turbulence strength $\delta B/B \sim 1$. Thus, mDM with $r_{\mathrm{L}\chi} < 10^{-3}$ pc can diffuse in the quasiparallel shock and L_{mfp} is approximately $r_{\mathrm{L}\chi}$, in which case L_{mfp} does not exceed the size of the supernova remnant. As a result, the condition that mDM can scatter with the magnetic turbulence and be swept-up by the quasiparallel shock is given as

$$\left(\frac{300\ \mathrm{km/s}}{v_{\mathrm{sh}}}\right)\left(\frac{|q_\chi|/e}{8.4\times10^{-11}}\right)\left(\frac{\mathrm{MeV}}{m_\chi}\right) > 1, \tag{4.3}$$

[4]Note that the pitch angle diffusion and the sweep-up of mDM discussed here are restricted to the downstream of the quasiparallel shock. It is possible that the a small fraction of the charged particles can diffuse in the cosmic ray driven turbulent environment, cross the shock front multiple times, and start the DSA process. This idea has been applied to the dust grain acceleration in the supernova shocks [215, 216], and it could be a potential mechanism for cosmic-ray mDM acceleration.

where we assume the downstream magnetic field is 10 μG.

Plasma instabilities in supernova remnants

As discussed above, mDM cannot undergo pitch angle scattering off cosmic-ray driven turbulence in some scenarios: (1) if the mDM Larmor radius is larger than 10^{-3} pc in a quasiparallel shock, or (2) for any mDM Larmor radius in a quasiperpendicular shock, where there is little turbulence generated from cosmic-ray protons. For these cases, we will show instead that the mDM bulk flow can self-generate plasma waves and thus be swept-up by the expanding supernova remnants. Since in both cases the mDM Larmor radius is larger than any magnetic irregularities in the downstream plasma, we can approximately treat the mDM as experiencing an ordered background magnetic field. The bulk of this work will then be devoted to analyzing possible mDM plasma instabilities in a homogeneous magnetic field.

In this section, we summarize the possible plasma instabilities that would allow a supernova shock to sweep up ambient mDM particles. In the frame of the shocked gas, we can treat the incoming mDM particles as a beam of charged particles moving with the bulk speed $V_0 = 3v_{\rm sh}/4$ and with the internal thermal speed approximately the Milky Way virial speed, $v_{{\rm th},\chi} = v_{\rm vir} \approx 220$ km/s [218]. The relative motion between the mDM beam and the shocked interstellar material then provides the free energy to drive plasma instabilities and excite plasma waves. Once the waves are excited, they will back-scatter on the mDM particles and slow down the mDM beam in the expanding fluid. That is, the mDM particles interact with the downstream fluid through wave-particle scattering. We assume the velocity distribution of the mDM particles becomes isotropized in the downstream frame when the instability saturates, and there is no more free energy to drive a plasma instability.

Unfortunately, there is no observational evidence guiding us as to which plasma waves and instabilities would be excited by mDM. For example, we do not know *a priori* the wave frequency, wavelength, and the propagation direction (parallel or perpendicular to $\mathbf{B}_0$). Nor do we know about the wave polarization (electrostatic vs. electromagnetic). In addition, there are

several dozens of plasma waves and more than 50 kinds of plasma instabilities. As a starting point, here we will consider some of the most representative waves and instabilities that occur in the formation of astrophysical shocks [219–225] as well as the anomalous heating in the pinch experiments [226–229].

Table 4.1. The plasma instabilities studied in this work. Here $\mathbf{B}_0$ and $\mathbf{k}$ denote the ordered magnetic field in the downstream and the wave vector, respectively. The abbreviation ES and EM stand for electrostatic (longitudinal polarization) and electromagnetic (transverse polarization), respectively.

Instability	Type	Beam direction	Wave direction	Frequency	Instability
Ion-acoustic	ES	$\mathbf{V}_0 \parallel \mathbf{B}_0$	$\mathbf{k} \parallel \mathbf{B}_0$	$< \omega_{\mathrm{p}i}$	No
Langmuir	ES	$\mathbf{V}_0 \parallel \mathbf{B}_0$	$\mathbf{k} \parallel \mathbf{B}_0$	$> \omega_{\mathrm{p}e}$	No
Lower-hybrid	ES	$\mathbf{V}_0 \perp \mathbf{B}_0$	$\mathbf{k} \perp \mathbf{B}_0$	$\sim \sqrt{\lvert\Omega_i\Omega_e\rvert}$	No
beam-firehose	EM	$\mathbf{V}_0 \parallel \mathbf{B}_0$	$\mathbf{k} \parallel \mathbf{B}_0$	$\lesssim \lvert\Omega_\chi\rvert$	Yes
Weibel	EM	$\mathbf{V}_0 \perp \mathbf{B}_0$	$\mathbf{k} \parallel \mathbf{B}_0$	$\lesssim \lvert\Omega_\chi\rvert$	Yes

In Table 4.1, we list the plasma waves and instabilities studied in this work. As a simplified model, we will take the downstream as a spatially homogeneous plasma immersed in an ordered magnetic field $\mathbf{B}_0 = B_0\hat{\mathbf{z}}$. We also assume the growth time of any mDM-driven instability in the supernova remnant is much greater than the dissipation time of interstellar protons and electrons at the shock front so that the mDM is treated as a beam drifting through the fully ionized hot proton/electron gas. With these assumptions, we find that the electrostatic waves are not excited because (1) the ion Landau damping dissipates the ion-acoustic and lower-hybrid waves, and (2) the mDM beam velocity is lower than the velocity threshold for exciting the Langmuir waves. On the other hand, electromagnetic waves may be excited in the low frequency regime ($\lesssim \Omega_\chi$). This is because the ion cyclotron frequency, Ω_i, is much higher than the frequency of the mDM-driven electromagnetic waves, and thus ion cyclotron damping is avoided. Each of these instabilities is described in detail in Sec. 4.3 and 4.4.

We conclude this overview of mDM dynamics by providing a table of the notation used frequently throughout this work, Table 4.2. We will present equations in CGS-Gaussian units

where the electric charge $e = \sqrt{\alpha\hbar c} = 4.8 \times 10^{-10}$ statC. The relevant physical quantities for a particles species j are the number density n_j, electric charge q_j, magnetic field strength in the shocked matter B_0, mass of the particle m_j, velocity of the particle v_j, temperature T_j, and mass density ρ_j.

Table 4.2. Notation used frequently in this work. We adopt CGS-Gaussian units and set $k_b = 1$.

plasma frequency	$\omega_{\mathrm{p}j} \equiv \sqrt{4\pi n_j q_j^2/m_j}$	Larmor frequency	$\Omega_j \equiv q_j B_0/m_j c$
Larmor radius	$r_{\mathrm{L}j} \equiv m_j c v_j/q_j B_0$	Debye screening length	$\lambda_{\mathrm{D}j} \equiv \sqrt{T_j/4\pi n_j q_j^2}$
thermal speed	$v_{\mathrm{th},j} \equiv \sqrt{2T_j/m_j}$	Alfvén speed	$v_{\mathrm{A}} \equiv \sum_j B_0/\sqrt{4\pi\rho_j}$

4.3 Electrostatic waves and instabilities

In this section, we study the possible electrostatic (longitudinal polarization) instabilities driven by an mDM beam. We will take a perturbative approach, where the mDM beam is treated as a perturbation to the remnant plasma, and determine the linear response. This approach is justified because the mDM plasma frequency is negligible compared to ion and electron plasma frequencies due to the small mDM electric charge. Given the parameter space we consider in this work, $|\Omega_\chi/\Omega_i| < 10^{-3}$, we are always working in the limit of small mDM plasma frequency, $\omega_{\mathrm{p}\chi}/\omega_{\mathrm{p}i} < 10^{-3}\sqrt{\rho_\chi/\rho_i} \ll 1$. With this assumption, the mDM does not change the dispersion relation of existing plasma waves in the Milky Way at a noticeable level.

While there are many kinds of electrostatic waves and instabilities, we choose three representative candidates as the most likely mDM instabilities: the ion-acoustic and Langmuir waves for $\mathbf{k} \parallel \mathbf{B}_0$ propagation and lower-hybrid waves for $\mathbf{k} \perp \mathbf{B}_0$ propagation. The reason we choose these three is motivated by their critical roles in the formation of astrophysical collisionless shocks (e.g., solar dust grain plasma [219], earth bow shock [220], colliding stellar winds [221]) as well as the notorious turbulence heating in the theta-pinch experiments [226–229]. However, while many astrophysical shocks have high beam velocity, the mDM beam

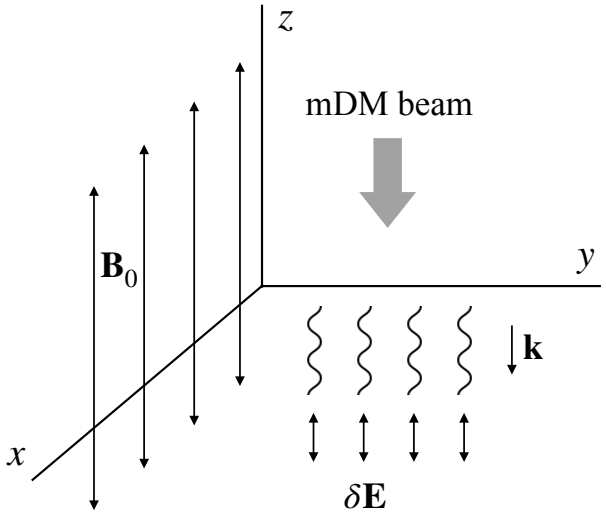

Figure 4.4. The environment in the downstream plasma frame, and our setup for a parallel shock where $\mathbf{B}_0 = B_0\hat{\mathbf{z}}$ is parallel to shock normal. In this frame, the shock front propagates with velocity $(v_{\rm sh}/4)\hat{\mathbf{z}}$ and the ambient mDM is treated as a weak beam flowing with velocity $\mathbf{V}_0 \equiv -(3v_{\rm sh}/4)\hat{\mathbf{z}}$. The ion-acoustic and Langmuir waves driven by the mDM beam propagate parallel to $\mathbf{B}_0$.

velocity is similar to the downstream ion thermal velocity, which leads to an unavoidable strong Landau damping. As a result, we show below that these electrostatic waves are not excited by the mDM beam.

4.3.1 Parallel shock (ion-acoustic and Langmuir waves)

We first consider the parallel shock scenario, defined as $\mathbf{B}_0 \parallel \mathbf{V}_0$, where $\mathbf{V}_0$ is the relative drift velocity between the mDM and the downstream electron-proton plasma. The setup is shown in Fig. 4.4. We examine the possibility of an mDM beam driving ion-acoustic and Langmuir wave instabilities. We choose these two representative electrostatic plasma waves for the following reason. In a parallel shock, the electrostatic waves are most easily excited when $\mathbf{k} \parallel \mathbf{V}_0$ and we therefore restrict to the case of parallel propagation, $\mathbf{k} \parallel \mathbf{B}_0$. Then the motions of the charged particles (e^-, i^+ and $\chi^\pm$) associated with this wave excitation/perturbation are parallel to $\mathbf{B}_0$, and the magnetic field does not alter the trajectories of these particles. As a result, electrostatic waves with $\mathbf{k} \parallel \mathbf{B}_0$ propagation would have dispersion relation identical to that of electrostatic waves

in a (magnetic)field-free plasma [230]. The two electrostatic waves for the field-free plasma are ion-acoustic waves in the low frequency regime ($\omega < \omega_{\mathrm{p}i}$) and Langmuir waves in the high frequency regime ($\omega > \omega_{\mathrm{p}e}$), and so we study these waves.

Here we consider an mDM beam flowing through a background plasma consisting of Maxwellian electrons and protons. The normalized velocity distribution of each species is

$$F_{0j}(\mathbf{v}) = \left(\frac{m_j}{2\pi T_j}\right)^{3/2} \exp\left(-\frac{m_j|\mathbf{v}|^2}{2T_j}\right), \quad j = e^-, i^+, \tag{4.4a}$$

$$F_{0\chi}(\mathbf{v}) = \left(\frac{m_\chi}{2\pi T_\chi}\right)^{3/2} \exp\left(-\frac{m_\chi}{2T_\chi}(\mathbf{v}-\mathbf{V_0})^2\right). \tag{4.4b}$$

We take the mDM thermal velocity to be the virial speed of Milky Way halo, i.e., $v_{\mathrm{th},\chi} = \sqrt{2T_\chi/m_\chi} \approx v_{\mathrm{vir}} \approx 220$ km/s.

We take the standard approach for a linear stability analysis, wherein we determine the dielectric function in the presence of these species and study the imaginary part induced by the mDM beam. In Appendix 4.A.1, we provide a detailed derivation of the dispersion relation for electrostatic waves (that is, longitudinal polarization with $\mathbf{k} \parallel \delta\mathbf{E}$) and parallel propagation, $\mathbf{k} \parallel \mathbf{B}_0$. Electrostatic waves have a dispersion relation determined by the poles of the dielectric function,

$$0 = D(\omega_r + i\gamma, \mathbf{k}) = 1 + \frac{2\omega_{\mathrm{p}i}^2}{k^2 v_{\mathrm{th},i}^2}\left[1 + \xi_i Z(\xi_i)\right] + \frac{2\omega_{\mathrm{p}e}^2}{k^2 v_{\mathrm{th},e}^2}\left[1 + \xi_e Z(\xi_e)\right] + \frac{2\omega_{\mathrm{p}\chi}^2}{k^2 v_{\mathrm{th},\chi}^2}\left[1 + \xi_\chi Z\left(\xi_\chi\right)\right], \tag{4.5}$$

where we have written the frequency in terms of real (ω_r) and imaginary (γ) parts, and ξ_i, ξ_e and ξ_χ are defined by

$$\xi_i = \frac{\omega_r + i\gamma}{k v_{\mathrm{th},i}}, \quad \xi_e = \frac{\omega_r + i\gamma}{k v_{\mathrm{th},e}}, \quad \xi_\chi = \frac{\omega_r - \mathbf{k}\cdot\mathbf{V}_0 + i\gamma}{k v_{\mathrm{th},\chi}}, \tag{4.6}$$

with $\mathbf{k}\cdot\mathbf{V}_0 = kV_0$ and $v_{\mathrm{th},j} = \sqrt{2T_j/m_j}$. The function $Z\left(\xi_j\right)$ is referred to as the *plasma dispersion function*, and defined explicitly in Eq. (4.37). The first three terms in Eq. (4.5) support

standard ion-acoustic and Langmuir waves. The last term, the dark matter contribution, can be neglected in determining the real oscillation frequency ω_r of the plasma waves because we are working in the limit of $\omega_{p\chi}/\omega_{pi} \ll 1$. However, it is essential to include this term when calculating the growth rate γ of the plasma waves, since the mDM beam is the only source of excess kinetic energy for driving an instability. Both the physics and approach here is reminiscent of the well-studied *bump-on-tail instability* where an electron beam drifting with high velocity excites a Langmuir wave. In the following, we consider the possibility of having an instability in the ion-acoustic and Langmuir wave frequency regimes.

Ion-acoustic waves

The ion-acoustic wave is a type of longitudinal oscillation in an unmagnetized plasma or in a magnetized plasma when $\mathbf{k} \parallel \mathbf{B}_0$. Its oscillation frequency is so low that the electrons are essentially locked to the oscillation of ions. The phase speed of the ion-acoustic wave is approximately $\omega/k \sim \sqrt{(T_e + T_i)/m_i}$, which is due to the restoring force of electron and ion thermal pressures. If $T_e \sim T_i$, the phase velocity is close to thermal ion velocity which suggests that a large fraction of ions can experience nearly constant electrostatic fields from the waves – as if ions are "surfing" on them. Moreover, there is a large negative slope in the ion velocity distribution at the phase speed: physically, there are more thermal ions that are moving a bit slower than the phase speed, which takes away energy from the waves, compared to thermal ions moving slightly faster than the phase speed, which would give energy to the waves. The net effect is that the waves suffer from rapid energy loss due to ion Landau damping. On the other hand, if $T_e \gg T_i$ then the phase speed is on the tail of the ion distribution function, $\omega/k \gg v_{\mathrm{th},i}$. Then there would be far fewer thermal ions "surfing" on the waves, and there is a reduced slope in the velocity distribution at the phase speed. The damping from ions is greatly suppressed in this case.

In a supernova shock environment, the electron and proton fluids are each isotropized after they cross the shock front. Each species has the same initial velocity in the downstream

frame, which implies $T_e/T_i \approx m_e/m_i \approx 1/1836$ just behind the shock. The electrons are then heated to several tenths of T_i through plasma instabilities [231, 232], but the final electron-ion temperature equilibration is caused by the electron-proton Coulomb scattering and the process takes about ~ 100 years [198]. However, the fact that $T_e \lesssim T_i$ suggests ion-acoustic waves suffer strong ion Landau damping. It is therefore not possible for mDM to excite any ion-acoustic waves in the supernova shock environment.

In the following discussion, we will demonstrate the problem of strong ion Landau damping by taking the case $T_e \gg T_i$. Although this does not correspond to the temperature ratio in the SNR, it allows us to obtain an analytic result and see that Landau damping prevents an mDM instability even in a scenario where reduced damping is expected. In the $T_e \gg T_i$ limit, the phase velocity is in the range $v_{\mathrm{th},i} \ll \omega_r/k \ll v_{\mathrm{th},e}$ which corresponds $\xi_e \ll 1$ and $\xi_i \gg 1$. Using the asymptotic expansions for $Z(\xi_j)$ given in Eqs. (4.38) and (4.39), the real part of the dispersion relation in Eq. (4.5) becomes

$$0 = D_{\mathrm{Re}}\left(\omega_r, k\right) \approx 1 - \frac{\omega_{\mathrm{p}i}^2}{\omega_r^2} + \frac{1}{k^2 \lambda_{\mathrm{D}e}^2}, \tag{4.7}$$

where $\lambda_{\mathrm{D}e} \equiv \sqrt{T_e/4\pi n_e e^2}$ is the electron Debye length. (The mDM contribution to D_r is neglected since we are working in the limit $\omega_{\mathrm{p}\chi}/\omega_{\mathrm{p}i} \ll 1$.) The phase velocity is

$$\frac{\omega_r}{k} \approx \sqrt{\frac{T_e/m_i}{1 + k^2 \lambda_{\mathrm{D}e}^2}}, \tag{4.8}$$

where $\sqrt{T_e/m_i} \equiv c_s$ is the ion sound speed. The real oscillation frequency ω_r ranges from kc_s for $k^2\lambda_{\mathrm{D}e}^2 \ll 1$ to $\omega_{\mathrm{p}i}$ for $k^2\lambda_{\mathrm{D}e}^2 \gg 1$.[5]

Next, to evaluate the growth rate for a wave with $\mathbf{k} \parallel \mathbf{B}_0$, we take the limit $|\gamma/\omega_r| \ll 1$

[5]Note that the assumption of $\omega_r/k \gg v_{\mathrm{th},i}$ breaks down when $k^2\lambda_{\mathrm{D}e}^2 \gtrsim T_e/T_i$, and the ion Landau damping becomes strong again. In the limit $k^2\lambda_{\mathrm{D}e}^2 \gg T_e/T_i$ where the phase velocity $\omega_r/k \ll v_{\mathrm{th},i}, v_{\mathrm{th},e}$, there is no collective electrostatic plasma waves since the thermal ions and electrons can travel for significantly more than one wavelength, k^{-1}, within one period, ω_r^{-1}. That is, any formation of electrostatic plasma waves will be "washed out" immediately. In the following discussion we always work in the limit $k^2\lambda_{\mathrm{D}e}^2 < T_e/T_i$.

and use Eqs. (4.44) and (4.46). Then the damping rate from electrons plus ions, γ_{e+i}, is

$$\begin{aligned}\frac{\gamma_{e+i}}{|\omega_r|} &\approx -\sqrt{\frac{\pi}{8}}\left(\frac{|\omega_r/k|}{\omega_{\mathrm{p}i}\lambda_{\mathrm{D}e}}\right)^3\left[\sqrt{\frac{m_e}{m_i}}\exp\left(-\frac{\omega_r^2/k^2}{v_{\mathrm{th},e}^2}\right)+\left(\frac{T_e}{T_i}\right)^{3/2}\exp\left(-\frac{\omega_r^2/k^2}{v_{\mathrm{th}i}^2}\right)\right] \\ &\approx -\sqrt{\frac{\pi}{8}}\frac{1}{\left(1+k^2\lambda_{\mathrm{D}e}^2\right)^{3/2}}\left[\sqrt{\frac{m_e}{m_i}}+\left(\frac{T_e}{T_i}\right)^{3/2}\exp\left(-\frac{T_e}{2T_i\left(1+k^2\lambda_{\mathrm{D}e}^2\right)}\right)\right],\end{aligned} \tag{4.9}$$

and the growth rate from mDM, γ_χ, is

$$\frac{\gamma_\chi}{|\omega_r|} \approx \sqrt{\pi}\left(\frac{\omega_{\mathrm{p}\chi}}{\omega_{\mathrm{p}i}}\right)^2\left|\frac{\omega_r/k}{v_{\mathrm{th},\chi}}\right|^3\left(\frac{V_0}{\omega_r/k}-1\right)\exp\left(-\frac{(\omega_r/k-V_0)^2}{v_{\mathrm{th},\chi}^2}\right). \tag{4.10}$$

The total growth rate is $\gamma=\gamma_{e+i}+\gamma_\chi$. From Eq. (4.10), we find that the necessary condition to get $\gamma_\chi>0$ is $V_0>\omega_r/k$. Rewriting the beam speed as $V_0=3v_{\mathrm{sh}}/4\approx 1.1\,v_{\mathrm{th},i}$, and using Eq. (4.8), we can simplify this condition as $k^2\lambda_{\mathrm{D}e}^2>T_e/2.4T_i-1$. For plasmas with $T_e/T_i<2.4$, all k modes have $\gamma_\chi>0$. For plasmas with $T_e/T_i>2.4$, only the modes with $k\lambda_{\mathrm{D}e}>\sqrt{T_e/2.4T_i-1}$ have $\gamma_\chi>0$.

Figure 4.5 shows the damping rate from electrons plus ions, γ_{e+i}, and the growth rate from mDM, γ_χ. We assume $\omega_{\mathrm{p}\chi}/\omega_{\mathrm{p}i}=10^{-3}$ and $v_{\mathrm{sh}}=500$ km/s, and consider plasmas with $T_e/T_i=5$ and 10. (Note that γ_χ is only plotted in the k range where $\gamma_\chi>0$.) It is clear from Fig. 4.5 that damping dominates over growth at all $k\lambda_{\mathrm{D}e}$, due in part to the strong suppression of the mDM contribution by $(\omega_{\mathrm{p}\chi}/\omega_{\mathrm{p}i})^2<10^{-6}$. We have checked the same conclusion is also true for shocks at the beginning of supernova explosion ($v_{\mathrm{sh}}\sim 10^4$ km/s) to the end of the Sedov-Taylor phase ($v_{\mathrm{sh}}\sim 200$ km/s). As a result, the mDM would not be swept up by the SNR via an ion-acoustic wave instability.

Langmuir waves

We now consider the Langmuir waves that exist in the large frequency regime ($\omega>\omega_{\mathrm{p}e}$). Langmuir waves, also known as electron plasma oscillations, are a type of fast-oscillating longitudinal wave in an unmagnetized plasma or in a magnetized plasma when $\mathbf{k}\parallel\mathbf{B}_0$. The

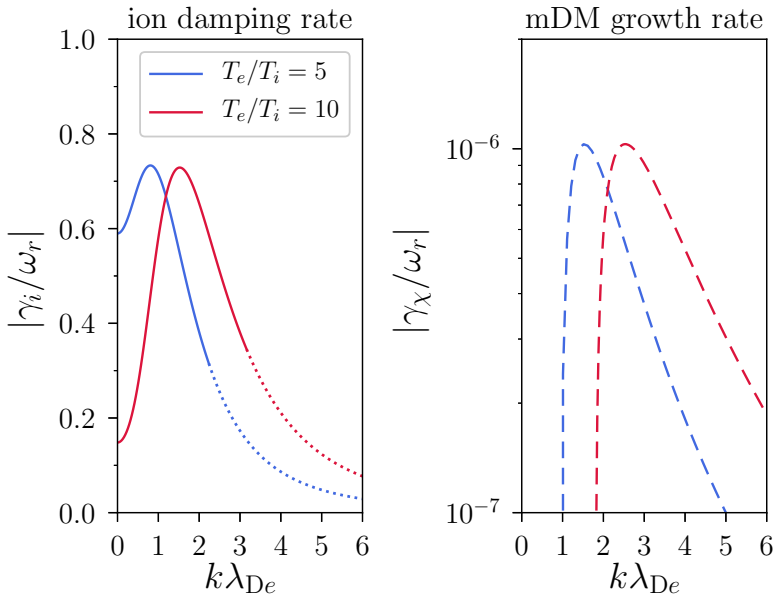

Figure 4.5. The damping of ion-acoustic waves from thermal ions (solid lines) from Eq. (4.9), and growth from mDM (dashed lines) from Eq. (4.10). Here we assumed $\omega_{p\chi}/\omega_{pi} = 10^{-3}$ and $v_{sh} = 500$ km/s. The dotted lines correspond to the regime $k^2\lambda_{De}^2 > T_e/T_i$ where Eq. (4.9) breaks down and there are no collective plasma oscillations. The damping rate from ions is significantly higher than the growth rate from mDM at all $k\lambda_{De}$. We have checked the same conclusion is true for shocks from the beginning of the supernova explosion ($v_{sh} \sim 10^4$ km/s) to the end of the Sedov-Taylor phase ($v_{sh} \sim 200$ km/s).

oscillation is so rapid that the thermal ions are not able to catch up with the waves, and ions are essentially a static background, $m_i \to \infty$ and $|\xi_i| \to \infty$. As a result, the dispersion relation of the Langmuir waves is exclusively dictated by electrons.

Similar to the discussion for ion acoustic waves, in order to avoid electron and ion Landau damping we require that the phase velocity $\omega_r/k \gg v_{th,e}, v_{th,i}$. This corresponds to $\xi_e, \xi_i \ll 1$, and in this limit the real part of the dispersion relation in Eq. (4.5) is given by

$$0 = D_{Re}(\omega_r, k) = 1 - \frac{\omega_{pe}^2}{\omega_r^2} - 3k^2\lambda_{De}^2\frac{\omega_{pe}^4}{\omega_r^4} + \cdots, \tag{4.11}$$

where again the mDM contribution is negligible in the limit $\omega_{p\chi}/\omega_{pi} \ll 1$. Solving Eq. (4.11)

gives the real wave frequency,

$$\omega_r = \omega_{\mathrm{p}e}\sqrt{1+3k^2\lambda_{\mathrm{D}e}^2+\cdots}. \tag{4.12}$$

Note that these equations are only valid for $k\lambda_{\mathrm{D}e} \ll 1$, which is required by the condition $\omega_r/k \gg v_{\mathrm{th},e}$, and that Langmuir waves with $k\lambda_{\mathrm{D}e} \sim 1$ suffer strong electron Landau damping.

The growth rate from mDM has the same form as Eq. (4.10), but with the replacement $\omega_{\mathrm{p}i} \to \omega_{\mathrm{p}e}$ and with ω_r from Eq. (4.12). And so again the condition for $\gamma_\chi > 0$ is $V_0 > \omega_r/k$. The phase speed in the regime $k\lambda_{\mathrm{D}e} \lesssim 1$ is approximately $\omega_r/k \gtrsim \omega_{\mathrm{p}e}\lambda_{\mathrm{D}e} = v_{\mathrm{th},e}/\sqrt{2}$. As discussed earlier, the electrons are heated up to several tenths of T_i behind the shock front due to plasma instabilities [231, 232], corresponding to $v_{\mathrm{th},e} \sim \sqrt{m_i/m_e}\, v_{\mathrm{th},i} \sim 10\, v_{\mathrm{sh}}$. Then the phase speed is much larger than the mDM beam velocity in the downstream frame, V_0, and the condition for getting $\gamma_\chi > 0$ is not satisfied. Therefore, the mDM would not be swept up by the SNR via a Langmuir wave instability.

4.3.2 Perpendicular shock (lower-hybrid wave)

For the perpendicular shock ($\mathbf{B}_0 \perp \mathbf{V}_0$), we choose lower-hybrid (LH) waves as the most likely candidate for an electrostatic wave driven by the mDM beam. The lower-hybrid wave instability is the high-frequency ($\omega \gg |\Omega_i|$) electrostatic wave driven by the cross-field plasma beam (i.e., moving perpendicular to the magnetic field $\mathbf{B}_0 = B_0\hat{\mathbf{z}}$) and the waves propagate very nearly perpendicular to $\mathbf{B}_0$. The free energy is provided either from the initial kinetic energy of the beam or from inhomogeneities in plasma density, temperature or background magnetic field. In this work, we only consider the first case since we do not expect the induced $\mathbf{E}$ and $\mathbf{E}\times\mathbf{B}$ from local electron/proton charge separation to have significant effects on the mDM trajectories near the shock front. (The latter case, also known as *lower-hybrid-drift instability*, is the major driver and free energy source for the anomalous heating in the theta pinch experiments as well as a dissipation mechanism in astrophysical shocks.)

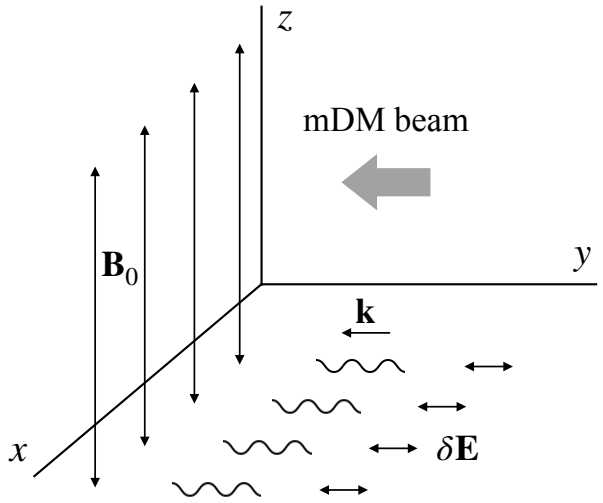

Figure 4.6. The environment in the downstream plasma frame, and our setup for a perpendicular shock where $\mathbf{B}_0$ is perpendicular to shock normal. In this frame, the shock front propagates with velocity $(v_{\rm sh}/4)\hat{\mathbf{y}}$ and the mDM is treated as a weak beam flowing with velocity $\mathbf{V}_0 \equiv -(3v_{\rm sh}/4)\hat{\mathbf{y}}$. The lower-hybrid waves driven by the mDM beam propagate perpendicular to $\mathbf{B}_0$.

The initial plasma configuration is illustrated in Fig. 4.6, and described as follows. We consider an mDM beam moving across the downstream magnetic field $\mathbf{B}_0 = B_0\hat{\mathbf{z}}$ with the beam velocity $\mathbf{V}_0 = V_0\hat{\mathbf{y}}$ in the downstream frame. We focus on wave perturbations with $k_y^2 \gg k_x^2$ and $k_z = 0$. Our choice is guided by the extensive parameter study of lower-hybrid-drift instability and modified-two-stream instability in Ref. [229] where the author shows that the maximum instability growth of the LH waves occurs for $k_y^2 \gg k_x^2$, $k_z = 0$ and $k_y^2 r_{{\rm L}e}^2 \approx 1$ when $T_e \approx T_i$. For simplicity, we write the wave vector as $\mathbf{k} = k\hat{\mathbf{y}}$.

The typical frequency of the LH waves is around $\omega_r \sim \omega_{\rm LH} \equiv \omega_{{\rm p}i}/\sqrt{1+\omega_{{\rm p}e}^2/\Omega_e^2}$. For $\omega_{{\rm p}e}^2 \gg \Omega_e^2$, which is satisfied in the supernova downstream plasma, we have $\omega_{\rm LH} = \sqrt{m_i/m_e}|\Omega_i|$ $\approx 43|\Omega_i|$. The LH wave instability is characterized by magnetized electrons where the wave vector k satisfies $k^2 r_{{\rm L}e}^2 \approx 1$ [228]. Since the thermal ion Larmor radius, $r_{{\rm L}i} \approx 43 r_{{\rm L}e}$, is larger than the characteristic wavelength of this instability, $1/k \approx r_{{\rm L}e}$, we treat the ions as unmagnetized. The same argument applies to mDM. As a result, the dispersion relation is given as [221, 228]

$$0 = D(\mathbf{k},\omega) = 1 + \frac{2\omega_{{\rm p}i}^2}{k^2 v_{{\rm th},i}^2}\left[1+\xi_i Z(\xi_i)\right] + \frac{\omega_{{\rm p}e}^2}{\Omega_e^2}\frac{1-I_0(b)\,e^{-b}}{b} + \frac{2\omega_{{\rm p}\chi}^2}{k^2 v_{{\rm th},\chi}^2}\left[1+\xi_\chi Z\left(\xi_\chi\right)\right], \quad (4.13)$$

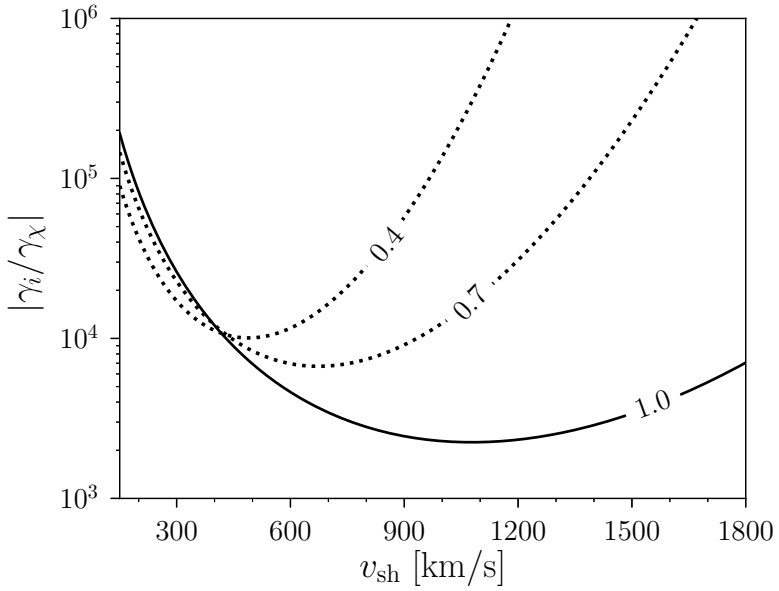

Figure 4.7. The ratio of ion damping to mDM growth rate for lower hybrid waves, $|\gamma_i/\gamma_\chi|$, as a function of shock speed. The various lines correspond to different fixed values of the ratio $\omega_r/kv_{\mathrm{th},i}$. The curves are calculated under the assumption $\omega_{\mathrm{p}\chi}/\omega_{\mathrm{p}i} = 10^{-3}$. All the curves have $|\gamma_i/\gamma_\chi| \gg 1$, which indicates that the ion Landau damping will suppress any mDM beam-driven LH wave instability.

where $b = k^2 r_{\mathrm{L}e}^2/2$, $\xi_i = \omega/kv_{\mathrm{th},i}$, $\xi_\chi = (\omega - kV_0)/kv_{\mathrm{th},\chi}$ and $I_0(b)$ is the modified Bessel function of the first kind of order zero. Note that $I_0(b)$ is real and the magnetized electrons do not contribute to damping.

Because ions behave as an unmagnetized thermal gas within one LH wavelength, the ion Landau damping to the LH waves is non-negligible. Our goal is to determine whether the ion Landau damping will stabilize the plasma or if the mDM beam can successfully excite the LH waves. Utilizing Eqs. (4.44) and (4.46b), the ratio of ion Landau damping to the mDM instability growth rate for LH waves is given as

$$\begin{aligned}\frac{\gamma_i}{\gamma_\chi} &= \frac{D^i_{\mathrm{Im}}(\mathbf{k},\omega_r)}{D^\chi_{\mathrm{Im}}(\mathbf{k},\omega_r)} \\ &= -\left(\frac{\omega_{\mathrm{p}i}}{\omega_{\mathrm{p}\chi}}\right)^2 \left(\frac{v_{\mathrm{th},\chi}}{v_{\mathrm{th},i}}\right)^3 \left(\frac{\omega_r/k}{V_0-\omega_r/k}\right) \exp\left(-\frac{\omega_r^2/k^2}{v_{\mathrm{th},i}^2} + \frac{(\omega_r/k - V_0)^2}{v_{\mathrm{th},\chi}^2}\right).\end{aligned} \tag{4.14}$$

Note that the necessary condition for $\gamma_\chi > 0$ is $\omega_r/k < V_0 = 3v_{\rm sh}/4 \approx 1.1\, v_{\mathrm{th},i}$, so we will always

work in that condition. Taking the characteristic frequency of the LH wave, $\omega_r \sim \omega_{\rm LH} \approx 43|\Omega_i|$, and the characteristic wave vector of the maximum growth rate of the LH wave instability, $k \sim 1/r_{{\rm L}e} \approx 43/r_{{\rm L}i}$, the characteristic phase velocity is approximately $v_{{\rm th},i}$. Of course, ω_r/k can be higher or lower than $v_{{\rm th},i}$, as long as $\omega_r/k < 1.1 v_{{\rm th},i}$. In Fig. 4.7, we show $|\gamma_i/\gamma_\chi|$ as a function of shock speed at various values of $\omega_r/k v_{{\rm th},i}$, assuming $\omega_{{\rm p}\chi}/\omega_{{\rm p}i} = 10^{-3}$. Note that decreasing $\omega_{{\rm p}\chi}/\omega_{{\rm p}i}$ would only raise the curves of $|\gamma_i/\gamma_\chi|$, meaning a weaker growth rate from the mDM beam. Therefore, we find ion Landau damping is dominant over the growth rate from the mDM beam, and we do not expect mDM to be swept up by the supernova remnant via a LH wave instability.

4.4 Electromagnetic waves and instabilities

In this section, we investigate the possibility of mDM exciting transverse electromagnetic (EM) waves in the downstream plasma, in the presence of a background magnetic field $\mathbf{B}_0$. We will show that an instability could occur with growth rate $\gamma \sim |\Omega_\chi|$. While the EM waves can, in general, propagate along arbitrary directions, we restrict our attention to wave propagation along $\mathbf{B}_0$ ($\mathbf{k} \parallel \mathbf{B}_0$). Our choice is motivated by abundant observations of the enhanced magnetic fluctuations in the solar winds, which indicate that the dominant and the fastest growing EM instability modes propagate approximately parallel or antiparallel to $\mathbf{B}_0$ [233–236]. In that case, there are a variety of kinetic waves and associated instabilities, e.g., Alfvén waves with the firehose instabilities, ion cyclotron waves with the ion cyclotron instability, and electron cyclotron waves with the electron Whistler instability. Here we focus on transverse-polarization, parallel-propagating EM waves in a supernova shock. We then consider two limiting cases: a beam-firehose instability in a parallel shock ($\mathbf{V}_0 \parallel \mathbf{B}_0$) and a Weibel instability in a perpendicular shock ($\mathbf{V}_0 \perp \mathbf{B}_0$).

Similar to the approach of the previous section, here we solve for the linear dispersion relation for a transverse EM wave propagating along $\mathbf{B}_0 = B_0\hat{\mathbf{z}}$ with wave vector $\mathbf{k} = k\hat{\mathbf{z}}$. Then

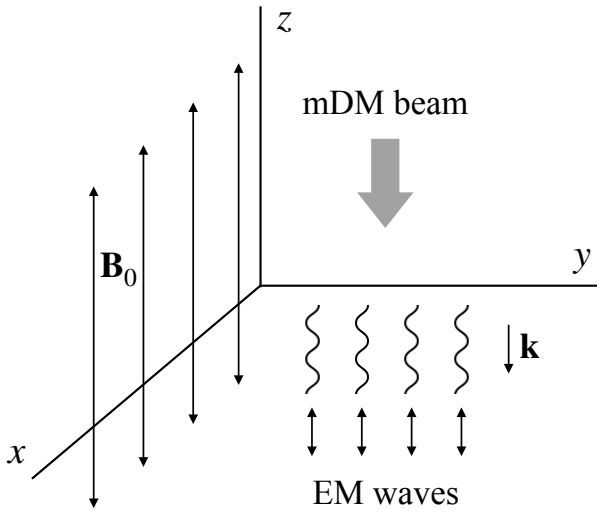

Figure 4.8. The environment in the downstream plasma frame, and our setup for a parallel shock where $\mathbf{B}_0 = B_0\hat{\mathbf{z}}$ is parallel to shock normal. In this frame, the shock front propagates with velocity $(v_{\rm sh}/4)\hat{\mathbf{z}}$ and the ambient mDM is treated as a weak beam flowing with velocity $\mathbf{V}_0 \equiv -(3v_{\rm sh}/4)\hat{\mathbf{z}}$. The excess of kinetic energy along $\mathbf{B}_0$ can drive a beam-firehose instability and excite EM waves.

the electric field perturbation can be written as $\delta\mathbf{E} = \delta E_x\hat{\mathbf{x}} + \delta E_y\hat{\mathbf{y}}$ and the general form of the linear dispersion relation can be expressed as [237]

$$0 = D^{\pm}(k,\omega) = c^2k^2 - \omega^2 + \sum_j \omega_{{\rm p}j}^2 \int d^3\mathbf{v} \frac{(\omega - kv_z)F_{0j} - \frac{1}{2}kv_\perp^2\left(\partial F_{0j}/\partial v_z\right)}{\omega - kv_z \pm \Omega_j}. \tag{4.15}$$

The superscript of $D^{\pm}$ and the $\pm$ sign in front of Ω_j denote the right-handed ($+$, $\delta E_x = -i\delta E_y$) and left-handed ($-$, $\delta E_x = i\delta E_y$) EM waves. A cylindrical coordinate system for the velocity space is used and the integration is over the range $\int d^3\mathbf{v} = \int_0^\infty 2\pi v_\perp dv_\perp \int_{-\infty}^\infty dv_z$.

4.4.1 Beam-firehose instability in a parallel shock

In the case of a parallel shock, we will show that the excess of kinetic energy from the mDM beam in the direction parallel to $\mathbf{B}_0$ can enhance EM perturbations and drive a beam-firehose instability.[6] An illustration is shown in Fig. 4.8. Physically, the firehose instability is

[6]Note that the instability studied here is slightly different from the classical firehose instability [238]. In most of the literature, the firehose instability refers to the instability of the transverse EM waves propagating parallel or antiparallel to $\mathbf{B}_0$ in a two-temperature Maxwellian plasma system with $T_{j\parallel} > T_{j\perp}$ (where the subscripts $\parallel$ and $\perp$

caused by the back-reaction of the centrifugal force from charged particles moving along the curved magnetic lines $\mathbf{B} = \mathbf{B}_0 + \delta\mathbf{B}$. A small perturbation $\delta\mathbf{B}$ will cause charged particles to be redirected due to the Lorentz force, and a drift current is produced in the same direction as $\nabla \times \mathbf{B}$. This drift current induces magnetic fields transverse to $\mathbf{B}_0$ and tends to increase the curvature of $\mathbf{B}$. The magnetic perturbations will enhance exponentially in time as the process is a coupled nonlinear feedback between the curved magnetic lines and the induced currents. This mechanism is reminiscent of a swinging firehose: when the water flow passes through the bent section of the hose, the centripetal force exerted on the hose tends to amplify the curvature and the bent section becomes even more curved. The process leads to an exponential growth of the wave amplitude [239].

Now we consider the mDM beam flowing along $\mathbf{B}_0 = B_0\hat{\mathbf{z}}$ with a beam velocity in the downstream plasma frame written as $\mathbf{V}_0 = -(3v_{\rm sh}/4)\hat{\mathbf{z}}$. The dispersion relation in this scenario is obtained by substituting the velocity distributions in Eqs. (4.4a) and (4.4b) into the EM linear dispersion relation in Eq. (4.15), which gives

$$0 = D^{\pm}(k,\omega) = c^2k^2 - \omega^2 - \sum_{j=i^+,e^-} \omega_{{\rm p}j}^2 \left(\frac{\omega}{kv_{{\rm th},j}}\right) Z\left(\xi_j\right) - \sum_{s=\chi^+,\chi^-} \omega_{{\rm p}s}^2 \left(\frac{\omega - kV_0}{kv_{{\rm th},\chi}}\right) Z\left(\xi_s\right), \tag{4.16}$$

where $\xi_j = \left(\omega \pm \Omega_j\right)/kv_{{\rm th},j}$ and $\xi_s = \left(\omega - kV_0 \pm \Omega_s\right)/kv_{{\rm th},\chi}$ and $Z(\xi)$ is again the plasma dispersion function defined in Appendix 4.A.1. Assuming equal number density of χ^+ and χ^-, we have $n_{0\chi^+} = n_{0\chi^-} = n_{0\chi}/2$ and consequently $\omega_{{\rm p}\chi^+}^2 = \omega_{{\rm p}\chi^-}^2 = \omega_{{\rm p}\chi}^2/2$. For $V_0 = 0$, there is no free energy to drive an instability and Eq. (4.16) supports only stable solutions with $\gamma \leq 0$. Here we show that in the presence of the mDM beam with nonzero V_0, it is possible to excite unstable modes of a beam-firehose instability with characteristic wave frequency $|\omega| \lesssim \Omega_\chi$.

We first focus on the electrons and ions, which we assume to be strongly magnetized with $|\omega| \ll |\Omega_i|, |\Omega_e|$. In the long wavelength and low frequency limit that we are interested in,

refer to the directions relative to $\mathbf{B}_0$). The excited waves are in the Alfvén wave frequency regime, $|\omega| \ll |\Omega_i|$. On the other hand, the beam-firehose instability phrased in this work refers to a beam of mDM plasma flowing along $\mathbf{B}_0$ and driving an EM wave instability.

we have $|\xi_i|, |\xi_e| \gg 1$. Then we can approximate $Z\left(\xi_j\right) \approx -1/\xi_j$ for $j = i^+, e^-$ and simplify the ion and electron terms in Eq. (4.16):

$$\sum_{j=i^+,e^-} \frac{\omega_{\mathrm{p}j}^2 \omega}{\omega \pm \Omega_j} \approx \omega \left[\frac{\omega_{\mathrm{p}e}^2}{\pm\Omega_e} \left(1 - \frac{\omega}{\pm\Omega_e}\right) + \frac{\omega_{\mathrm{p}i}^2}{\pm\Omega_i} \left(1 - \frac{\omega}{\pm\Omega_i}\right) \right] = -\omega^2 \frac{c^2}{v_{\mathrm{A}}^2}, \tag{4.17}$$

where the charge neutrality of proton-electron plasma is used. The standard Alfvén speed v_{A} is defined as $v_{\mathrm{A}} \equiv B_0/\sqrt{4\pi\left(\rho_i + \rho_e\right)}$ and has a typical value

$$v_{\mathrm{A}} \approx 22 \text{ km/s} \left(\frac{B_0}{10\ \mu\mathrm{G}}\right) \left(\frac{1 \text{ cm}^{-3}}{n_{\mathrm{post},i}}\right)^{1/2}, \tag{4.18}$$

where $n_{\mathrm{post},i}$ denotes the proton number density in the supernova downstream fluid.

The relevant source of damping for EM waves propagating in a homogeneous plasma is cyclotron damping. For the case studied here, the cyclotron damping from thermal ions and electrons is negligible. This is because for very low frequency and long wavelength EM waves ($|\omega| \ll |\Omega_i|, |\Omega_e|$ and $|\xi_i|, |\xi_e| \gg 1$), the exponential function in the plasma dispersion function $Z\left(\xi_j\right)$ which contributes the damping is exponentially suppressed. Physically, it means the ions and electrons do not rotate at the same rate as the circularly polarized EM waves, so the waves do not undergo a cyclotron resonance. The ion (electron) cyclotron damping only becomes important when $\omega \to \Omega_i$ (Ω_e), in which case the ions (electrons) can absorb a significant amount of the energy from the electric fields of the EM waves.

In the presence of the mDM beam, the dispersion relation of right-handed EM waves becomes

$$0 = c^2k^2 - \omega^2\left(1 + \frac{c^2}{v_{\mathrm{A}}^2}\right) - \frac{\omega_{\mathrm{p}\chi}^2}{2}\left(\frac{\omega - kV_0}{kv_{\mathrm{th},\chi}}\right)\left[Z\left(\xi_{\chi^+}\right) + Z\left(\xi_{\chi^-}\right)\right]. \tag{4.19}$$

The left-handed EM waves have an identical form since $\Omega_{\chi^+} = -\Omega_{\chi^-}$. We solve Eq. (4.19) numerically assuming $B_0 = 10\ \mu$G and $n_{\mathrm{post},i} = 1 \text{ cm}^{-3}$. The results are shown in Fig. 4.9. In the left panel of Fig. 4.9, we show the real oscillation frequency $|\omega_r|$ and the growth rate γ as a function of $ck/\omega_{\mathrm{p}\chi}$ for different shock speeds, assuming $\rho_{\mathrm{DM}} = \rho_\chi = 1 \text{ GeV/cm}^3$. The value of

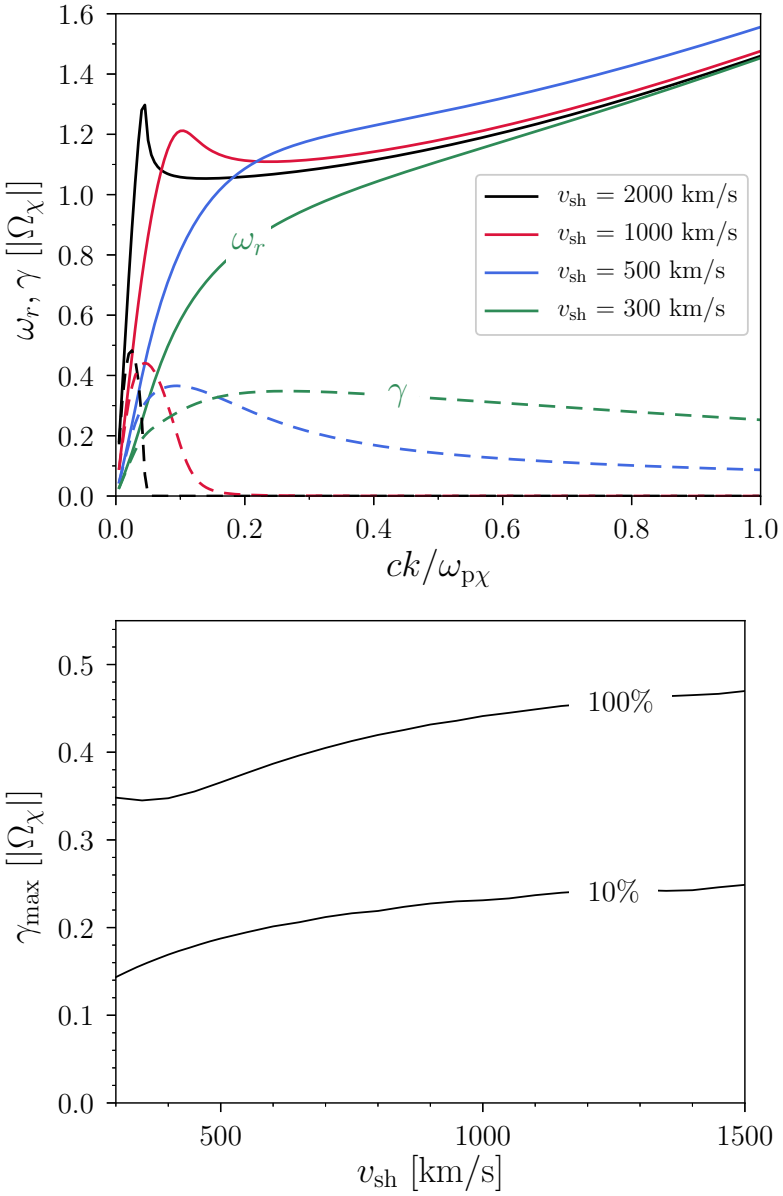

Figure 4.9. Beam-firehose instability in a parallel shock. (top) Plot of the real oscillation frequency (solid lines) and the growth rate (dashed lines) of the right/left-handed EM waves in units of $|\Omega_\chi|$. The curves are plotted assuming $\rho_{\rm DM} = \rho_\chi = 1\ {\rm GeV/cm^3}$. (bottom) Plot of the maximum growth rate as a function of shock speed. The numbers on the curves denote the fraction of the DM abundance comprised of mDM, $\rho_\chi/\rho_{\rm DM}$, assuming $\rho_{\rm DM} = 1\ {\rm GeV/cm^3}$.

k at which the maximum growth occurs is a decreasing function of the shock speed $v_{\rm sh} = 4V_0/3$. This is because the instability is most effective when the crossing time of the beam through one wavelength, $\sim 1/kV_0$, is comparable to one gyration time of $1/\Omega_\chi$, i.e., the beam is *resonant*

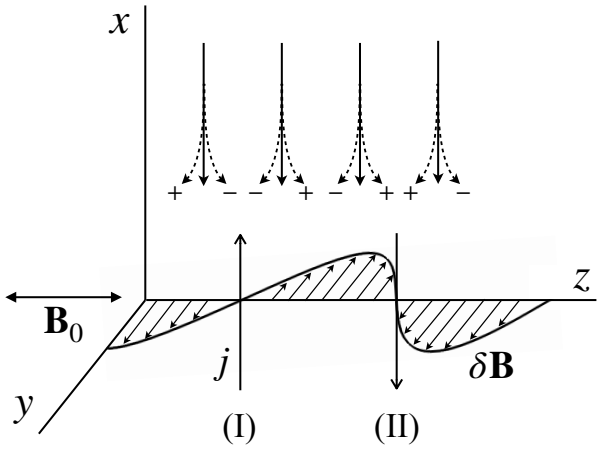

Figure 4.10. An illustration of the Weibel instability driven by the mDM beam in a perpendicular shock. The shock front faces toward the $\hat{\mathbf{x}}$ direction. An initial magnetic fluctuation, $\delta\mathbf{B}$, is assumed to be perpendicular to $\mathbf{B}_0$ and lies in the $y-z$ plane. The incoming $\chi^{\pm}$s are deflected by $\delta\mathbf{B}$ and induce current sheets pointing in opposite directions in layers I and II. The magnetic perturbations are then amplified via Ampère's Law.

with the excited EM waves. This also justifies the assumption made above that $|\xi_i|, |\xi_e| \gg 1$ since $|\xi_i| = (\omega \pm \Omega_i)/kv_{\mathrm{th},i} \sim |\Omega_\chi/kV_0||\Omega_i/\Omega_\chi| \sim |\Omega_i/\Omega_\chi| \gg 1$ and the same argument applies for the electrons as well. In the right panel of Fig. 4.9, we plot the maximum growth rate $\gamma_{\max}$ as a function of v_{sh} for various values of $\rho_\chi/\rho_{\mathrm{DM}}$, assuming $\rho_{\mathrm{DM}} = 1\ \mathrm{GeV/cm^3}$. The maximum growth rate $\gamma_{\max}$ is an increasing function of v_{sh} and $\rho_\chi/\rho_{\mathrm{DM}}$, but $\gamma_{\max}$ starts to saturate at high v_{sh}. For the optimal scenario where all DM is made up of mDM, we find $\gamma \sim 0.5|\Omega_\chi|$ for all shock speeds in the Sedov-Taylor phase ($v_{\mathrm{sh}} \gtrsim 200\ \mathrm{km/s}$).

4.4.2 Weibel instability in a perpendicular shock

In the case of a perpendicular shock, we will show that an excess of kinetic energy from the mDM beam in the direction perpendicular to $\mathbf{B}_0$ can drive a Weibel instability [240] and excite EM waves. The Weibel instability is a transverse EM instability driven by a plasma with anisotropic velocity distribution. The instability can occur even in the absence of external magnetic field. The EM waves driven by the Weibel instability is *nonresonant* with the particles. A simple physical picture of the Weibel instability is given in Ref. [241] where the author treats

a two-temperature Maxwellian gas as two counterstreaming cold plasmas. The same mechanism also applies to a single beam. In the following, we briefly describe the physical picture of the Weibel instability driven by the mDM beam, along the lines of the description in Refs [241, 242].

We consider a neutral mDM beam consisting of equal numbers of χ^+s and χ^-s and with beam velocity $\mathbf{V}_0 = -(3v_{\rm sh}/4)\hat{\mathbf{x}}$ in the downstream plasma frame. An illustration is shown in Fig. 4.10. Now consider an EM perturbation with $\mathbf{k} \parallel \mathbf{B}_0$ and $\delta\mathbf{B} \perp \mathbf{V}_0$. The Lorentz force $q_{\chi^\pm}\mathbf{V}_0 \times \delta\mathbf{B}$ deflects the mDM trajectories as shown by the dashed curves in Fig. 4.10. At layer I, the χ^-s congregate and χ^+s disperse away, resulting an induced current sheet pointing in the $\hat{\mathbf{x}}$ direction. The layer II has an opposite result, with the current sheet pointing in the $-\hat{\mathbf{x}}$ direction. The magnetic fluctuations are then amplified via Ampère's Law. Note that the fluctuations arising from this mechanism are aperiodic, i.e., $\omega_r \simeq 0$.

We determine the growth rate via the linear stability analysis. The dispersion relation in the perpendicular shock is obtained by the same method as the previous subsection, with the exception that $\mathbf{V}_0 \perp \mathbf{B}_0$. The result is expressed as

$$\begin{aligned} 0 = D^{\pm} = c^2k^2 - \omega^2 &- \sum_{j=i^+,e^-} \omega_{{\rm p}j}^2 \left(\frac{\omega}{kv_{{\rm th},j}}\right) Z\left(\xi_j\right) \\ &- \sum_{s=\chi^+,\chi^-} \omega_{{\rm p}s}^2 \left[\left(\frac{\omega}{kv_{{\rm th},\chi}}\right) Z\left(\xi_s\right) + \left(\frac{V_0}{v_{{\rm th},\chi}}\right)^2 \left(1 + \xi_s Z\left(\xi_s\right)\right) \right], \end{aligned} \tag{4.20}$$

where $\xi_j = \left(\omega \pm \Omega_j\right)/kv_{{\rm th},j}$ and $\xi_s = \left(\omega \pm \Omega_s\right)/kv_{{\rm th},\chi}$. The factor $V_0/v_{{\rm th},\chi}$ quantifies the deviation of a plasma away from an isotropic gas. For $V_0 = 0$, there is no free energy to drive the instability and Eq. (4.20) supports only stable solutions with $\gamma \leq 0$. The ions and electrons are again strongly magnetized ($|\omega| \ll |\Omega_i|, |\Omega_e|$ and $|\xi_i|, |\xi_e| \gg 1$) under the condition of small mDM Larmor frequency, $|\Omega_\chi/\Omega_i| < 10^{-3}$, and the low frequency, long wavelength EM waves that we are interested in. Thus, the thermal ions and electrons do not resonate with the EM waves and the cyclotron damping is exponentially suppressed. As a result, the sum of the ion and electron terms in Eq. (4.20) is reduced to $-\omega^2c^2/v_{\rm A}^2$ following the same reasoning discussed in

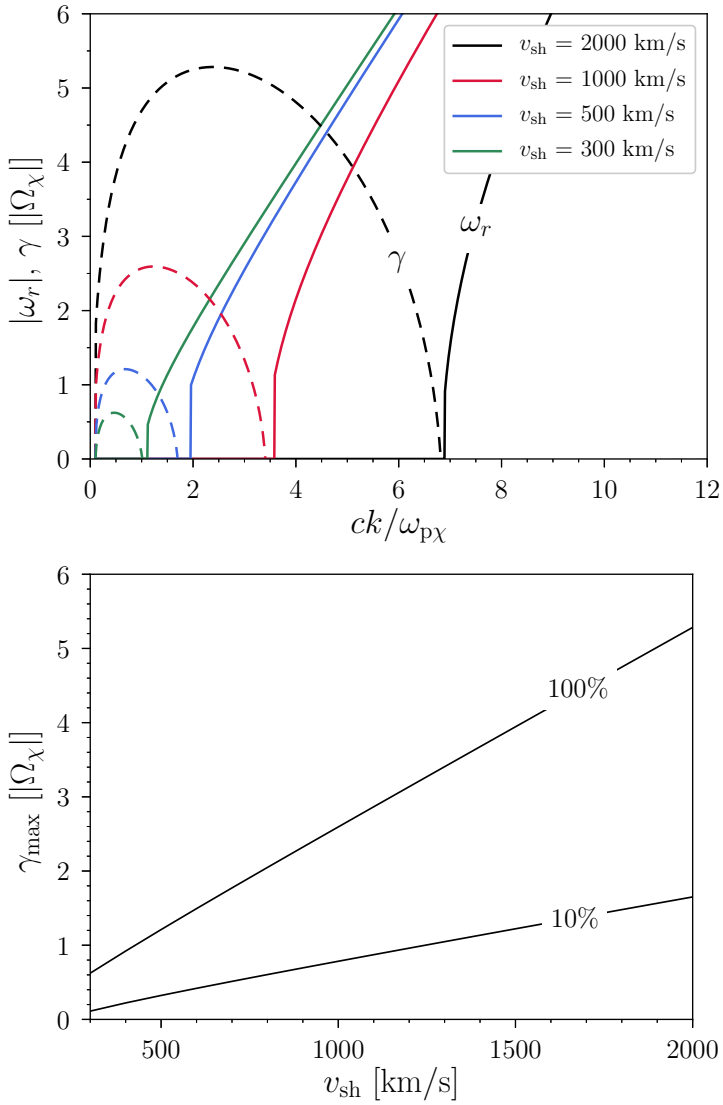

Figure 4.11. Weibel instability in a perpendicular shock. (top) Plot of the real oscillation frequency (solid lines) and the growth rate (dashed lines) of the right/left-hand EM wave as a function of wave vector, assuming $\rho_{\rm DM} = \rho_\chi = 1$ GeV/cm^3. We note that one feature of Weibel instability is an aperiodic wave, i.e., $\omega_r \simeq 0$, which explains the vanishingly small values of ω_r for the unstable k modes. (bottom) The maximum growth rate as a function of shock speed. The numbers on the curves denote $\rho_\chi/\rho_{\rm DM}$, assuming $\rho_{\rm DM} = 1$ GeV/cm^3.

Sec. 4.4.1.

The numerical solution of Eq. (4.20) is shown in Fig. 4.11 with the assumption $B_0 = 10\ \mu$G and $n_{{\rm post},i} = 1$ cm^{-3}. Both EM helicities have the same form of the dispersion relation. In the left panel of Fig. 4.11, we show $|\omega_r|$ and γ as a function of $ck/\omega_{p\chi}$ for various $v_{\rm sh}$, assuming

$\rho_{\rm DM} = \rho_\chi = 1$ GeV/cm^3. Among the unstable k modes, we find $\omega_r \simeq 0$. This indicates that the excited EM waves (left- and right-handed) are aperiodic and they barely propagate in space. The superposition of both helicities with the same phase then gives linearly polarized EM waves with $\omega_r \simeq 0$, which agrees with the features of the EM waves driven by the Weibel instability. We note that all curves of γ eventually drop to zero or negative values as $k \to 0$ due to the fact that the free energy driving the instability is contained in the term $\left(V_0^2/v_{{\rm th},\chi}^2\right)[1+\xi_s Z(\xi_s)]$, which vanishes as $k \to 0$ ($\xi_s \to \infty$). In the right panel, we show the maximum growth rates as a function of $v_{\rm sh}$ with various values of $\rho_\chi/\rho_{\rm DM}$ assuming $\rho_{\rm DM} = 1$ GeV/cm^3. The maximum growth rate $\gamma_{\rm max}$ is an increasing function of $v_{\rm sh}$ and $\rho_\chi/\rho_{\rm DM}$, and it is approximately proportional to $V_0/v_{{\rm th},\chi}$. For the optimal scenario where $\rho_\chi/\rho_{\rm DM} = 100\%$, we find $\gamma \gtrsim |\Omega_\chi|$ for all shock speeds in the Sedov-Taylor phase ($v_{\rm sh} \gtrsim 200$ km/s).

We emphasize that while $\omega_r/k \to 0$ among the unstable k modes shown in the left panel of Fig. 4.11, the result does not suggest the kinetic waves in the plasma have zero phase speed. For the unstable EM fluctuations excited by the instability, the linear stability analysis performed here only contains the information about γ and ω_r at a given k mode as they are created. It does not provide information regarding the evolution and propagation of the fluctuations during the late stage of the instability. On the other hand, the kinetic plasma waves are the stable collective oscillations from tiny perturbations on an equilibrium plasma. Therefore, the phase speed of the growing fluctuations from instabilities should be distinguished from the phase speed of the kinetic waves propagating in the equilibrium plasma.

4.4.3 Condition for sweeping up mDM

We have shown that a mDM beam can drive the firehose and Weibel electromagnetic plasma instabilities, assuming a simplified model for the downstream plasma and magnetic field in a SNR. If the maximum growth rate is $\gamma_{\rm max}$, then the instability will be saturated in a timescale $\approx \gamma_{\rm max}^{-1}$. Consequently, for a shock of speed $v_{\rm sh}$, the saturation length in the downstream plasma is $\approx 3 v_{\rm sh}\gamma_{\rm max}^{-1}/4$, where the mDM beam velocity is $V_0 = 3v_{\rm sh}/4$. That is, it takes about a distance

scale of $3v_{\rm sh}\gamma_{\rm max}^{-1}/4$ to saturate the instability and make the mDM velocity distribution isotropic in the downstream frame. Since the majority of shocked ISM gas resides in the outermost shell with thickness $\approx 0.1R_{\rm sh}$ [198], we require that $3v_{\rm sh}\gamma_{\rm max}^{-1}/4 < 0.1R_{\rm sh}$ in order for the mDM to be swept up and isotropized in an expanding SNR.

The colored bands in Fig. 4.1 show the resulting condition on the mDM charge and mass. We take the downstream ion density as $n_{{\rm post},i} = 1\ {\rm cm}^{-3}$ and the ambient mDM mass density as $\rho_\chi = 1\ {\rm GeV/cm}^3$. Above the orange (green) band, the mDM charge fraction $|q_\chi/e|$ is sufficiently large for it to drive a plasma instability and be swept up by the supernova in a parallel (perpendicular) shock. The upper and lower boundaries of each band are for $v_{\rm sh} = 1500\ {\rm km/s}$ and $300\ {\rm km/s}$, respectively, where we have used the appropriate value of the remnant radius $R_{\rm sh}$ for that shock speed (see Fig. 4.3).

4.5 Implications

In this section, we turn to some consequences of the mDM interaction in the SNR. Having seen that mDM can be swept up for sufficiently large charge fractions, we next discuss the eventual fate of the mDM velocity distribution once the shocked ISM gas undergoes adiabatic decompression and the supernova shock dies out. We comment on the possibility and challenges of generating a Fermi-accelerated mDM component in Sec. 4.5.2. Finally, the total mass swept up by the SNR can increase if mDM is accounted for, and we discuss how this could impact the Sedov-Taylor phase.

4.5.1 Adiabatic decompression and the mDM velocity distribution

When the mDM-driven plasma instabilities occur, a significant fraction of the ordered kinetic energy of the mDM beam is transferred to the disordered kinetic energy of the mDM particles moving isotropically. The mDM is "shocked" and heated up. For supernova shocks at the early and mid stages of the Sedov-Taylor phase, the swept-up mDM has bulk velocity (in the Milky Way frame) and velocity dispersion that are significantly larger than $v_{{\rm th},\chi} \approx 220\ {\rm km/s}$,

which would apparently have a large impact on terrestrial dark matter detection. However, it is not easy for these shocked mDM particles to stream out directly from the remnant for the following reason. After the instabilities have saturated, the mDM particles continue to scatter on the EM waves and are trapped in the supernova remnant. Consequently, we expect that the trapped mDM particles lose energy through adiabatic decompression as the shocked ISM gas returns to the ambient ISM state. At the same time, the bulk of the shocked mDM would slow down with the remnant and eventually come to rest in the Milky Way frame after the supernova shock has died out.

We first consider the effect of adiabatic decompression on the mDM velocity dispersion in the downstream frame. As a simplified model[7], here we assume that (1) all the kinetic energy of the mDM beam measured in the downstream frame is transferred to the heat of random mDM motion, (2) the process is instantaneous, i.e., the growth time is neglected, and (3) the shocked mDM particles follow a Maxwell-Boltzmann distribution after the instabilities have saturated. Then for a group of mDM particles shocked and swept up by the supernova shock wave with speed $v_{\rm sh}$, the resulting velocity dispersion is given as $v'_{{\rm dis},\chi}(v_{\rm sh}) = \sqrt{v^2_{{\rm th},\chi} + 3v^2_{\rm sh}/8}$. (Note that groups of mDM particles entering the shock at different shock speeds will have different velocity dispersion after being swept up. Since the different groups of mDM do not thermalize via Coulomb interactions for the parameters we study in this work, we use *velocity dispersion* here to mean the dispersion for a given group of particles.)

Because the shocked ISM has a higher gas pressure than the ambient pressure, its volume expands. At the same time, the trapped mDM particles lose kinetic energy through adiabatic decompression. If the volume of the shocked ISM gas expands by a factor Λ^{-3}, then each mDM particles' speed is decreased by a factor Λ. That is, for a group of mDM particles swept up by the shock with speed $v_{\rm sh}$, the final velocity dispersion after decompression is given as $v''_{{\rm dis},\chi}(v_{\rm sh}) = \Lambda v'_{{\rm dis},\chi}(v_{\rm sh})$. Here we follow Ref. [243] to specify the decompression factor Λ in

[7]The exact mDM velocity distribution as well as the kinetic energy distribution between the shocked mDM particles and the mDM-driven waves can be obtained from the quasilinear theory or hybrid simulation.

two limits.

Density argument: decompression stops once the shocked ISM gas is returned from its downstream density, ρ_2, to the ambient ISM density, ρ_1. According to the RH condition, $\rho_2 = 4\rho_1$ for a high shock number. Thus, the decompression factor is

$$\Lambda_d = \left(\frac{\rho_2}{\rho_1}\right)^{-1/3} = 4^{-1/3} \approx 0.63. \tag{4.21}$$

Pressure argument: decompression stops once the shocked ISM gas is returned from its downstream pressure, P_2, to the ambient ISM pressure, P_1. With the assumption that the shocked ISM gas is an ideal fluid and expands adiabatically, the decompression factor is

$$\Lambda_p = \left(\frac{P_2}{P_1}\right)^{-1/5} = \left(\frac{5M^2-1}{4}\right)^{-1/5}, \tag{4.22}$$

where $M \equiv v_{\rm sh}/c_{\rm s}$ denotes the Mach number and $c_{\rm s}$ is the ambient ISM sound speed. For ISM temperature $T_1 = 10^4$ K and adiabatic index $\gamma_{\rm a} = 5/3$ for a monatomic gas, the ISM sound speed is $c_{\rm s} = \sqrt{\gamma_{\rm a} T_1/m_i} \approx 12$ km/s.

In Fig. 4.12, we show the effect of adiabatic decompression on the shocked mDM particles. The orange and blue lines in the subplot denote Λ_d and Λ_p, respectively. The decompression effect from the pressure argument is significantly stronger than the effect from the density argument. This is because the downstream pressure ($\sim \rho_1 v_{\rm sh}^2$) is easily larger than the ambient ISM pressure ($\sim \rho_1 c_{\rm s}^2$) by few orders of magnitude for high Mach shocks whereas the downstream density is always approximately 4 times the upstream density. The difference between the two arguments leads to a big contrast to the mDM velocity dispersion. In the main plot, the red dashed line represents the mDM velocity dispersion, $v'_{{\rm dis},\chi}$, for the group of mDM particles entering the shock with the speed $v_{\rm sh}$. The orange and blue lines represent the final velocity dispersion, $v''_{{\rm dis},\chi}$, of the same group of mDM particles that have undergone Λ_d and Λ_p, respectively. Note that $v'_{{\rm dis},\chi}$ always drops $\approx 40\%$ with the density argument whereas it can drop

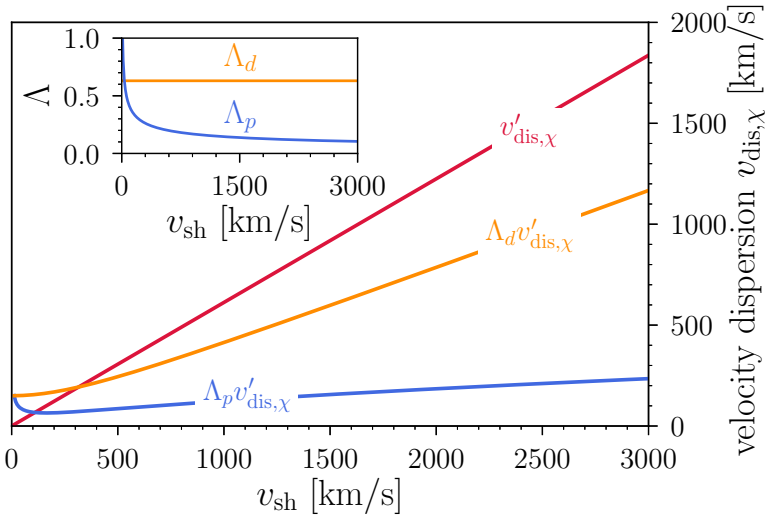

Figure 4.12. The effect of adiabatic decompression on the mDM velocity dispersion, in the frame of the downstream fluid. (main plot) The red dashed line is the velocity dispersion, $v'_{\mathrm{dis},\chi}$, for a group of mDM particles which have isotropized in a shock with speed v_{sh}. Note that v'_{χ} does not include any adiabatic decompression effect. The orange and blue lines are the mDM velocity dispersion after decompression, $v''_{\mathrm{dis},\chi}(v_{\mathrm{sh}}) = \Lambda v'_{\mathrm{dis},\chi}(v_{\mathrm{sh}})$, with Λ given by a density (Λ_d) or pressure (Λ_p) argument, respectively. The actual velocity dispersion after decompression should lie between the orange and blue lines. (inset) Decompression factors Λ_d and Λ_p.

as much as $\gtrsim 80\%$ with the pressure argument for shocks in the Sedov-Taylor phase. A more realistic $v''_{\mathrm{dis},\chi}$ within a galactic supernova remnant should lie between the orange and blue lines.

The mDM particles do not just free-stream out from the supernova remnant after adiabatic decompression has stopped. In the case of a quasiparallel shock, the mDM particles continue to scatter on the magnetic irregularities driven by the mDM beam or cosmic-ray protons. In the case of a quasiperpendicular shock, the mDM particles are confined in the downstream or near the shock front since the ordered upstream magnetic fields prohibit mDM streaming more than one Larmor radius. (Note that the latter case is independent of whether or not the trapping comes from mDM scattering with mDM-driven plasma waves.) In both scenarios, the shocked mDM particles remain trapped in the supernova remnant and the bulk velocity would slow down with the remnant. As a result, the velocity distribution of the shocked mDM in the Milky Way frame,

dN/dv_χ, is given as

$$\frac{1}{n_\chi}\frac{dN}{dv_\chi} = \int_{300\text{ km/s}}^{10^4\text{ km/s}} 4\pi R_{\rm sh}^2 \frac{dR_{\rm sh}}{dv_{\rm sh}} F_{\rm shell}\left(v_\chi, v_{\rm sh}\right) dv_{\rm sh}, \tag{4.23}$$

where we have normalized by the ambient mDM number density, n_χ, we have used

$$4\pi R_{\rm sh}^2 dR_{\rm sh}/dv_{\rm sh} = 2.94 E_{\rm SN}\rho_{\rm ISM}^{-1} v_{\rm sh}^{-3}, \tag{4.24}$$

and

$$F_{\rm shell}\left(v_\chi, v_{\rm sh}\right) = \frac{4}{\sqrt{\pi}}\frac{v_\chi^2}{(v''_{{\rm dis},\chi})^3} e^{-v_\chi^2/(v''_{{\rm dis},\chi})^2}. \tag{4.25}$$

Here as a conservative estimate in Eq. (4.23), we only consider the supernova shock speed from 10^4 km/s to 300 km/s, which is the region where mDM can drive plasma instabilities and be shocked in the case of 100% dark matter content as mDM. (For $v_{\rm sh} \lesssim 300$ km/s, mDM beam does not drive EM plasma instabilities, as we have shown in Sec. 4.4.)

In Fig. 4.13, we show the velocity distribution in the cases with and without adiabatic decompression. The red curve does not include any decompression which means $v''_{{\rm dis},\chi} = v'_{{\rm dis},\chi}$. The orange and blue curves include adiabatic decompression with the density argument and the pressure argument, respectively. The black dashed curve is for mDM that has not interacted with any SNR. The tail of the red curve comes from the swept-up mDM in the early phase of the Sedov-Taylor phase where the shock speed is high. It does not result from the DSA mechanism. The decompression from density argument only decreases the tail of high-speed particles moderately since the shocked ISM density is only 4 times the ambient ISM density and the bulk of the fluid is not decompressed much. On the other hand, the decompression from the pressure argument can cool down the shocked mDM significantly, even colder than the ambient mDM. We expect that the shocked mDM should lie between these limits. These arguments suggest that, after being shocked and cooled by decompression, the bulk of the mDM velocity distribution ends up qualitatively similar to the initial ambient mDM distribution.

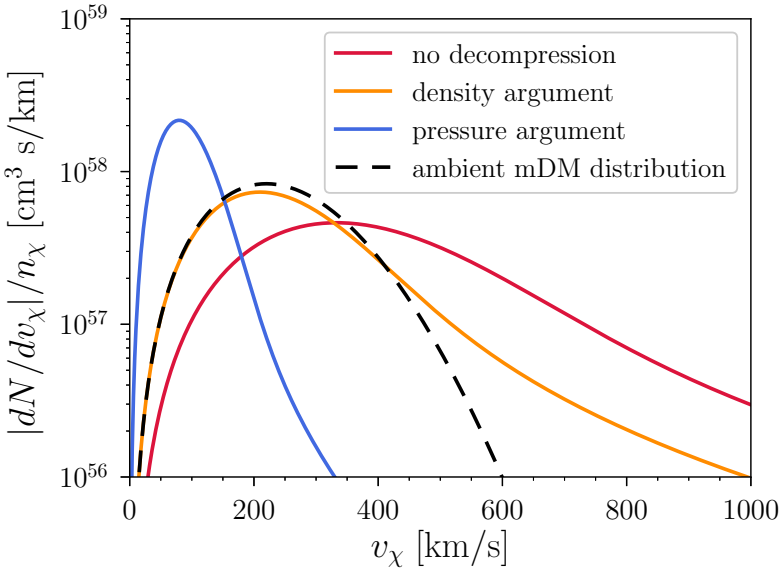

Figure 4.13. The velocity distribution of the shocked mDM in each supernova event. We only consider mDM particles entering the supernova shock of speed between 10^4 km/s and 300 km/s. The black dashed curve is the ambient (unshocked) mDM distribution. While decompression according to the density argument only moderately cools down the shocked mDM, decompression from the pressure argument can make the majority of the shocked mDM colder than the ambient mDM.

4.5.2 Challenges for generating dark cosmic rays

We have shown that mDM can be shocked and swept up by the supernovae. A natural question one might ask is whether mDM also undergoes the DSA process and is Fermi-accelerated to relativistic speeds in the same way cosmic-ray protons are accelerated. Having relativistic mDM particles in the Milky Way would have a significant impact on terrestrial dark matter detection [183, 184]. However, there is no consensus on the flux of Fermi-accelerated mDM in the Milky Way. Reference [184] considers (1) the possibility of getting pre-accelerated mDM from one shock and injecting them into the DSA process in another shock, as well as (2) the possibility that mDM particles with the virial velocity larger than the shock speed can undergo Fermi acceleration in one shock if they are never thermalized with the ISM gas. On the other hand, Ref. [183] assumes that the mDM can be injected into the DSA process in just one shock if the mDM particles have the same rigidity as some of the Fermi-accelerated protons in the

same shock. Because the two works assume very different acceleration processes, the resulting Fermi-accelerated fluxes are incompatible. Nevertheless, there are still several critical issues that must be answered. In this section, we bring up the challenges of getting Fermi-accelerated mDM taking into consideration plasma waves and adiabatic decompression.

The standard acceleration theory utilizes the diffusion-convection equation in a quasi-parallel shock. It requires that (1) the accelerated particle speed be much higher than the shock speed and (2) the phase space distribution of the accelerated particles in the local fluid frame is isotropic. Then in the steady state, the diffusion-convection equation gives the isotropic part of the phase space distribution in the downstream, f_+, in terms of the isotropic part of the phase space distribution in the far upstream, f_-, in the following form [206, 244, 245]

$$f_+(p) = sp^{-s}\int^p dp' f_-\left(p'\right) p'^{s-1} + C/p^s, \tag{4.26}$$

where $s = 3r/(r-1)$ decides the slope of the Fermi-accelerated spectrum and $r \approx 4$ denotes the compression ratio of the flow given by the Rankine-Hugoniot conditions. The first term on the right-hand side (rhs) of Eq. (4.26) provides the spectrum of the Fermi-accelerated particles in the downstream when the preexisting energetic particles in the far upstream are advected through the shock front and undergo the DSA process. The second term represents the spectrum of the particles that are directly injected from the downstream particles into the DSA process. The constant C is determined by matching the spectrum of the injected particles at the supra-thermal regime[8] with the power-law spectrum.

In Ref. [184], the authors use the first term on the right-hand side of Eq. (4.26) to obtain a Fermi-accelerated mDM spectrum. The proposed physical origins are the following: (1) the mDM with $m_\chi/q_\chi^2 < 3\times 10^6\,\mathrm{GeV}/e^2$ are thermalized with ISM. To Fermi-accelerate them, two shocks are required. The moving magnetic fields near the shock front of the first supernova

[8]Supra-thermal regime is the transition zone where the distribution of the downstream thermal particles is joined to the power-law distribution of the Fermi-accelerated particles.

shock reflect mDM particles and accelerate them to the shock speed. Among the reflected mDM, all the particles moving faster than 200 km/s can then undergo DSA in a second shock with $v_{\rm sh} = 200$ km/s. This process is referred as *two-stage injection* in Ref. [184]. (2) The mDM with $m_\chi/q_\chi^2 > 3\times10^6\,{\rm GeV}/e^2$ are not thermalized with ISM and therefore have the velocity of the Milky Way virial velocity (taken as 220 km/s). On encountering a shock with $v_{\rm sh} = 200$ km/s, all mDM particles are Fermi-accelerated because they move faster than the shock. Here we revisit both mechanisms, taking into consideration plasma waves.

We first review the idea of particle reflection at the shock front from the standard cosmic ray acceleration theory. It was known that a fraction of upstream protons may be reflected by the potential barrier at the shock front due to the shock reformation [205, 246, 247]. However, heavy ions with mass-to-charge ratio larger than protons are not reflected by the shock barrier; instead they penetrate to the downstream [248]. Since the mDM we study here has mass-to-charge ratio significantly larger than the ratio of protons, we also expect mDM impinge to the downstream directly, which represents the first difficulty for the two-stage mechanism. The mDM particles flow into the downstream fluid and are swept up by the SNR. After that, they likely still remain trapped in the downstream fluid due to the wave-particle scattering. They will undergo adiabatic decompression and slow down along with the expanding SNR. The number density of the energetic mDM (say with speeds significantly higher than 200 km/s in the Milky Way frame) from the first shock will be reduced after taking into consideration these effects, as shown in Fig. 4.13.

This leads to the second challenge of getting DSA in the two-stage injection process. For the second supernova shock with $v_{\rm sh} = 200$ km/s, the first term on the rhs of Eq. (4.26) operates exclusively to preaccelerated particles with speeds *at least* several thousand km/s. Such high speeds can be achieved only if mDM enters the first supernova shock at the free-expansion phase or the very early stage of the Sedov-Taylor phase so that the catastrophic energy loss from the adiabatic decompression is overcome. Consequently, the total number of these high-speed mDM from the first supernova shock which might undergo standard acceleration in the second

shock would certainly be several orders of magnitude lower than the total number of the mDM particles covered within $R_{\rm sh}\,(200\ {\rm km/s})$ of the first supernova shock. Taking all these issues into consideration, we find it challenging to get Fermi-accelerated mDM from multiple supernova shocks.

The direct injection of the downstream mDM particles to the DSA process is another possibility to get dark cosmic rays, as proposed in Refs. [183, 184]. However, studying this mechanism from first principles is a difficult problem, and generally simulations are required to determine the constant C in Eq. (4.26). (Ref. [184] assumes an $\mathcal{O}(1)$ injection fraction.) There are multiple stages to obtaining the injection rate. Here we only qualitatively discuss three challenges/issues, while much more work is required before obtaining a self-consistent picture of the mDM injection rate. The very first thing to figure out is the exact mDM velocity distribution in the downstream, since it controls the number of downstream mDM particles that can return to upstream after they have passed the shock for their first time. In this work, we merely use linear stability analysis to understand the timescale for mDM to be swept up by the SNR. The mDM velocity distribution can be obtained by utilizing quasilinear theory, which describes the phase space evolution and the beam relaxation back to a marginally stable state [249].

The second challenge is understanding the dynamics of the mDM particles that return back to the upstream from the downstream. In the case of proton cosmic ray acceleration, it is believed that the protons returning to the upstream from the downstream (or reflected at the shock front back upstream) scatter on self-generated Alfvén waves propagating along the ambient magnetic fields in the (quasi)parallel shock. Those protons are then isotropized in the upstream frame and can return downstream again. While the same strategy can be applied to mDM, it is not clear how the injection process is altered due to the ultraslow instabilities of mDM particles compared to that of cosmic-ray protons.

The third issue is that the Alfvén waves excited in the upstream will eventually cross the shock front and trap a fraction of mDM particles trying to escape to the upstream. This effect reduces the odds that particles can gain energy from multiple crossings at the shock front and be

injected to DSA process [201, 250]. Different velocity distribution functions will lead to different probabilities that particles can evade the trapping. It is therefore important to understand how the downstream mDM with a non-Maxwellian distribution responds to the particle-trapping from the upstream Alfvén waves. Addressing all these questions is needed to determine the normalization and slope of any Fermi-accelerated mDM component.

4.5.3 Sedov-Taylor phase of the supernova remnant

If the mDM particles are swept up by the supernova remnant, the total mass density of the swept-up fluid, ρ_0, is increased. Then we expect the shock wave to propagate slower and travel a shorter distance than the case in which only the ISM is swept up. In principle, we can determine this slowing-down effect by measuring $R_{\rm sh}$, $\dot{R}_{\rm sh}$ and $\ddot{R}_{\rm sh}$ of the younger Type Ia supernovae, which are at the early stage of the Sedov-Taylor phase and where the dynamics of expansion is predominantly governed by the swept-up mass. We can infer the effect of deceleration from the swept-up mDM once the E/ρ_0 is obtained, where E is the initial kinetic energy of the ejecta.

A simple estimate shows that it is not easy to make an observable prediction, however. The typical ISM mass density is $\rho_{\rm ISM} \sim 1\ {\rm GeV/cm^3}$. In the optimal case where mDM constitutes all of the DM, the mDM mass density at few kpc away from the Galactic Center (GC) is also $\rho_\chi \sim 1\ {\rm GeV/cm^3}$. Thus, the total swept-up mass $\rho_0 = \rho_{\rm ISM} + \rho_\chi$ is at most a few times larger. On the other hand, the kinetic energy of the ejecta from a Type Ia supernova is approximately $1 - 2 \times 10^{51}$ erg – which is also uncertain by a factor a few. With these uncertainties from the mass density and the ejecta kinetic energy, it is challenging to quantify the effect of deceleration from the swept-up mDM or make any constraints on the local mDM density. Lastly, we note that while the volume within a few hundred pc from GC has $\rho_{\rm DM} > 10\ {\rm GeV/cm^3}$ and is an ideal site to test the deceleration effect, there are no observed supernovae in that region within the past 1000 years. The lack of events is due to the fact that the molecular clouds in the central molecular zone (inner ~ 200 pc) is subject to disruptive shear which suppresses the star formation rate [251].

4.6 Conclusion

We have shown that it is possible for mDM to be swept up by supernova remnants and to become isotropized in the expanding fluid through plasma instabilities. A few of the most representative plasma waves and instabilities are considered: ion-acoustic, Langmuir, and lower-hybrid wave instabilities of electrostatic waves, and beam-firehose and Weibel instabilities of electromagnetic waves. While there is a tremendous amount of free energy from the relative motion between the ambient mDM and the supernova remnants, we find that the electrostatic waves are never excited due to the fact that mDM with $|q_\chi|/m_\chi \ll e/m_p$ is not able to drive the growth fast enough to overcome ion Landau damping. On the other hand, electromagnetic waves can be excited by mDM because the wave frequency is much smaller than the ion cyclotron frequency and thus the ion cyclotron damping is avoided.

We find that for $|q_\chi/m_\chi| \gtrsim 10^{-13} e/\mathrm{MeV}$, mDM can be isotropized in the expanding supernova remnants at the Sedov-Taylor phase by driving electromagnetic beam-firehose and Weibel instabilities in parallel and perpendicular shocks, respectively, provided that mDM constitutes all the DM content in the Milky Way. If mDM makes up only a fraction of the total DM, then mDM might not able to drive electromagnetic plasma waves at the late stage of the Sedov-Taylor phase since the mDM beam velocity threshold for the instability increases as the density of mDM decreases.

Finally, we emphasize that the plasma waves prevent the majority of the shocked mDM particles from free-streaming out the supernova remnant via wave-particle interactions. Moreover, the mDM particles undergo significant energy loss from adiabatic decompression as the remnant expands. Both effects play important roles in the final velocity distribution of the shocked mDM in the Milky Way, and our analysis suggests that the bulk of the shocked mDM ends up with a velocity distribution qualitatively similar to the unshocked distribution. Further study of mDM wave-particle interactions is needed to determine to what extent mDM undergoes Fermi-acceleration and its subsequent Galactic dynamics.

4.7 Acknowledgments

We thank Tsang Keung Chan, Hope How-Huan Chen, Daniel Dubin, David Dunsky, Dušan Kereš, Robert Lasenby, Diego Redigolo and Kurt Thompson for valuable discussions. We especially appreciate the guidance on plasma physics and cosmic rays from Patrick Diamond and Mikhail Malkov. J.T.L. is supported by an Government Scholarship to Study Abroad from Taiwan government. T.L. is supported by an Alfred P. Sloan Research Fellowship and Department of Energy (DOE) grant no. DE-SC0019195.

This chapter is, in full, a reprint of material from published work done in collaboration with Tongyan Lin, as it appears in the Physical Review D 101 (10), 103034. The dissertation author was the primary investigator and author of this material.

4.A Review of unmagnetized linear response function

In this Appendix, we follow closely the derivations in Refs. [230, 252] to briefly review the dispersion relation for an unmagnetized plasma with no magnetic fields present. The derivation of the linear response for a magnetized plasma is similar, and can be found in many plasma physics books, e.g., Refs [230, 237, 252, 253].

We start with the collisionless Vlasov-Maxwell equations

$$\begin{aligned} \left(\frac{\partial}{\partial t}+\mathbf{v}\cdot\nabla+\frac{q_j}{m_j}\mathbf{E}\cdot\frac{\partial}{\partial \mathbf{v}}\right) f_j(\mathbf{x},\mathbf{v},t)=0, \qquad & \text{Vlasov equation,} \\ \nabla\cdot\mathbf{E}=\sum_j 4\pi q_j\int f_j(\mathbf{x},\mathbf{v},t)\,d^3\mathbf{v}, \qquad & \text{Gauss Law,} \end{aligned} \tag{4.27}$$

where $\mathbf{E}=\mathbf{E}(\mathbf{x},t)$ is the electric field, and q_j, and m_j are the charge and mass of species j. In the present analysis, we consider longitudinal waves with small amplitude propagating through a system near equilibrium. We consider a spatially homogeneous plasma with no external electric and magnetic fields, i.e., $\mathbf{E}_0=\mathbf{B}_0=0$. Define a normalized particle distribution function of the

species j as

$$F_j(\mathbf{x},\mathbf{v},t) \equiv \frac{f_j(\mathbf{x},\mathbf{v},t)}{n_{0j}}, \tag{4.28}$$

where $f_j(\mathbf{x},\mathbf{v},t)$ is the density in $(\mathbf{x},\mathbf{v})$ phase space and n_{0j} is the ambient number density. Both $\mathbf{E}(\mathbf{x},t)$ and $F_j(\mathbf{x},\mathbf{v},t)$ can be written as the sum of their equilibrium values plus small perturbation terms:

$$\begin{aligned} \mathbf{E}(\mathbf{x},t) &\to \delta\mathbf{E}(\mathbf{x},t), \\ F_j(\mathbf{x},\mathbf{v},t) &\to F_{0j}(\mathbf{v}) + \delta F_j(\mathbf{x},\mathbf{v},t). \end{aligned} \tag{4.29}$$

The analysis is greatly simplified if we apply the Fourier-Laplace transform on $\delta\mathbf{E}$ and δF_j,

$$\begin{aligned} \delta\mathbf{E}(\mathbf{x},t) &= \int d^3\mathbf{k}\, e^{i\mathbf{k}\cdot\mathbf{x}} \int_{\omega_0-i\infty}^{\omega_0+i\infty} \frac{d\omega}{2\pi i} e^{\omega t}\, \delta\tilde{\mathbf{E}}(\mathbf{k},\omega), \\ \delta F_j(\mathbf{x},\mathbf{v},t) &= \int d^3\mathbf{k}\, e^{i\mathbf{k}\cdot\mathbf{x}} \int_{\omega_0-i\infty}^{\omega_0+i\infty} \frac{d\omega}{2\pi i} e^{\omega t}\, \delta\tilde{F}_j(\mathbf{k},\mathbf{v},\omega), \end{aligned} \tag{4.30}$$

where $\omega_0 = \mathrm{Re}(\omega)$ is chosen large enough so that the reverse integrals $\int_0^\infty \delta\tilde{\mathbf{E}}(\mathbf{k},\omega)\exp(-\omega t)\,dt$ and $\int_0^\infty \delta\tilde{F}_j(\mathbf{k},\mathbf{v},\omega)\exp(-\omega t)\,dt$ converge. Rewriting the linearized Vlasov-Maxwell equations in $(\mathbf{k},\omega)$ space, then

$$-i(\omega - \mathbf{k}\cdot\mathbf{v})\,\delta\tilde{F}_j(\mathbf{k},\mathbf{v},\omega) = \frac{q_j}{m_j}\delta\tilde{\mathbf{E}}\cdot\frac{\partial F_{0j}(\mathbf{v})}{\partial\mathbf{v}}, \tag{4.31}$$

$$i\mathbf{k}\cdot\delta\tilde{\mathbf{E}}(\mathbf{k},\omega) = \sum_j 4\pi n_{0j} q_j \int \delta\tilde{F}_j(\mathbf{k},\mathbf{v},\omega)\,d^3\mathbf{v}. \tag{4.32}$$

It is straightforward to show from Eqs. (4.31) and (4.32) that

$$i\mathbf{k}\cdot\delta\tilde{\mathbf{E}}(\mathbf{k},\omega)\left[1 + \sum_j \frac{\omega_{\mathrm{p}j}^2}{k^2}\int \frac{\mathbf{k}\cdot\partial F_{0j}(\mathbf{v})/\partial\mathbf{v}}{\omega - \mathbf{k}\cdot\mathbf{v}}\,d^3\mathbf{v}\right] = 0, \tag{4.33}$$

where $\omega_{\mathrm{p}j}^2 = 4\pi n_{0j} q_j^2/m_j$. Equation (4.33) applies for the longitudinal component of $\delta\tilde{\mathbf{E}}$. The

requirement for a nontrivial solution of Eq. (4.33) is

$$D(\mathbf{k},\omega) \equiv 1 + \sum_j \frac{\omega_{\mathrm{p}j}^2}{k^2} \int \frac{\mathbf{k}\cdot\partial F_{0j}(\mathbf{v})/\partial \mathbf{v}}{\omega - \mathbf{k}\cdot\mathbf{v}}\, d^3\mathbf{v} = 0, \tag{4.34}$$

Equation (4.34) is the definition of the unmagnetized plasma dielectric function, $D(\mathbf{k},\omega)$, and the associated dispersion relation.

4.A.1 Plasma dispersion function

In many plasma environments, each species is modeled as a gas in thermal equilibrium. It is therefore useful to further simplify the dispersion relation in Eq. (4.34). A drifting Maxwellian gas of species j has the distribution function given by

$$F_{0j}(\mathbf{v}) = \pi^{-3/2}\, v_{\mathrm{th},j}^{-3} \exp\left(-\frac{\left(\mathbf{v}-\mathbf{V}_{0j}\right)^2}{v_{\mathrm{th},j}^2} \right), \tag{4.35}$$

where $\mathbf{V}_{0j}$ and $v_{\mathrm{th},j} = \sqrt{2T_j/m_j}$ are the drift velocity and the thermal velocity of the species j, respectively. Using Eq. (4.35) in Eq. (4.34), the dispersion relation of the unmagnetized plasma is expressed as

$$0 = D(\mathbf{k},\omega) = 1 + \sum_j \frac{2\omega_{\mathrm{p}j}^2}{k^2 v_{\mathrm{th},j}^2} \left[1 + \xi_j Z\left(\xi_j\right) \right], \tag{4.36}$$

where $\xi_j = \left(\omega - \mathbf{k}\cdot\mathbf{V}_{0j}\right)/k v_{\mathrm{th},j}$ and

$$Z\left(\xi_j\right) \equiv \frac{1}{\sqrt{\pi}} \int_{-\infty}^{\infty} \frac{e^{-x^2}}{x-\xi_j}\, dx. \tag{4.37}$$

Here we examine some important properties of the plasma dispersion function widely used in the literature of plasma physics. The asymptotic expansion of $Z\left(\xi_j\right)$ for small and large values of $|\xi_j|$ are given as [254]

$$Z\left(\xi_j\right) = i\sqrt{\pi}\exp\left(-\xi_j^2\right) - 2\xi_j + \frac{4}{3}\xi_j^3 - \frac{8}{15}\xi_j^5 + \cdots, \qquad \text{for } |\xi_j| < 1, \tag{4.38}$$

and

$$Z\left(\xi_j\right) = i\sqrt{\pi}\exp\left(-\xi_j^2\right) - \frac{1}{\xi_j} - \frac{1}{2\xi_j^3} - \frac{3}{4\xi_j^5} + \cdots \qquad \text{for } |\xi_j| > 1. \tag{4.39}$$

Also, differentiating $Z\left(\xi_j\right)$ with respect to ξ_j and applying integration by parts, we obtain

$$Z'\left(\xi_j\right) = \frac{-2}{\sqrt{\pi}} \int_{-\infty}^{\infty} \frac{xe^{-x^2}}{x-\xi_j}\, dx = -2\left[1 + \xi_j Z\left(\xi_j\right)\right]. \tag{4.40}$$

As an example to show the application of Eqs. (4.36), (4.38) and (4.39), consider Langmuir waves propagating through a neutral electron-proton plasma at equilibrium with zero drift velocities. Landau damping is avoided if we require that $\omega_r/k \gg v_{\text{th},e} \gg v_{\text{th},i}$, i.e., $|\xi_e| \gg 1$ and $|\xi_i| \gg 1$. The dispersion relation in Eq. (4.36) becomes

$$\begin{aligned} 0 = D\left(\mathbf{k},\omega\right) &= 1 - \frac{\omega_{\text{p}e}^2}{\omega_r^2} - 3k^2\lambda_{\text{D}e}^2\frac{\omega_{\text{p}e}^4}{\omega_r^4} - \frac{\omega_{\text{p}i}^2}{\omega_r^2} + \cdots \\ &\approx 1 - \frac{\omega_{\text{p}e}^2}{\omega_r^2} - 3k^2\lambda_{\text{D}e}^2\frac{\omega_{\text{p}e}^4}{\omega_r^4} + \mathscr{O}\left(\omega_{\text{p}e}^6\right), \end{aligned} \tag{4.41}$$

where $\lambda_{\text{D}e} \equiv \sqrt{T_e/4\pi n_e e^2}$ is the electron Debye screening length. The ion contribution is neglected because $\omega_{\text{p}e}^2 \gg \omega_{\text{p}i}^2$ in the neutral plasma. In the limit $k^2\lambda_{\text{D}e}^2 \ll 1$ where electron Landau damping is avoided, we obtain the dispersion relation for stable Langmuir waves,

$$\omega_r = \omega_{\text{p}e}\sqrt{1 + 3k^2\lambda_{\text{D}e}^2}. \tag{4.42}$$

Note that the Landau damping contribution comes from the term $i\sqrt{\pi}\exp\left(-\xi_j^2\right)$ in Eqs. (4.38) and (4.39). In the regime where $\xi_j \sim 1$, the exponential term is not negligible, and the waves suffer strong Landau damping from the species j. To get the damping rate, one can numerically solve Eq. (4.36) or use the technique shown in the following subsection.

4.A.2 Weakly damped or growing waves

In this section, we provide some useful results on the growth rate for the weakly damped or growing waves. Expanding $D(\mathbf{k}, \omega_r + i\gamma)$ in the limit $|\gamma/\omega_r| \ll 1$, we obtain

$$0 = D(\mathbf{k}, \omega_r + i\gamma) = D_{\mathrm{Re}}(\mathbf{k}, \omega_r) + iD_{\mathrm{Im}}(\mathbf{k}, \omega_r) + i\gamma \frac{\partial D_{\mathrm{Re}}(\mathbf{k}, \omega_r)}{\partial \omega_r}, \tag{4.43}$$

where we have separated $D(\mathbf{k}, \omega_r + i\gamma)$ into real and imaginary parts and assumed higher order terms are small. The real part of Eq. (4.43), $D_{\mathrm{Re}}(\mathbf{k}, \omega_r) = 0$, determines the real oscillation frequency. Setting the imaginary part to zero then gives the damping or growing rate,

$$\gamma = \frac{-D_{\mathrm{Im}}(\mathbf{k}, \omega_r)}{\partial D_{\mathrm{Re}}(\mathbf{k}, \omega_r)/\partial \omega_r}, \tag{4.44}$$

where $\gamma < 0$ and $\gamma > 0$ correspond to damping and growing waves, respectively.

On the other hand, the dielectric function $D(\mathbf{k}, \omega_r + i\gamma)$ can be directly decomposed into its real and imaginary components by utilizing the Plemelj formula,

$$\left.\frac{1}{\omega_r - \mathbf{k}\cdot\mathbf{v} + i\gamma}\right|_{|\gamma| \ll \omega_r} = \mathscr{P}\frac{1}{\omega_r - \mathbf{k}\cdot\mathbf{v}} - i\pi\delta(\omega_r - \mathbf{k}\cdot\mathbf{v}), \tag{4.45}$$

with $\mathscr{P}$ denoting the Cauchy principle value. We obtain

$$D_{\mathrm{Re}}(\mathbf{k}, \omega_r) = 1 + \sum_j \frac{\omega_{\mathrm{p}j}^2}{k^2}\, \mathscr{P}\int \mathbf{k}\cdot\frac{\partial F_{0j}(\mathbf{v})}{\partial \mathbf{v}}\frac{1}{\omega_r - \mathbf{k}\cdot\mathbf{v}} d^3\mathbf{v}, \tag{4.46a}$$

$$D_{\mathrm{Im}}(\mathbf{k}, \omega_r) = -\pi\sum_j \frac{\omega_{\mathrm{p}j}^2}{k^2}\int \mathbf{k}\cdot\frac{\partial F_{0j}(\mathbf{v})}{\partial \mathbf{v}}\,\delta(\omega_r - \mathbf{k}\cdot\mathbf{v})\, d^3\mathbf{v}. \tag{4.46b}$$

Bibliography

[1] A. M. Ghez, S. Salim, S. D. Hornstein, A. Tanner, M. Morris, E. E. Becklin and G. Duchene, *Stellar orbits around the galactic center black hole*, *Astrophys. J.* **620** (2005) 744 [astro-ph/0306130].

[2] O. Shemmer, H. Netzer, R. Maiolino, E. Oliva, S. Croom, E. Corbett and L. di Fabrizio, *Near infrared spectroscopy of high redshift active galactic nuclei. 1. A Metallicity-accretion rate relationship*, *Astrophys. J.* **614** (2004) 547 [astro-ph/0406559].

[3] E. Bañados, B. P. Venemans, R. Decarli, E. P. Farina, C. Mazzucchelli, F. Walter, X. Fan, D. Stern, E. Schlafly, K. C. Chambers, H. W. Rix, L. Jiang, I. McGreer, R. Simcoe, F. Wang, J. Yang, E. Morganson, G. De Rosa, J. Greiner, M. Baloković, W. S. Burgett, T. Cooper, P. W. Draper, H. Flewelling, K. W. Hodapp, H. D. Jun, N. Kaiser, R. P. Kudritzki, E. A. Magnier, N. Metcalfe, D. Miller, J. T. Schindler, J. L. Tonry, R. J. Wainscoat, C. Waters and Q. Yang, *The Pan-STARRS1 distant $z > 5.6$ quasar survey: more than 100 quasars within the first Gyr of the universe*, *Astrophys. J. Suppl.* **227** (2016) 11 [1608.03279].

[4] Y. Matsuoka, K. Iwasawa, M. Onoue, N. Kashikawa, M. A. Strauss, C.-H. Lee, M. Imanishi, T. Nagao, M. Akiyama, N. Asami, J. Bosch, H. Furusawa, T. Goto, J. E. Gunn, Y. Harikane, H. Ikeda, T. Izumi, T. Kawaguchi, N. Kato, K. Kikuta, Satoshi Kohno, Y. Komiyama, S. Koyama, R. H. Lupton, T. Minezaki, S. Miyazaki, H. Murayama, M. Niida, A. J. Nishizawa, A. Noboriguchi, M. Oguri, Y. Ono, M. Ouchi, P. A. Price, H. Sameshima, A. Schulze, J. D. Silverman, N. Sugiyama, P. J. Tait, M. Takada, T. Takata, M. Tanaka, J.-J. Tang, Y. Toba, Y. Utsumi, S.-Y. Wang and T. Yamashita, *Subaru High-z Exploration of Low-luminosity Quasars (SHELLQs). X. Discovery of 35 Quasars and Luminous Galaxies at* $5.7 \leq z \leq 7.0$, *Astrophys. J.* **883** (2019) 183.

[5] F. Wang, J. Yang, X. Fan, X.-B. Wu, M. Yue, J.-T. Li, F. Bian, L. Jiang, E. Bañados, J.-T. Schindler, J. R. Findlay, F. B. Davies, R. Decarli, E. P. Farina, R. Green, J. F. Hennawi, Y.-H. Huang, C. Mazzuccheli, I. D. McGreer, B. Venemans, F. Walter, S. Dye, B. W. Lyke, A. D. Myers and E. Haze Nunez, *Exploring Reionization-era Quasars. III. Discovery of 16 Quasars at* $6.4 \lesssim z \lesssim 6.9$ *with DESI Legacy Imaging Surveys and the UKIRT Hemisphere Survey and Quasar Luminosity Function at* $z \sim 6.7$, *Astrophys. J.* **884**

(2019) 30.

[6] I. T. Andika, K. Jahnke, M. Onoue, E. Bañados, C. Mazzucchelli, M. Novak, A.-C. Eilers, B. P. Venemans, J.-T. Schindler, F. Walter, M. Neeleman, R. A. Simcoe, R. Decarli, E. P. Farina, V. Marian, A. Pensabene, T. M. Cooper and A. F. Rojas, *Probing the Nature of High Redshift Weak Emission Line Quasars: A Young Quasar with a Starburst Host Galaxy*, *Astrophys. J.* **903** (2020) 34 [2009.07784].

[7] E. Bañados, C. Mazzucchelli, E. Momjian, A.-C. Eilers, F. Wang, J.-T. Schindler, T. Connor, I. T. Andika, A. J. Barth, C. Carilli, F. B. Davies, R. Decarli, X. Fan, E. P. Farina, J. F. Hennawi, A. Pensabene, D. Stern, B. P. Venemans, L. Wenzl and J. Yang, *The Discovery of a Highly Accreting, Radio-loud Quasar at z = 6.82*, *Astrophys. J.* **909** (2021) 80 [2103.03295].

[8] F. Wang, J. Yang, X. Fan, J. F. Hennawi, A. J. Barth, E. Banados, F. Bian, K. Boutsia, T. Connor, F. B. Davies, R. Decarli, A.-C. Eilers, E. P. Farina, R. Green, L. Jiang, J.-T. Li, C. Mazzucchelli, R. Nanni, J.-T. Schindler, F. Venemans, Bram Walter, X.-B. Wu and M. Yue, *A luminous quasar at redshift 7.642*, *Astrophys. J. Lett.* **907** (2021) L1.

[9] M. Tegmark, J. Silk, M. J. Rees, A. Blanchard, T. Abel and F. Palla, *How small were the first cosmological objects?*, *Astrophys. J.* **474** (1997) 1 [astro-ph/9603007].

[10] M. C. Begelman and M. J. Rees, *The fate of dense stellar systems*, *Mon. Not. Roy. Astron. Soc.* **185** (1978) 847.

[11] M. J. Rees, *Black Hole Models for Active Galactic Nuclei*, *Ann. Rev. Astron. Astrophys.* **22** (1984) 471.

[12] Z. Haiman and A. Loeb, *What is the highest plausible redshift of luminous quasars?*, *Astrophys. J.* **552** (2001) 459 [astro-ph/0011529].

[13] M. Volonteri and M. J. Rees, *Quasars at z=6: The survival of the fittest*, *Astrophys. J.* **650** (2006) 669 [astro-ph/0607093].

[14] M. G. Haehnelt and M. J. Rees, *The formation of nuclei in newly formed galaxies and the evolution of the quasar population*, *Mon. Not. Roy. Astron. Soc.* **263** (1993) 168.

[15] I. Shlosman, J.-H. Choi, M. C. Begelman and K. Nagamine, *Supermassive Black Hole Seed Formation at High Redshifts: Long-Term Evolution of the Direct Collapse*, *Mon. Not. Roy. Astron. Soc.* **456** (2016) 500 [1508.05098].

[16] A. Loeb and F. A. Rasio, *Collapse of primordial gas clouds and the formation of quasar black holes*, *Astrophys. J.* **432** (1994) 52 [astro-ph/9401026].

[17] D. J. Eisenstein and A. Loeb, *Origin of quasar progenitors from the collapse of low spin cosmological perturbations*, *Astrophys. J.* **443** (1995) 11 [astro-ph/9401016].

[18] S. P. Oh and Z. Haiman, *Second-generation objects in the universe: radiative cooling and collapse of halos with virial temperatures above* 10^4 *kelvin*, *Astrophys. J.* **569** (2002) 558 [astro-ph/0108071].

[19] V. Bromm and A. Loeb, *Formation of the first supermassive black holes*, *Astrophys. J.* **596** (2003) 34 [astro-ph/0212400].

[20] S. M. Koushiappas, J. S. Bullock and A. Dekel, *Massive black hole seeds from low angular momentum material*, *Mon. Not. Roy. Astron. Soc.* **354** (2004) 292 [astro-ph/0311487].

[21] G. Lodato and P. Natarajan, *Supermassive black hole formation during the assembly of pre-galactic discs*, *Mon. Not. Roy. Astron. Soc.* **371** (2006) 1813 [astro-ph/0606159].

[22] S. L. Shapiro and S. A. Teukolsky, *The collapse of dense star clusters to supermassive black holes-The origin of quasars and AGNs*, *Astrophys. J.* **292** (1985) L41.

[23] G. D. Quinlan and S. L. Shapiro, *The collapse of dense star clusters to supermassive black holes-Binaries and gravitational radiation*, *Astrophys. J.* **321** (1987) 199.

[24] G. D. Quinlan and S. L. Shapiro, *Dynamical evolution of dense clusters of compact stars*, *Astrophys. J.* **343** (1989) 725.

[25] S. F. Portegies Zwart, H. Baumgardt, P. Hut, J. Makino and S. L. W. McMillan, *The Formation of massive black holes through collision runaway in dense young star clusters*, *Nature* **428** (2004) 724 [astro-ph/0402622].

[26] L. Mayer, S. Kazantzidis, A. Escala and S. Callegari, *Direct formation of supermassive black holes via multi-scale gas inflows in galaxy mergers*, *Nature* **466** (2010) 1082.

[27] F. Hoyle and W. A. Fowler, *Nature of strong radio sources*, *Nature* **197** (1963) 533.

[28] I. Iben, *Massive stars in quasi-static equlibrium*, *Astrophys. J.* **138** (1963) 1090.

[29] W. A. Fowler, *Massive Stars, Relativistic Polytropes, and Gravitational Radiation*, *Rev. Mod. Phys.* **36** (1964) 545.

[30] Ya. B. Zeldovich, *Gravitational instability: An Approximate theory for large density perturbations*, *Astron. Astrophys.* **5** (1970) 84.

[31] S. Chandrasekhar, *The Dynamical Instability of Gaseous Masses Approaching the*

Schwarzschild Limit in General Relativity, *Astrophys. J.* **140** (1964) 417.

[32] R. P. Feynman, *Feynman Lectures on Gravitation*. CRC Press, 2018.

[33] X.-D. Shi and G. M. Fuller, *Neutrinos and supermassive stars: Prospects for neutrino emission and detection*, *Astrophys. J.* **503** (1998) 307 [astro-ph/9801106].

[34] S. Kawamura, T. Nakamura, M. Ando, N. Seto, K. Tsubono, K. Numata, R. Takahashi, S. Nagano, T. Ishikawa, M. Musha, K.-i. Ueda, T. Sato, M. Hosokawa, K. Agatsuma, T. Akutsu, K.-s. Aoyanagi, K. Arai, A. Araya, H. Asada, T. Aso, Yoichi Chiba, T. Ebisuzaki, Y. Eriguchi, M.-K. Fujimoto, M. Fukushima, T. Futamase, K. Ganzu, T. Harada, T. Hashimoto, K. Hayama, W. Hikida, Y. Himemoto, H. Hirabayashi, T. Hiramatsu, K. Ichiki, T. Ikegami, K. T. Inoue, K. Ioka, K. Ishidoshiro, Y. Itoh, S. Kamagasako, N. Kanda, N. Kawashima, H. Kirihara, K. Kiuchi, S. Kobayashi, K. Kohri, Y. Kojima, K. Kokeyama, Y. Kozai, H. Kudoh, H. Kunimori, K. Kuroda, K.-i. Maeda, H. Matsuhara, Y. Mino, O. Miyakawa, S. Miyoki, H. Mizusawa, T. Morisawa, S. Mukohyama, I. Naito, N. Nakagawa, K. Nakamura, H. Nakano, K. Nakao, A. Nishizawa, Y. Niwa, C. Nozawa, M. Ohashi, N. Ohishi, M. Ohkawa, A. Okutomi, K. Oohara, N. Sago, M. Saijo, M. Sakagami, S. Sakata, M. Sasaki, S. Sato, M. Shibata, H. Shinkai, K. Somiya, H. Sotani, N. Sugiyama, H. Tagoshi, T. Takahashi, H. Takahashi, R. Takahashi, T. Takano, T. Tanaka, K. Taniguchi, A. Taruya, H. Tashiro, M. Tokunari, S. Tsujikawa, Y. Tsunesada, K. Yamamoto, T. Yamazaki, J. Yokoyama, C.-M. Yoo et al., *The Japanese space gravitational wave antenna: DECIGO*, *Class. Quant. Grav.* **28** (2011) 094011.

[35] G. M. Harry, P. Fritschel, D. A. Shaddock, W. Folkner and E. S. Phinney, *Laser interferometry for the big bang observer*, *Class. Quant. Grav.* **23** (2006) 4887.

[36] J. Crowder and N. J. Cornish, *Beyond LISA: Exploring future gravitational wave missions*, *Phys. Rev. D* **72** (2005) 083005 [gr-qc/0506015].

[37] G. Steigman, B. Dasgupta and J. F. Beacom, *Precise Relic WIMP Abundance and its Impact on Searches for Dark Matter Annihilation*, *Phys. Rev. D* **86** (2012) 023506 [1204.3622].

[38] K. Griest and M. Kamionkowski, *Unitarity Limits on the Mass and Radius of Dark Matter Particles*, *Phys. Rev. Lett.* **64** (1990) 615.

[39] B. W. Lee and S. Weinberg, *Cosmological Lower Bound on Heavy Neutrino Masses*, *Phys. Rev. Lett.* **39** (1977) 165.

[40] L. J. Hall, K. Jedamzik, J. March-Russell and S. M. West, *Freeze-In Production of FIMP Dark Matter*, *JHEP* **03** (2010) 080 [0911.1120].

[41] S. Dodelson and L. M. Widrow, *Sterile-neutrinos as dark matter*, *Phys. Rev. Lett.* **72** (1994) 17 [hep-ph/9303287].

[42] X.-D. Shi and G. M. Fuller, *A New dark matter candidate: Nonthermal sterile neutrinos*, *Phys. Rev. Lett.* **82** (1999) 2832 [astro-ph/9810076].

[43] K. N. Abazajian, G. M. Fuller and M. Patel, *Sterile neutrino hot, warm, and cold dark matter*, *Phys. Rev. D* **64** (2001) 023501 [astro-ph/0101524].

[44] C. T. Kishimoto and G. M. Fuller, *Lepton Number-Driven Sterile Neutrino Production in the Early Universe*, *Phys. Rev. D* **78** (2008) 023524 [0802.3377].

[45] K. N. Abazajian, *Resonantly Produced 7 keV Sterile Neutrino Dark Matter Models and the Properties of Milky Way Satellites*, *Phys. Rev. Lett.* **112** (2014) 161303 [1403.0954].

[46] L. Wolfenstein, *Neutrino Oscillations in Matter*, *Phys. Rev. D* **17** (1978) 2369.

[47] S. P. Mikheyev and A. Y. Smirnov, *Resonance enhancement of oscillations in matter and solar neutrino spectroscopy*, *Yadernaya Fizika* **42** (1985) 1441.

[48] H. An, M. Pospelov and J. Pradler, *New stellar constraints on dark photons*, *Phys. Lett. B* **725** (2013) 190 [1302.3884].

[49] J. H. Chang, R. Essig and S. D. McDermott, *Revisiting Supernova 1987A Constraints on Dark Photons*, *JHEP* **01** (2017) 107 [1611.03864].

[50] T. Emken, R. Essig, C. Kouvaris and M. Sholapurkar, *Direct Detection of Strongly Interacting Sub-GeV Dark Matter via Electron Recoils*, *J. Cosmol. Astropart. Phys.* **1909** (2019) 070 [1905.06348].

[51] T. Hambye, M. H. G. Tytgat, J. Vandecasteele and L. Vanderheyden, *Dark matter direct detection is testing freeze-in*, *Phys. Rev. D* **98** (2018) 075017 [1807.05022].

[52] J. D. Bowman, A. E. E. Rogers, R. A. Monsalve, T. J. Mozdzen and N. Mahesh, *An absorption profile centred at 78 megahertz in the sky-averaged spectrum*, *Nature (London)* **555** (2018) 67 [1810.05912].

[53] R. Barkana, *Possible interaction between baryons and dark-matter particles revealed by the first stars*, *Nature* **555** (2018) 71 [1803.06698].

[54] N. Seto, S. Kawamura and T. Nakamura, *Possibility of direct measurement of the acceleration of the universe using 0.1-Hz band laser interferometer gravitational wave antenna in space*, *Phys. Rev. Lett.* **87** (2001) 221103 [astro-ph/0108011].

[55] G. M. Fuller, S. E. Woosley and T. A. Weaver, *The evolution of radiation-dominated stars. I - Nonrotating supermassive stars*, *Astrophys. J.* **307** (1986) 675.

[56] D. J. Mortlock, S. J. Warren, B. P. Venemans, M. Patel, P. C. Hewett, R. G. McMahon, C. Simpson, T. Theuns, E. A. Gonzáles-Solares, A. Adamson, S. Dye, N. C. Hambly, P. Hirst, M. J. Irwin, E. Kuiper, A. Lawrence and H. J. A. Röttgering, *A luminous quasar at a redshift of z = 7.085*, *Nature* **474** (2011) 616 [1106.6088].

[57] B. P. Venemans, J. R. Findlay, W. J. Sutherland, G. De Rosa, R. G. McMahon, R. Simcoe, E. A. González-Solares, K. Kuijken and J. R. Lewis, *Discovery of three z>6.5 quasars in the VISTA Kilo-degree Infrared Galaxy (VIKING) survey*, *Astrophys. J.* **779** (2013) 24 [1311.3666].

[58] X.-B. Wu, F. Wang, X. Fan, W. Yi, W. Zuo, F. Bian, L. Jiang, I. D. McGreer, R. Wang, J. Yang, Q. Yang, D. Thompson and Y. Beletsky, *An ultraluminous quasar with a twelve-billion-solar-mass black hole at redshift 6.30*, *Nature* **518** (2015) 512 [1502.07418].

[59] E. Bañados, B. P. Venemans, C. Mazzucchelli, E. P. Farina, F. Walter, F. Wang, R. Decarli, D. Stern, X. Fan, F. B. Davies, J. F. Hennawi, R. A. Simcoe, M. L. Turner, H.-W. Rix, J. Yang, D. D. Kelson, G. C. Rudie and J. M. Winters, *An 800-million-solar-mass black hole in a significantly neutral Universe at a redshift of 7.5*, *Nature* (2017) .

[60] B. P. Venemans, F. Walter, R. Decarli, E. Bañados, C. Carilli, J. M. Winters, K. Schuster, E. da Cunha, X. Fan, E. P. Farina, C. Mazzucchelli, H.-W. Rix and A. Weiss, *Copious Amounts of Dust and Gas in a z=7.5 Quasar Host Galaxy*, *Astrophys. J.* **851** (2017) L8 [1712.01886].

[61] M. C. Begelman, M. Volonteri and M. J. Rees, *Formation of supermassive black holes by direct collapse in pregalactic halos*, *Mon. Not. Roy. Astron. Soc.* **370** (2006) 289 [astro-ph/0602363].

[62] M. C. Begelman, *Evolution of supermassive stars as a pathway to black hole formation*, *Mon. Not. Roy. Astrono. Soc.* **402** (2010) 673 [0910.4398].

[63] M. Shibata, Y. Sekiguchi, H. Uchida and H. Umeda, *Gravitational waves from supermassive stars collapsing to a supermassive black hole*, *Phys. Rev. D* **94** (2016) 021501 [1606.07147].

[64] A. Burrows and J. Hayes, *Pulsar recoil and gravitational radiation due to asymmetrical stellar collapse and explosion*, *Phys. Rev. Lett.* **76** (1996) 352 [astro-ph/9511106].

[65] E. Mueller and H.-T. Janka, *Gravitational radiation from convective instabilities in Type II supernova explosions*, *Astron. Astrophys.* **317,** (1997) 140.

[66] C. L. Fryer, D. E. Holz and S. A. Hughes, *Gravitational waves from stellar collapse: Correlations to explosion asymmetries*, *Astrophys. J.* **609** (2004) 288 [astro-ph/0403188].

[67] C. D. Ott, A. Burrows, L. Dessart and E. Livne, *A New Mechanism for Gravitational Wave Emission in Core-Collapse Supernovae*, *Phys. Rev. Lett.* **96** (2006) 201102 [astro-ph/0605493].

[68] L. Dessart, A. Burrows, C. Ott, E. Livne, S.-C. Yoon and N. Langer, *Multi-dimensional simulations of the accretion-induced collapse of white dwarfs to neutron stars*, *Astrophys. J.* **644** (2006) 1063 [astro-ph/0601603].

[69] K. Kotake, N. Ohnishi and S. Yamada, *Gravitational Radiation from Standing Accretion Shock Instability in Core-Collapse Supernovae*, *Astrophys. J.* **655** (2007) 406 [astro-ph/0607224].

[70] Y. B. Zeldovich and A. G. Polnarev, *Radiation of gravitational waves by a cluster of superdense stars*, *Soviet Astr* **18** (1974) 17.

[71] L. Smarr, *Gravitational Radiation from Distant Encounters and from Headon Collisions of Black Holes: The Zero Frequency Limit*, *Phys. Rev. D* **15** (1977) 2069.

[72] S. J. Kovacs and K. S. Thorne, *The Generation of Gravitational Waves. 4. Bremsstrahlung*, *Astrophys. J.* **224** (1978) 62.

[73] V. B. Braginskii and L. P. Grishchuk, *Kinematic resonance and memory effect in free-mass gravitational antennas Supernovae*, *Sov. Phys. JETP* **62** (1985) 427.

[74] M. S. Turner, *Gravitational radiation from point-masses in unbound orbits - Newtonian results*, *Astrophys. J.* **216** (1977) 610.

[75] R. Epstein, *The Generation of Gravitational Radiation by Escaping Supernova Neutrinos*, *Astrophys. J.* **223** (1978) 1037.

[76] M. S. Turner, *Gravitational Radiation from Supernova Neutrino Bursts*, *Nature* **274** (1978) 565.

[77] V. B. Braginskii and K. S. Thorne, *Gravitational-wave bursts with memory and experimental prospects Supernovae*, *Nature* **327** (1987) 23.

[78] M. Favata, *The gravitational-wave memory effect*, *Class. Quant. Grav.* **27** (2010) 084036 [1003.3486].

[79] N. Sago, K. Ioka, T. Nakamura and R. Yamazaki, *Gravitational wave memory of*

gamma-ray burst jets, *Phys. Rev. D* **70** (2004) 104012 [gr-qc/0405067].

[80] S. W. Hawking and W. Israel, eds., *Three Hundred Years of Gravitation*. Cambridge University Press, 1989.

[81] P. J. Schinder, D. N. Schramm, P. J. Wiita, S. H. Margolis and D. L. Tubbs, *Neutrino Emission by the Pair, Plasma and Photoprocesses in the Weinberg-Salam Model*, *Astrophys. J.* **313** (1987) 531.

[82] N. Itoh, T. Adachi, M. Nakagawa, Y. Kohyama and H. Munakata, *Neutrino energy loss in stellar interiors. III - Pair, photo-, plasma, and bremsstrahlung processes*, *Astrophys. J.* **339** (1989) 354.

[83] N. Itoh, H. Hayashi, A. Nishikawa and Y. Kohyama, *Neutrino Energy Loss in Stellar Interiors. VII. Pair, Photo-, Plasma, Bremsstrahlung, and Recombination Neutrino Processes*, *Astrophys. J. S.* **102** (1996) 411.

[84] F. Linke, J. A. Font, H.-T. Janka, E. Muller and P. Papadopoulos, *Spherical collapse of supermassive stars: Neutrino emission and gamma-ray bursts*, *Astron. Astrophys.* **376** (2001) 568 [astro-ph/0103144].

[85] K.-J. Chen, A. Heger, S. Woosley, A. Almgren, D. Whalen and J. Johnson, *The General Relativistic Instability Supernova of a Supermassive Population III Star*, *Astrophys. J.* **790** (2014) 162 [1402.4777].

[86] R. K. Sachs and A. M. Wolfe, *Perturbations of a cosmological model and angular variations of the microwave background*, *Astrophys. J.* **147** (1967) 73.

[87] C. Y. Cardall and G. M. Fuller, *General relativistic effects in the neutrino driven wind and r process nucleosynthesis*, *Astrophys. J.* **486** (1997) L111 [astro-ph/9701178].

[88] T. A. Apostolatos, C. Cutler, G. J. Sussman and K. S. Thorne, *Spin induced orbital precession and its modulation of the gravitational wave forms from merging binaries*, *Phys. Rev. D* **49** (1994) 6274.

[89] L. Barack and C. Cutler, *LISA capture sources: Approximate waveforms, signal-to-noise ratios, and parameter estimation accuracy*, *Phys. Rev. D* **69** (2004) 082005 [gr-qc/0310125].

[90] K. Yagi and N. Seto, *Detector configuration of DECIGO/BBO and identification of cosmological neutron-star binaries*, *Phys. Rev. D* **83** (2011) 044011 [1101.3940].

[91] P. N. Payne, *SMARR'S ZERO FREQUENCY LIMIT CALCULATION*, *Phys. Rev. D* **28** (1983) 1894.

[92] R. S. Foster and D. C. Backer, *Constructing a pulsar timing array*, *Astrophys. J.* **361** (1990) 300.

[93] D. R. Lorimer, *Binary and millisecond pulsars*, *Living reviews in relativity* **11** (2008) 8.

[94] F. A. Jenet, J. W. Armstrong and M. Tinto, *Pulsar Timing Sensitivity to Very-Low-Frequency Gravitational Waves*, *Phys. Rev. D* **83** (2011) 081301 [1101.3759].

[95] P. Amaro-Seoane, H. Audley, S. Babak, J. Baker, E. Barausse, P. Bender, E. Berti, P. Binetruy, M. Born, D. Bortoluzzi, J. Camp, C. Caprini, V. Cardoso, M. Colpi, J. Conklin, N. Cornish, C. Cutler, K. Danzmann, R. Dolesi, V. Ferraioli, Luigi Ferroni, E. Fitzsimons, J. Gair, L. Gesa Bote, D. Giardini, F. Gibert, C. Grimani, H. Halloin, G. Heinzel, T. Hertog, M. Hewitson, K. Holley-Bockelmann, D. Hollington, M. Hueller, H. Inchauspe, P. Jetzer, N. Karnesis, C. Killow, A. Klein, B. Klipstein, N. Korsakova, S. L. Larson, J. Livas, I. Lloro, N. Man, D. Mance, J. Martino, I. Mateos, K. McKenzie, S. T. McWilliams, C. Miller, G. Mueller, G. Nardini, G. Nelemans, M. Nofrarias, A. Petiteau, P. Pivato, E. Plagnol, E. Porter, J. Reiche, D. Robertson, N. Robertson, E. Rossi, G. Russano, B. Schutz, A. Sesana, D. Shoemaker, J. Slutsky, C. F. Sopuerta, T. Sumner, N. Tamanini, I. Thorpe, M. Troebs, M. Vallisneri, A. Vecchio, D. Vetrugno, S. Vitale, M. Volonteri, G. Wanner, H. Ward, P. Wass, W. Weber, J. Ziemer and P. Zweifel, *Laser Interferometer Space Antenna*, 1702.00786.

[96] P. J. Montero, H.-T. Janka and E. Muller, *Relativistic collapse and explosion of rotating supermassive stars with thermonuclear effects*, *Astrophys. J.* **749** (2012) 37 [1108.3090].

[97] G. M. Fuller and X.-D. Shi, *Supermassive stars as gamma-ray bursters*, *Astrophys. J.* **502** (1998) L5 [astro-ph/9711020].

[98] X.-D. Shi, G. M. Fuller and F. Halzen, *Observing the birth of supermassive black holes with the 'ICECUBE' neutrino detector*, *Phys. Rev. Lett.* **81** (1998) 5722 [astro-ph/9805242].

[99] E. Grohs and G. M. Fuller, *The surprising influence of late charged current weak interactions on Big Bang Nucleosynthesis*, *Nucl. Phys. B* **911** (2016) 955 [1607.02797].

[100] CMB-S4 collaboration, K. N. Abazajian, P. Adshead, Z. Ahmed, S. W. Allen, D. Alonso, K. S. Arnold, C. Baccigalupi, J. G. Bartlett, N. Battaglia, B. A. Benson, C. A. Bischoff, J. Borrill, V. Buza, E. Calabrese, R. Caldwell, J. E. Carlstrom, C. L. Chang, T. M. Crawford, F.-Y. Cyr-Racine, T. De Bernardis, Francesco de Haan, S. di Serego Alighieri, J. Dunkley, C. Dvorkin, J. Errard, G. Fabbian, S. Feeney, S. Ferraro, J. P. Filippini, R. Flauger, G. M. Fuller, V. Gluscevic, D. Green, D. Grin, E. Grohs, J. W. Henning, J. C. Hill, R. Hlozek, G. Holder, W. Holzapfel, W. Hu, K. M. Huffenberger, R. Keskitalo, L. Knox, A. Kosowsky, J. Kovac, E. D. Kovetz, C.-L. Kuo, A. Kusaka, M. Le Jeune, A. T. Lee, M. Lilley, M. Loverde, M. S. Madhavacheril, A. Mantz, D. J. E. Marsh, J. McMahon,

P. D. Meerburg, J. Meyers, A. D. Miller, J. B. Munoz, H. N. Nguyen, M. D. Niemack, M. Peloso, J. Peloton, L. Pogosian, C. Pryke, M. Raveri, C. L. Reichardt, G. Rocha, A. Rotti, E. Schaan, M. M. Schmittfull, D. Scott, N. Sehgal, S. Shandera, B. D. Sherwin, T. L. Smith, L. Sorbo, G. D. Starkman, K. T. Story, A. van Engelen, J. D. Vieira, S. Watson, N. Whitehorn and W. L. Kimmy Wu, *CMB-S4 Science Book, First Edition*, 1610.02743.

[101] R. Maiolino, M. Haehnelt, M. T. Murphy, D. Queloz, L. Origlia, J. Alcala, Y. Alibert, P. J. Amado, C. Allende Prieto, M. Ammler-von Eiff, M. Asplund, M. Barstow, G. Becker, X. Bonfils, F. Bouchy, A. Bragaglia, M. R. Burleigh, A. Chiavassa, D. A. Cimatti, S. Cirasuolo, M. Cristiani, V. D'Odorico, D. Dravins, E. Emsellem, J. Farihi, P. Figueira, J. Fynbo, B. T. Gansicke, M. Gillon, B. Gustafsson, V. Hill, G. Israelyan, A. Korn, S. Larsen, P. De Laverny, J. Liske, C. Lovis, A. Marconi, C. Martins, P. Molaro, B. Nisini, E. Oliva, P. Petitjean, M. Pettini, A. Recio Blanco, R. Rebolo, A. Reiners, C. Rodriguez-Lopez, N. Ryde, N. C. Santos, S. Savaglio, I. Snellen, K. Strassmeier, N. Tanvir, L. Testi, E. Tolstoy, A. Triaud, L. Vanzi, M. Viel and M. Volonteri, *A Community Science Case for E-ELT HIRES*, 1310.3163.

[102] R. J. Cooke, M. Pettini, K. M. Nollett and R. A. Jorgenson, *The primordial deuterium abundance of the most metal-poor damped Lyα system*, *Astrophys. J.* **830** (2016) 148 [1607.03900].

[103] P. Galison and A. Manohar, *Two Z's or not two Z's?*, *Phys. Lett. B* **136** (1984) 279.

[104] B. Holdom, *Two U(1)'s and Epsilon Charge Shifts*, *Phys. Lett. B* **166** (1986) 196.

[105] C. Boehm and P. Fayet, *Scalar dark matter candidates*, *Nucl. Phys. B* **683** (2004) 219 [hep-ph/0305261].

[106] N. Arkani-Hamed, D. P. Finkbeiner, T. R. Slatyer and N. Weiner, *A Theory of Dark Matter*, *Phys. Rev. D* **79** (2009) 015014 [0810.0713].

[107] M. Pospelov, *Secluded U(1) below the weak scale*, *Phys. Rev. D* **80** (2009) 095002 [0811.1030].

[108] J. Redondo, *Helioscope Bounds on Hidden Sector Photons*, *JCAP* **0807** (2008) 008 [0801.1527].

[109] J. Redondo and M. Postma, *Massive hidden photons as lukewarm dark matter*, *JCAP* **0902** (2009) 005 [0811.0326].

[110] J. Jaeckel, J. Redondo and A. Ringwald, *Signatures of a hidden cosmic microwave background*, *Phys. Rev. Lett.* **101** (2008) 131801 [0804.4157].

[111] A. Mirizzi, J. Redondo and G. Sigl, *Microwave Background Constraints on Mixing of Photons with Hidden Photons*, *JCAP* **03** (2009) 026 [0901.0014].

[112] J. Redondo and G. Raffelt, *Solar constraints on hidden photons re-visited*, *JCAP* **1308** (2013) 034 [1305.2920].

[113] K. E. Kunze and M. A. Vazquez-Mozo, *Constraints on hidden photons from current and future observations of CMB spectral distortions*, *JCAP* **12** (2015) 028 [1507.02614].

[114] E. Hardy and R. Lasenby, *Stellar cooling bounds on new light particles: plasma mixing effects*, *JHEP* **02** (2017) 033 [1611.05852].

[115] M. Pospelov, J. Pradler, J. T. Ruderman and A. Urbano, *Room for New Physics in the Rayleigh-Jeans Tail of the Cosmic Microwave Background*, *Phys. Rev. Lett.* **121** (2018) 031103 [1803.07048].

[116] E. Rrapaj, A. Sieverding and Y.-Z. Qian, *Rate of dark photon emission from electron positron annihilation in massive stars*, *Phys. Rev. D* **100** (2019) 023009 [1904.10567].

[117] S. D. McDermott and S. J. Witte, *Cosmological evolution of light dark photon dark matter*, *Phys. Rev. D* **101** (2020) 063030 [1911.05086].

[118] S. J. Witte, S. Rosauro-Alcaraz, S. D. McDermott and V. Poulin, *Dark photon dark matter in the presence of inhomogeneous structure*, *JHEP* **06** (2020) 132 [2003.13698].

[119] A. Caputo, H. Liu, S. Mishra-Sharma and J. T. Ruderman, *Dark Photon Oscillations in Our Inhomogeneous Universe*, *Phys. Rev. Lett.* **125** (2020) 221303 [2002.05165].

[120] A. Caputo, H. Liu, S. Mishra-Sharma and J. T. Ruderman, *Modeling Dark Photon Oscillations in Our Inhomogeneous Universe*, *Phys. Rev. D* **102** (2020) 103533 [2004.06733].

[121] A. Caputo, H. Liu, S. Mishra-Sharma, M. Pospelov, J. T. Ruderman and A. Urbano, *Edges and Endpoints in 21-cm Observations from Resonant Photon Production*, *arXiv:2009.03899* (2020) .

[122] A. Fradette, M. Pospelov, J. Pradler and A. Ritz, *Cosmological Constraints on Very Dark Photons*, *Phys. Rev. D* **90** (2014) 035022 [1407.0993].

[123] J. Berger, K. Jedamzik and D. G. E. Walker, *Cosmological Constraints on Decoupled Dark Photons and Dark Higgs*, *JCAP* **11** (2016) 032 [1605.07195].

[124] M. Pettini and R. Cooke, *A new, precise measurement of the primordial abundance of deuterium*, *Mon. Not. R. Astron Soc.* **425** (2012) 2477 [1205.3785].

[125] R. J. Cooke, M. Pettini, R. A. Jorgenson, M. T. Murphy and C. C. Steidel, *Precision measures of the primordial abundance of deuterium*, *Astrophys. J.* **781** (2014) 31 [1308.3240].

[126] M. Kawasaki, K. Kohri, T. Moroi, K. Murai and H. Murayama, *Big-bang nucleosynthesis with sub-GeV massive decaying particles*, *JCAP* **12** (2020) 048 [2006.14803].

[127] L. Forestell, D. E. Morrissey and G. White, *Limits from BBN on Light Electromagnetic Decays*, *JHEP* **01** (2019) 074 [1809.01179].

[128] J. Coffey, L. Forestell, D. E. Morrissey and G. White, *Cosmological Bounds on sub-GeV Dark Vector Bosons from Electromagnetic Energy Injection*, *JHEP* **07** (2020) 179 [2003.02273].

[129] M. Hufnagel, K. Schmidt-Hoberg and S. Wild, *BBN constraints on MeV-scale dark sectors. Part II. Electromagnetic decays*, *JCAP* **11** (2018) 032 [1808.09324].

[130] G. M. Fuller, C. T. Kishimoto and A. Kusenko, *Heavy sterile neutrinos, entropy and relativistic energy production, and the relic neutrino background*, 1110.6479.

[131] E. Grohs, G. M. Fuller, C. T. Kishimoto, M. W. Paris and A. Vlasenko, *Neutrino energy transport in weak decoupling and big bang nucleosynthesis*, *Phys. Rev. D* **93** (2016) 083522 [1512.02205].

[132] E. W. Kolb and M. S. Turner, *The Early Universe*. Westview Press, Boulder, Colorado, 1990.

[133] E. Braaten and D. Segel, *Neutrino energy loss from the plasma process at all temperatures and densities*, *Phys. Rev. D* **48** (1993) 1478 [hep-ph/9302213].

[134] G. G. Raffelt, *Stars as laboratories for fundamental physics*. University of Chicago Press, 1996.

[135] H. A. Weldon, *Simple Rules for Discontinuities in Finite Temperature Field Theory*, *Phys. Rev. D* **28** (1983) 2007.

[136] PLANCK collaboration, N. Aghanim, Y. Akrami, M. Ashdown, J. Aumont, C. Baccigalupi, M. Ballardini, A. J. Banday, R. B. Barreiro, N. Bartolo, S. Basak, R. Battye, K. Benabed, J. P. Bernard, M. Bersanelli, P. Bielewicz, J. J. Bock, J. R. Bond, J. Borrill, F. Bouchet, F. R. Boulanger, M. Bucher, C. Burigana, R. C. Butler, E. Calabrese, J. F. Cardoso, J. Carron, A. Challinor, H. C. Chiang, J. Chluba, L. P. L. Colombo, C. Combet, D. Contreras, B. P. Crill, F. Cuttaia, P. de Bernardis, G. de Zotti, J. Delabrouille, J. M. Delouis, E. Di Valentino, J. M. Diego, O. Doré, M. Douspis, A. Ducout, X. Dupac, S. Dusini, G. Efstathiou, F. Elsner, T. A. Enßlin, H. K. Eriksen, Y. Fantaye, M. Farhang,

J. Fergusson, R. Fernandez-Cobos, F. Finelli, F. Forastieri, M. Frailis, A. A. Fraisse, E. Franceschi, A. Frolov, S. Galeotta, S. Galli, K. Ganga, R. T. Génova-Santos, M. Gerbino, T. Ghosh, J. González-Nuevo, K. M. Górski, S. Gratton, A. Gruppuso, J. E. Gudmundsson, J. Hamann, W. Handley, F. K. Hansen, D. Herranz, S. R. Hildebrandt, E. Hivon, Z. Huang, A. H. Jaffe, W. C. Jones, A. Karakci, E. Keihänen, R. Keskitalo, K. Kiiveri, J. Kim, T. S. Kisner, L. Knox, N. Krachmalnicoff, M. Kunz, H. Kurki-Suonio, G. Lagache, J. M. Lamarre, A. Lasenby, M. Lattanzi, C. R. Lawrence, M. Le Jeune, P. Lemos, J. Lesgourgues, F. Levrier, A. Lewis, M. Liguori, P. B. Lilje et al., *Planck 2018 results. VI. Cosmological parameters*, *Astron. Astrophys.* **641** (2018) 67 [1807.06209].

[137] L. Kawano, *Let's go: Early universe 2. Primordial nucleosynthesis the computer way*, *NASA STI/Recon Technical Report* **92** (1992) 25163.

[138] E. Grohs and G. M. Fuller, *Insights into neutrino decoupling gleaned from considerations of the role of electron mass*, *Nucl. Phys. B* **923** (2017) 222 [1706.03391].

[139] A. F. Heckler, *Astrophysical applications of quantum corrections to the equation of state of a plasma*, *Phys. Rev. D* **49** (1994) 611.

[140] N. Fornengo, C. W. Kim and J. Song, *Finite temperature effects on the neutrino decoupling in the early Universe*, *Phys. Rev. D* **56** (1997) 5123 [hep-ph/9702324].

[141] J. J. Bennett, G. Buldgen, M. Drewes and Y. Y. Y. Wong, *Towards a precision calculation of the effective number of neutrinos N_{eff} in the Standard Model: the QED equation of state*, *JCAP* **2020** (2020) 003 [1911.04504].

[142] A. D. Dolgov, S. H. Hansen and D. V. Semikoz, *Non-equilibrium corrections to the spectra of massless neutrinos in the early universe*, *Nucl. Phys. B* **503** (1997) 426 [hep-ph/9703315].

[143] G. Mangano, G. Miele, S. Pastor, T. Pinto, O. Pisanti and P. D. Serpico, *Relic neutrino decoupling including flavour oscillations*, *Nucl. Phys. B* **729** (2005) 221 [hep-ph/0506164].

[144] J. Birrell, C.-T. Yang, P. Chen and J. Rafelski, *Relic neutrinos: Physically consistent treatment of effective number of neutrinos and neutrino mass*, *Phys. Rev. D* **89** (2014) 023008.

[145] P. F. de Salas and S. Pastor, *Relic neutrino decoupling with flavour oscillations revisited*, *JCAP* **7** (2016) 051 [1606.06986].

[146] M. Escudero Abenza, *Precision early universe thermodynamics made simple: N_{eff} and neutrino decoupling in the Standard Model and beyond*, *JCAP* **2020** (2020) 048 [2001.04466].

[147] J. Froustey, C. Pitrou and M. C. Volpe, *Neutrino decoupling including flavour oscillations and primordial nucleosynthesis*, *JCAP* **12** (2020) 015 [2008.01074].

[148] K. Akita and M. Yamaguchi, *A precision calculation of relic neutrino decoupling*, *JCAP* **08** (2020) 012 [2005.07047].

[149] M. Ibe, S. Kobayashi, Y. Nakayama and S. Shirai, *Cosmological constraint on dark photon from $N_{\rm eff}$*, *JHEP* **04** (2020) 009 [1912.12152].

[150] A. Coc, P. Petitjean, J.-P. Uzan, E. Vangioni, P. Descouvemont, C. Iliadis and R. Longland, *New reaction rates for improved primordial D /H calculation and the cosmic evolution of deuterium*, *Phys. Rev. D* **92** (2015) 123526 [1511.03843].

[151] L. E. Marcucci, G. Mangano, A. Kievsky and M. Viviani, *Implication of the Proton-Deuteron Radiative Capture for Big Bang Nucleosynthesis*, *Phys. Rev. Lett.* **116** (2016) 102501 [1510.07877].

[152] S. R. Beane, E. Chang, W. Detmold, K. Orginos, A. Parreño, M. J. Savage, B. C. Tiburzi and Nplqcd Collaboration, *Ab initio Calculation of the n p $\rightarrow$d γ Radiative Capture Process*, *Phys. Rev. Lett.* **115** (2015) 132001 [1505.02422].

[153] C. Broggini, D. Bemmerer, A. Caciolli and D. Trezzi, *LUNA: Status and prospects*, *Prog. Part. Nucl. Phys.* **98** (2018) 55 [1707.07952].

[154] M. W. Paris, G. M. Hale, A. C. Hayes-Sterbenz and G. Jungman, *R-matrix analysis of reactions in the 9B compound system*, *Nucl. Data Sheets* **120** (2014) 184 [1304.3153].

[155] C. Iliadis, K. S. Anderson, A. Coc, F. X. Timmes and S. Starrfield, *Bayesian Estimation of Thermonuclear Reaction Rates*, *Astrophys. J.* **831** (2016) 107 [1608.05853].

[156] Á. Gómez Iñesta, C. Iliadis and A. Coc, *Bayesian Estimation of Thermonuclear Reaction Rates for Deuterium+Deuterium Reactions*, *Astrophys. J.* **849** (2017) 134 [1710.01647].

[157] R. S. de Souza, S. R. Boston, A. Coc and C. Iliadis, *Thermonuclear fusion rates for tritium + deuterium using Bayesian methods*, *Phys. Rev. C* **99** (2019) 014619 [1901.04857].

[158] A. Sung, H. Tu and M.-R. Wu, *New constraint from supernova explosions on light particles beyond the Standard Model*, *Phys. Rev. D* **99** (2019) 121305 [1903.07923].

[159] W. DeRocco, P. W. Graham, D. Kasen, G. Marques-Tavares and S. Rajendran, *Observable signatures of dark photons from supernovae*, *JHEP* **02** (2019) 171 [1901.08596].

[160] R. J. Cooke, M. Pettini and C. C. Steidel, *One Percent Determination of the Primordial*

Deuterium Abundance, *Astrophys. J.* **855** (2018) 102 [1710.11129].

[161] E. B. Grohs, J. R. Bond, R. J. Cooke, G. M. Fuller, J. Meyers and M. W. Paris, *Big Bang Nucleosynthesis and Neutrino Cosmology*, 1903.09187.

[162] T. Lin, *Dark matter models and direct detection*, *PoS* **333** (2019) 009 [1904.07915].

[163] A. De Rujula, S. L. Glashow and U. Sarid, *CHARGED DARK MATTER*, *Nucl. Phys.* **B333** (1990) 173.

[164] S. Dimopoulos, D. Eichler, R. Esmailzadeh and G. D. Starkman, *Getting a Charge Out of Dark Matter*, *Phys. Rev. D* **41** (1990) 2388.

[165] S. L. Dubovsky, D. S. Gorbunov and G. I. Rubtsov, *Narrowing the window for millicharged particles by CMB anisotropy*, *JETP Lett.* **79** (2004) 1 [hep-ph/0311189].

[166] S. D. McDermott, H.-B. Yu and K. M. Zurek, *Turning off the Lights: How Dark is Dark Matter?*, *Phys. Rev. D* **83** (2011) 063509 [1011.2907].

[167] C. Dvorkin, K. Blum and M. Kamionkowski, *Constraining Dark Matter-Baryon Scattering with Linear Cosmology*, *Phys. Rev. D* **89** (2014) 023519 [1311.2937].

[168] E. D. Kovetz, V. Poulin, V. Gluscevic, K. K. Boddy, R. Barkana and M. Kamionkowski, *Tighter limits on dark matter explanations of the anomalous EDGES 21 cm signal*, *Phys. Rev. D* **98** (2018) 103529 [1807.11482].

[169] W. L. Xu, C. Dvorkin and A. Chael, *Probing sub-GeV Dark Matter-Baryon Scattering with Cosmological Observables*, *Phys. Rev. D* **97** (2018) 103530 [1802.06788].

[170] T. R. Slatyer and C.-L. Wu, *Early-Universe constraints on dark matter-baryon scattering and their implications for a global 21 cm signal*, *Phys. Rev. D* **98** (2018) 023013 [1803.09734].

[171] X. Chu, T. Hambye and M. H. G. Tytgat, *The Four Basic Ways of Creating Dark Matter Through a Portal*, *J. Cosmol. Astropart. Phys.* **1205** (2012) 034 [1112.0493].

[172] C. Dvorkin, T. Lin and K. Schutz, *Making dark matter out of light: freeze-in from plasma effects*, *Phys. Rev. D* **99** (2019) 115009 [1902.08623].

[173] S. Davidson, B. Campbell and D. C. Bailey, *Limits on particles of small electric charge*, *Phys. Rev. D* **43** (1991) 2314.

[174] R. Essig, J. Mardon and T. Volansky, *Direct Detection of Sub-GeV Dark Matter*, *Phys. Rev. D* **85** (2012) 076007 [1108.5383].

[175] M. Battaglieri, A. Belloni, A. Chou, P. Cushman, B. Echenard, R. Essig, J. Estrada, J. L. Feng, B. Flaugher, P. J. Fox, P. Graham, C. Hall, R. Harnik, J. Hewett, J. Incandela, E. Izaguirre, D. McKinsey, M. Pyle, N. Roe, P. Rybka, Gray Sikivie, T. M. P. Tait, N. Toro, R. Van De Water, N. Weiner, K. Zurek, E. Adelberger, A. Afanasev, D. Alexander, J. Alexander, V. Cristian Antochi, D. M. Asner, H. Baer, D. Banerjee, E. Baracchini, P. Barbeau, J. Barrow, N. Bastidon, J. Battat, S. Benson, A. Berlin, M. Bird, N. Blinov, K. K. Boddy, M. Bondi, W. M. Bonivento, M. Boulay, J. Boyce, M. Brodeur, L. Broussard, R. Budnik, P. Bunting, M. Caffee, S. S. Caiazza, S. Campbell, T. Cao, G. Carosi, M. Carpinelli, G. Cavoto, A. Celentano, J. Hyeok Chang, S. Chattopadhyay, A. Chavarria, C.-Y. Chen, K. Clark, J. Clarke, O. Colegrove, J. Coleman, D. Cooke, R. Cooper, M. Crisler, P. Crivelli, F. D'Eramo, D. D'Urso, E. Dahl, W. Dawson, M. De Napoli, R. De Vita, P. DeNiverville, S. Derenzo, A. Di Crescenzo, E. Di Marco, K. R. Dienes, M. Diwan, D. Handiipondola Dongwi, A. Drlica-Wagner, S. Ellis, A. Chigbo Ezeribe, G. Farrar, F. Ferrer, E. Figueroa-Feliciano, A. Filippi, G. Fiorillo, B. Fornal, A. Freyberger, C. Frugiuele, C. Galbiati, I. Galon, S. Gardner, A. Geraci, G. Gerbier et al., *US Cosmic Visions: New Ideas in Dark Matter 2017: Community Report*, in *U.S. Cosmic Visions: New Ideas in Dark Matter College Park, MD, USA, March 23-25, 2017*, 2017, 1707.04591.

[176] R. Barkana, N. J. Outmezguine, D. Redigolo and T. Volansky, *Strong constraints on light dark matter interpretation of the EDGES signal*, *Phys. Rev. D* **98** (2018) 103005 [1803.03091].

[177] A. Berlin, D. Hooper, G. Krnjaic and S. D. McDermott, *Severely Constraining Dark Matter Interpretations of the 21-cm Anomaly*, *Phys. Rev. Lett.* **121** (2018) 011102 [1803.02804].

[178] J. B. Muñoz and A. Loeb, *A small amount of mini-charged dark matter could cool the baryons in the early Universe*, *Nature (London)* **557** (2018) 684 [1802.10094].

[179] H. Liu, N. J. Outmezguine, D. Redigolo and T. Volansky, *Reviving Millicharged Dark Matter for 21-cm Cosmology*, *Phys. Rev. D* **100** (2019) 123011 [1908.06986].

[180] L. Chuzhoy and E. W. Kolb, *Reopening the window on charged dark matter*, *J. Cosmol. Astropart. Phys.* **0907** (2009) 014 [0809.0436].

[181] A. R. Bell, *The acceleration of cosmic rays in shock fronts - I*, *Mon. Not. R. Astron Soc.* **182** (1978) 147.

[182] R. D. Blandford and J. P. Ostriker, *Particle acceleration by astrophysical shocks*, *Astrophys. J.* **221** (1978) L29.

[183] P.-K. Hu, A. Kusenko and V. Takhistov, *Dark Cosmic Rays*, *Phys. Lett.* **B768** (2017) 18 [1611.04599].

[184] D. Dunsky, L. J. Hall and K. Harigaya, *CHAMP Cosmic Rays*, *J. Cosmol. Astropart. Phys.* **1907** (2019) 015 [1812.11116].

[185] M. Heikinheimo, M. Raidal, C. Spethmann and H. Veermäe, *Dark matter self-interactions via collisionless shocks in cluster mergers*, *Phys. Lett.* **B749** (2015) 236 [1504.04371].

[186] C. Spethmann, H. Veermäe, T. Sepp, M. Heikinheimo, B. Deshev, A. Hektor and M. Raidal, *Simulations of Galaxy Cluster Collisions with a Dark Plasma Component*, *Astron. Astrophys.* **608** (2017) A125 [1603.07324].

[187] A. Stebbins and G. Krnjaic, *New Limits on Charged Dark Matter from Large-Scale Coherent Magnetic Fields*, *J. Cosmol. Astropart. Phys.* **1912** (2019) 003 [1908.05275].

[188] A. A. Prinz, R. Baggs, J. Ballam, S. Ecklund, C. Fertig, J. A. Jaros, K. Kase, A. Kulikov, W. G. Langeveld, R. Leonard, T. Marvin, T. Nakashima, W. R. Nelson, A. Odian, M. Pertsova, G. Putallaz and A. Weinstein, *Search for millicharged particles at SLAC*, *Phys. Rev. Lett.* **81** (1998) 1175 [hep-ex/9804008].

[189] A. Haas, C. S. Hill, E. Izaguirre and I. Yavin, *Looking for milli-charged particles with a new experiment at the LHC*, *Phys. Lett.* **B746** (2015) 117 [1410.6816].

[190] G. Magill, R. Plestid, M. Pospelov and Y.-D. Tsai, *Millicharged particles in neutrino experiments*, *Phys. Rev. Lett.* **122** (2019) 071801 [1806.03310].

[191] J. Jaeckel, M. Jankowiak and M. Spannowsky, *LHC probes the hidden sector*, *Phys. Dark Univ.* **2** (2013) 111 [1212.3620].

[192] S. Davidson, S. Hannestad and G. Raffelt, *Updated bounds on millicharged particles*, *J. High Energy Phys.* **05** (2000) 003 [hep-ph/0001179].

[193] H. Vogel and J. Redondo, *Dark Radiation constraints on minicharged particles in models with a hidden photon*, *J. Cosmol. Astropart. Phys.* **1402** (2014) 029 [1311.2600].

[194] J. H. Chang, R. Essig and S. D. McDermott, *Supernova 1987A Constraints on Sub-GeV Dark Sectors, Millicharged Particles, the QCD Axion, and an Axion-like Particle*, *J. High Energy Phys.* **09** (2018) 051 [1803.00993].

[195] C. Boehm, M. J. Dolan and C. McCabe, *A Lower Bound on the Mass of Cold Thermal Dark Matter from Planck*, *J. Cosmol. Astropart. Phys.* **1308** (2013) 041 [1303.6270].

[196] R. Foot and S. Vagnozzi, *Dissipative hidden sector dark matter*, *Phys. Rev. D* **91** (2015) 023512 [1409.7174].

[197] M. S. Mahdawi and G. R. Farrar, *Constraints on Dark Matter with a moderately large*

and velocity-dependent DM-nucleon cross-section, *J. Cosmol. Astropart. Phys.* **1810** (2018) 007 [1804.03073].

[198] B. T. Draine, *Physics of the Interstellar and Intergalactic Medium*. Princeton University Press, Princeton, NJ, 2011.

[199] B. T. Draine and C. F. McKee, *Theory of Interstellar Shocks*, *Annu. Rev. Astron. Astrophys* **31** (1993) 373.

[200] D. Burgess and M. Scholer, *Collisionless Shocks in Space Plasmas: Structure and Accelerated Particles*. Cambridge University Press, Cambridge, England, 2015.

[201] A. Marcowith, A. Bret, A. Bykov, M. E. Dieckman, L. O. C. Drury, B. Lembège, M. Lemoine, G. Morlino, G. Murphy, G. Pelletier, I. Plotnikov, B. Reville, M. Riquelme, L. Sironi and A. Stockem Novo, *The microphysics of collisionless shock waves*, *Rept. Prog. Phys.* **79** (2016) 046901 [1604.00318].

[202] F. H. Shu, *The Physics of Astrophysics: Gas Dynamics*, vol. 2. University Science Books, Sausalito, 1991.

[203] J. Skilling, *Cosmic Ray Streaming. I - Effect of Alfvén waves on particles*, *Mon. Not. R. Astron. Soc.* **172** (1975) 557.

[204] M. A. Malkov and H. J. Völk, *Diffusive ion acceleration at shocks: The problem of injection*, *Adv. Space Res.* **21** (1998) 551.

[205] D. Caprioli, A. R. Pop and A. Spitkovsky, *Simulations and Theory of Ion Injection at Non-relativistic Collisionless Shocks*, *Astrophys. J.* **798** (2015) L28 [1409.8291].

[206] M. A. Malkov and H. J. Völk, *Theory of ion injection shocks*, *Astron. Astrophys.* **300** (1995) 605.

[207] M. A. Malkov, *Ion leakage from quasiparallel collisionless shocks: implications for injection and shock dissipation*, *Phys. Rev. E* **58** (1998) 4911 [astro-ph/9806340].

[208] A. M. Bykov, A. Brandenburg, M. A. Malkov and S. M. Osipov, *Microphysics of cosmic ray driven plasma instabilities*, *Space Sci. Rev.* **178** (2013) 201 [1304.7081].

[209] E. M. Reynoso, J. P. Hughes and D. A. Moffett, *On the Radio Polarization Signature of Efficient and Inefficient Particle Acceleration in Supernova Remnant SN 1006*, *Astron. J.* **145** (2013) 104 [1302.4678].

[210] D. Caprioli and A. Spitkovsky, *Simulations of Ion Acceleration at Non-relativistic Shocks. II. Magnetic Field Amplification*, *Astrophys. J.* **794** (2014) 46 [1401.7679].

[211] A. Hanusch, T. V. Liseykina, M. Malkov and F. Aharonian, *Steepening of Cosmic-Ray Spectra in Shocks with Varying Magnetic Field Direction*, *Astrophys. J.* **885** (2019) 11 [1907.09226].

[212] E. G. Zweibel, *The microphysics and macrophysics of cosmic rays*, *Phys. Plasmas* **20** (2013) 055501.

[213] P. O. Lagage and C. J. Cesarsky, *The maximum energy of cosmic rays accelerated by supernova shocks*, *Astron. Astrophys.* **125** (1983) 249.

[214] A. R. Bell, *Turbulent amplification of magnetic field and diffusive shock acceleration of cosmic rays*, *Mon. Not. R. Astron. Soc.* **353** (2004) 550.

[215] R. I. Epstein, *The acceleration of interstellar grains and the composition of the cosmic rays*, *Mon. Not. R. Astron. Soc.* **193** (1980) 723.

[216] D. C. Ellison, L. O. C. Drury and J.-P. Meyer, *Galactic Cosmic Rays from Supernova Remnants. II. Shock Acceleration of Gas and Dust*, *Astrophys. J.* **487** (1997) 197.

[217] R. M. Kulsrud, *Plasma Physics for Astrophysics*. Princeton University Press, Princeton, NJ, 2005.

[218] L. Necib, M. Lisanti, S. Garrison-Kimmel, A. Wetzel, R. Sanderson, P. F. Hopkins, C.-A. Faucher-Giguère and D. Kereš, *Under the Firelight: Stellar Tracers of the Local Dark Matter Velocity Distribution in the Milky Way*, *Astrophys. J.* **883** (2019) 27 [1810.12301].

[219] S. Ghosh, S. Sarkar, M. Khan and M. R. Gupta, *Dust ion acoustic shock waves in a collisionless dusty plasma*, *Phys. Lett.* **A274** (2000) 162.

[220] H. Lesch, *Particle heating in supernova shocks*, *Astron. Astrophys.* **239** (1990) 437.

[221] M. A. Malkov and V. I. Sotnikov, *Lower-hybrid drift instability and macroscopic flow of colliding magnetized plasmas*, *Phys. Plasmas* **25** (2018) 102108 [1805.01933].

[222] M. Pohl and R. Schlickeiser, *On the conversion of blast wave energy into radiation in active galactic nuclei and gamma-ray bursts*, *Astron. Astrophys.* **354** (2000) 395.

[223] R. Schlickeiser, R. Vainio, M. Boettcher, I. Lerche, M. Pohl and C. Schuster, *Conversion of relativistic pair energy into radiation in the jets of active galactic nuclei*, *Astron. Astrophys.* **393** (2002) 69 [astro-ph/0207066].

[224] K.-I. Nishikawa, P. Hardee, G. Richardson, R. Preece, H. Sol and G. J. Fishman, *Particle acceleration in relativistic jets due to weibel instability*, *Astrophys. J.* **595** (2003) 555 [astro-ph/0305091].

[225] K.-I. Nishikawa, P. Hardee, G. Richardson, R. Preece, H. Sol and G. J. Fishman, *Particle acceleration and magnetic field generation in electron-positron relativistic shocks*, *Astrophys. J.* **622** (2005) 927 [astro-ph/0409702].

[226] N. A. Krall and P. C. Liewer, *Low-Frequency Instabilities in Magnetic Pulses*, *Phys. Rev.* **A4** (1971) 2094.

[227] P. C. Liewer and N. A. Krall, *Self-consistent approach to anomalous resistivity applied to theta pinch experiments*, *Phys. Fluids* **16** (1973) 1953.

[228] R. C. Davidson and N. T. Gladd, *Anomalous transport properties associated with the lower-hybrid-drift instability*, *Phys. Fluids* **18** (1975) 1327.

[229] N. T. Gladd, *The lower hybrid drift instability and the modified two stream instability in high density theta pinch environments*, *Plasma Phys.* **18** (1976) 27.

[230] N. A. Krall and A. W. Trivelpiece, *Principles of plasma physics*, *Am. J. Phys.* **41** (1973) 1380.

[231] P. J. Cargill and K. Papadopoulos, *A mechanism for strong shock electron heating in supernova remnants*, *Astrophys. J.* **329** (1988) L29.

[232] P. Ghavamian, S. J. Schwartz, J. Mitchell, A. Masters and J. M. Laming, *Electron-Ion Temperature Equilibration in Collisionless Shocks: The Supernova Remnant-Solar Wind Connection*, *Space Sci. Rev.* **178** (2013) 633 [1305.6617].

[233] C. F. Kennel and H. E. Petschek, *Limit on stably trapped particle fluxes*, *J. Geophys. Res.* **71** (1966) 1.

[234] L. K. Jian, H. Y. Wei, C. T. Russell, J. G. Luhmann, B. Klecker, N. Omidi, P. A. Isenberg, M. L. Goldstein, A. Figueroa-Viñas and X. Blanco-Cano, *Electromagnetic waves near the proton cyclotron frequency: Stereo observations*, *Astrophys. J.* **786** (2014) 123.

[235] S. P. Gary, L. K. Jian, T. W. Broiles, M. L. Stevens, J. J. Podesta and J. C. Kasper, *Ion-driven instabilities in the solar wind: Wind observations of 19 March 2005* , *J. Geophys. Res.* **121** (2016) 30.

[236] M. Lazar, P. H. Yoon, R. A. López and P. S. Moya, *Electromagnetic Electron Cyclotron Instability in the Solar Wind* , *J. Geophys. Res.* **123** (2018) 6.

[237] S. P. Gary, *Theory of Space Plasma Microinstabilities*. Cambridge University Press, Cambridge, England, 2005.

[238] M. Rosenbluth, *Stability of the pinch*, Tech. Rep. LA-2030, Los Alamos Scientific Lab.,

N. Mex., 4, 1956.

[239] E. N. Parker, *Dynamical Instability in an Anisotropic Ionized Gas of Low Density*, *Phys. Rev.* **109** (1958) 1874.

[240] E. S. Weibel, *Spontaneously Growing Transverse Waves in a Plasma Due to an Anisotropic Velocity Distribution*, *Phys. Rev. Lett.* **2** (1959) 83.

[241] B. D. Fried, *Mechanism for Instability of Transverse Plasma Waves*, *Phys. Fluids* **2** (1959) 337.

[242] M. V. Medvedev and A. Loeb, *Generation of magnetic fields in the relativistic shock of gamma-ray burst sources*, *Astrophys. J.* **526** (1999) 697 [astro-ph/9904363].

[243] R. D. Blandford and J. P. Ostriker, *Supernova shock acceleration of cosmic rays in the Galaxy*, *Astrophys. J.* **237** (1980) 793.

[244] L. O. C. Drury, *An introduction to the theory of diffusive shock acceleration of energetic particles in tenuous plasmas*, *Rep. Prog. Phys.* **46** (1983) 973.

[245] R. D. Blandford and D. Eichler, *Particle acceleration at astrophysical shocks: A theory of cosmic ray origin*, *Phys. Rep.* **154** (1987) 1.

[246] H. Kucharek and M. Scholer, *Origin of diffuse superthermal ions at quasi-parallel supercritical collisionless shocks*, *J. Geophys. Res.* **96** (1991) 21195.

[247] F. Guo and J. Giacalone, *The Acceleration of Thermal Protons at Parallel Collisionless Shocks: Three-dimensional Hybrid Simulations*, *Astrophys. J.* **773** (2013) 158 [1303.5174].

[248] D. Caprioli, D. T. Yi and A. Spitkovsky, *Chemical Enhancements in Shock-Accelerated Particles: Ab initio Simulations*, *Phys. Rev. Lett.* **119** (2017) 171101 [1704.08252].

[249] P. H. Diamond, S.-I. Itoh and K. Itoh, *Modern Plasma Physics: Volume 1, Physical Kinetics of Turbulent Plasmas*. Cambridge University Press, Cambridge, England, 2010.

[250] T. N. Kato, *Particle acceleration and wave excitation in quasi-parallel high-Mach-number collisionless shocks: Particle-in-cell simulation*, *Astrophys. J.* **802** (2015) 115 [1407.1971].

[251] J. Kauffmann, T. Pillai, Q. Zhang, K. M. Menten, P. F. Goldsmith, X. Lu, A. E. Guzmán and A. Schmiedeke, *The Galactic Center Molecular Cloud Survey*, *Astron. Astrophys.* **603** (2017) A90.

[252] A. A. Galeev and R. N. Sudan, *Basic plasma physics i*, *Plasma Phys.* **1** (1983) 519.

[253] S. Ichimaru, *Basic Principles of Plasma Physics: A Statistical Approach*. CRC Press, 2018.

[254] B. D. Fried and S. D. Conte, *The Plasma Dispersion Function: The Hilbert Transform of the Gaussian*. Academic Press, New York, 1961.